BERGISCHE
UNIVERSITÄT
WUPPERTAL

Powder-Based Additive Manufacturing of Oxide Dispersion-Strengthened Steels

Dissertation to obtain a doctoral degree of

Doctor of Engineering (Dr.-Ing.)

in the

School of Mechanical Engineering and Safety Engineering

University of Wuppertal

Submitted by:

Mareen Goßling

from Coesfeld

Lübeck 2025

Acknowledgement (Danksagung)

Für mich persönlich war es nie das erklärte Ziel, eines Tages eine Dissertation zu schreiben. Umso mehr erfüllt es mich mit Dankbarkeit, heute auf diesen Weg zurückblicken zu dürfen – einen Weg, der sich manchmal geplant anfühlte, oft aber durch glückliche Begegnungen mit Menschen, die mich geprägt und begleitet haben, sowie durch mein eigenes Interesse und meine Anstrengung entstanden ist.

Mein besonderer Dank gilt zunächst Prof. Dr. habil. Bilal Gökce, der mir die Möglichkeit gab, Teil seines neu gegründeten Wuppertaler Lehrstuhls zu werden. Ebenso danke ich Univ.-Prof. Dr.-Ing. Manuel Löwer für die Übernahme des Zweitgutachtens sowie PD Dr.-Ing. habil. Nadine Schlüter und Prof. Dr.-Ing. Axel Schumacher als Mitglieder der Prüfungskommission, die mir ermöglicht haben, diese Arbeit in diesem Rahmen abzulegen.

Ein Dank gilt außerdem allen Kolleginnen und Kollegen am Lehrstuhl, die diese Zeit nicht nur fachlich, sondern vor allem auch menschlich besonders gemacht haben. Ganz besonders hervorheben möchte ich Silja-Katharina Rittinghaus, die mich während meiner gesamten Zeit stets unterstützt hat und als Gruppenleiterin maßgeblich dazu beigetragen hat, eine Arbeitsatmosphäre zu schaffen, in der ich mich nicht nur wissenschaftlich entfalten, sondern auch menschlich wohlfühlen konnte. Ebenso danke ich Markus Wilms, der mir die Tür zur additiven Fertigung bereits lange vor meiner Zeit am Lehrstuhl in Wuppertal geöffnet hat und damit einen wichtigen Grundstein für meinen weiteren wissenschaftlichen und beruflichen Weg gelegt hat. Mein Dank gilt außerdem Inna, Carlos, Claudia, Hamed, Shabbir, Ingo sowie den Studierenden und wissenschaftlichen Hilfskräften, die mich während meiner Zeit begleitet haben: Johanna, Daniel, Nils, Jan Hendrik und Jan Niklas. Ganz besonders danke ich Ivan, für seinen bedingungslosen Support in jeder Lage – und dafür, dass er immer da war, wenn ich ihn am meisten gebraucht habe. Ich möchte auch meinen Bürokollegen Jan Lino danken, der nicht nur ein zuverlässiger Sparringspartner für viele Fragen war sondern auch einen großen Anteil daran hat, dass selbst an schwierigen Tagen immer auch Raum für gute Gespräche und leckeren Kaffee blieb.

Wer mich kennt, weiß, dass neben den wissenschaftlichen Erkenntnissen vor allem das Zwischenmenschliche für mich eine große Rolle spielt. Daher war es für mich besonders wertvoll, im Rahmen eines DFG-geförderten Projekts im Schwerpunktprogramm 2122 „Materials for Additive Manufacturing" arbeiten zu dürfen und dabei viele junge Wissenschaftlerinnen und Wissenschaftler in ganz Deutschland kennenzulernen. Ohne die Unterstützung aus diesem Team hätte meine Forschung nicht diese Tiefe erreicht. Deshalb danke ich allen Beteiligten des SPP, insbesondere jenen, die aktiv zu meiner Arbeit und auch zu meinem psychischen Wohlbefinden beigetragen haben: Marie-Louise, Somnath, Nick, Felix und Louis.

Darüber hinaus ergaben sich weitere wertvolle Forschungskontakte, bei denen ich mich herzlich bedanken möchte: Abdelrahman Elsayed und Marina Macias Barrientos – danke für eure Zeit, eure Beratung und alles, was ich von euch lernen durfte.

Da mir die Arbeit nicht immer leichtgefallen ist, bin ich umso dankbarer für jeden Rückhalt und jede Aufmunterung, sei es in den Pausen, beim Mensaessen, auf abendlichen Fahrradtouren, in Telefonaten oder einfach zuhause in meiner WG. Mein besonderer Dank gilt daher meinen Freunden: Nils, Freddie, Lisa, Max, Jonte, Franz, Nicole, Catharina, Helen und Kristin sowie meinen wunderbaren

Mitbewohnerinnen und Mitbewohnern PC, Paul, Larissa, Pia, Michele, Martin, Prabhat, Sven, Janina, Leyla und Masoud.

Zu guter Letzt möchte ich meiner Familie danken, die mich immer bedingungslos unterstützt hat. Danke an meine Eltern Brigitte und Wilfried, die mir Geborgenheit gegeben und mich zugleich zur Unabhängigkeit erzogen haben – mit dem Mut, mich Dinge zu trauen und keine Angst vor dem Scheitern zu entwickeln. Danke auch an meine Geschwister Kevin und Jenna, die mir schon früh beigebracht haben, den nötigen Biss zu entwickeln – nicht nur, um das größte Stück Schokolade im Vanillepudding zu bekommen oder die Macht über die Fernbedienung, sondern auch, um meine eigenen Ziele zu erreichen.

Abstract

This dissertation explores the integration of oxide nanoparticles (NPs) into powder bed fusion using a laser beam (PBF-LB/M) to fabricate oxide dispersion-strengthened (ODS) steels with enhanced high-temperature performance. A simplified Fe20Cr alloy system was used to systematically investigate how NP characteristics—such as size, morphology, crystallographic phase, and distribution—affect microstructure evolution and mechanical behaviour.

Three peer-reviewed studies form the empirical foundation: Study I establishes the feasibility of a fully laser-assisted process chain using laser-generated ZrO_2 NPs; Study II compares nanoparticle additivation methods (ball milling vs. dielectrophoretic deposition) using Y_2O_3; and Study III examines the influence of ZrO_2 synthesis route and loading on microstructure and mechanical response. Key findings include that laser-generated NPs promote grain refinement and creep resistance, but suffer from agglomeration at higher loadings, while chemically synthesized NPs provide superior grain stability after heat treatment. The highest creep resistance ($5.0 \times 10^{-8}\,s^{-1}$ at 600 °C, 50 MPa) was achieved using 1.0 vol% laser-generated ZrO_2 NPs.

The results highlight that ODS performance in AM systems depends less on theoretical particle spacing and more on retained NP size and thermal stability. Additivation strategy, synthesis route, and NP concentration must be jointly optimized to tailor short-term and long-term mechanical properties. This work provides foundational insights and process guidelines for advancing ODS steel design in laser-based additive manufacturing.

Abstract (German)

In diese Dissertation wird die Integration von Oxid-Nanopartikeln (NPs) in das pulverbettbasierte Laserstrahlschmelzen (PBF-LB/M) zur Herstellung von oxiddispersionsgehärteten (ODS) Stählen mit verbesserter Hochtemperaturbeständigkeit untersucht. Als Modellsystem dient ein vereinfachter Fe20Cr-Werkstoff, um systematisch zu analysieren, wie NP-Eigenschaften – insbesondere Größe, Morphologie, Kristallstruktur und Verteilung – die Mikrostrukturentwicklung und das mechanische Verhalten beeinflussen.

Die Arbeit basiert auf drei peer-reviewten Studien: Studie I untersucht die Machbarkeit einer vollständig laserbasierten Prozesskette mit lasererzeugten ZrO_2-NPs. Studie II vergleicht Additivierungsmethoden (Pulverkugekmahlen vs. dielektrophoretische Deposition) unter Verwendung von Y_2O_3. Studie III analysiert den Einfluss der ZrO_2-Syntheseroute und Partikelkonzentration auf Mikrostruktur und mechanische Eigenschaften. Zentrale Ergebnisse zeigen, dass lasererzeugte NPs Kornfeinung und Kriechbeständigkeit fördern, jedoch bei höheren Konzentrationen zur Agglomeration neigen. Chemisch synthetisierte NPs bieten hingegen eine höhere Kornstabilität nach der Wärmebehandlung. Die beste Kriechbeständigkeit ($5{,}0 \times 10^{-8}\,s^{-1}$ bei 600 °C und 50 MPa) wurde mit 1,0 Vol.-% lasererzeugten ZrO_2-NPs erreicht.

Die Resultate verdeutlichen, dass die Leistungsfähigkeit von ODS-Stählen in der additiven Fertigung weniger von theoretischen Partikelabständen als vielmehr von der Stabilität und Größe der eingebetteten NPs abhängt. Additivierungsstrategie, Syntheseroute und Partikelkonzentration müssen gezielt aufeinander abgestimmt werden, um sowohl kurzfristige als auch langzeitmechanische Eigenschaften zu optimieren. Diese Arbeit liefert grundlegende Erkenntnisse und praxisrelevante Leitlinien zur Weiterentwicklung laserbasierter ODS-Stahlkonzepte in der additiven Fertigung.

List of Abbreviations

Abbreviation	Long term
AM	Additive Manufacturing
APT	Atom Probe Tomography
as-built	AB
BM	Ball Milling
DD	Dielectrophoretic Deposition
DED	Direct Entergy Deposition
ECCI	Electron Channeling Contrast Imaging
HIP	Hot isostatic pressing
HT	Heat treatment
IPD	Interparticle distance
IPDs	Interparticle distances
LAL	Laser Ablation in Liquids
LOM	Light optical microscopy
NP	Nanoparticle
NPs	Nanoparticles
ODS	Oxide Dispersion-Strengthened
PBF-LB/M	Laser Powder Bed Fusion
SEM	Scanning Electron Microscope
TEM	Transmission Electron Microscope
Y_2O_3	Yttria
ZrO_2	zirconia

Table of Content

1. General Introduction

1.1 Motivation and Relevance

The global transition to carbon-free energy production is both urgent and complex. [1] According to the IPCC Sixth Assessment Report, global CO_2 emissions must be reduced by at least 42% by 2030 [2] to limit global warming to 1.5 °C [3]. Simultaneously, global energy demand is expected to increase by 24% by 2040, primarily driven by energy-intensive sectors such as steel, cement, and petrochemicals [4]. Meeting these opposing demands requires more efficient energy generation systems and the deployment of advanced technologies such as fusion power plants. These developments call for structural materials capable of withstanding extreme thermal, mechanical, and radiation loads in next-generation energy environments. [1, 5–8]

Oxide dispersion-strengthened (ODS) steels are among the most promising candidates. These materials offer exceptional creep resistance, thermal stability, and microstructural integrity, making them attractive for applications in advanced combustion engines, hydrogen turbines, and nuclear fusion environments. [9, 10] A prominent example is EUROFER97, a ferritic ODS steel developed within European fusion research (e.g., DEMO and IFMIF) for high-temperature components due to its low activation characteristics and robust long-term performance.

The superior properties of ODS steels arise from a fine and stable dispersion of nanoscale oxide particles within the matrix, which effectively hinder dislocation motion and grain boundary migration. [11–13] Conventional processing routes, such as mechanical alloying [14] followed by hot isostatic pressing (HIP), have proven effective but remain costly, complex, and difficult to scale.

Additive manufacturing (AM)—particularly laser powder bed fusion (PBF-LB/M)—has emerged as a promising alternative. [15] PBF-LB/M offers near-net-shape manufacturing, material savings, and opportunities for microstructural control. [12, 16–20] However, achieving homogeneous NP dispersion and stable integration during AM remains a key challenge. Performance in ODS steels depends critically on NP characteristics, especially particle size (typically 2–10 nm), morphology, and composition. These features govern dispersion behaviour, melt pool interactions, and long-term stability in the solidified part. [21–24]

Chemical and physical synthesis methods have been shown to produce tailored oxide nanoparticles (NPs) suitable for strengthening mechanisms. [25–27] Nevertheless, when introduced into the PBF-LB/M process, issues such as agglomeration, loss, and non-uniform distribution often arise.

This dissertation addresses these challenges by systematically comparing two types of ZrO_2 nanoparticles: one produced via laser ablation in liquids (LAL), and the other through conventional chemical synthesis. This approach enables a detailed investigation of how synthesis route, dispersion behaviour, and concentration affect microstructure and high-temperature mechanical properties in a simplified alloy system.

Fe20Cr is employed as a model alloy to reduce compositional complexity and isolate NP-related effects. This binary system captures the key characteristics of ferritic ODS steels while avoiding confounding factors associated with more complex compositions, such as those in EUROFER97 [28], PM2000 [29] or MA956 [30].

This dissertation investigates how:

- different NP types (ZrO_2 and Y_2O_3),
- their synthesis methods (chemical vs. laser-based),
- and their additivation strategies (mechanical vs. dielectrophoretic)

influence NP dispersion, microstructure evolution, and selected high-temperature mechanical properties before and after PBF-LB/M and subsequent heat treatment (HT). Emphasis is placed on creep resistance in selected ZrO_2-containing systems.

1.2 Research Questions

This dissertation addresses key challenges related to oxide nanoparticle integration in laser-based AM of ODS steels. Using Fe20Cr as a model alloy, and investigating two oxide types (Y_2O_3 and ZrO_2) introduced via distinct synthesis and additivation methods, the following research questions are formulated:

1) How and why do NP characteristics (size, morphology, chemistry) evolve from powder to solid part during the LPBF-LB/M process?
2) How do theoretical predictions (e.g., by Rösler and Arzt) for NP size and interparticle distance in the solid part correlate with experimental results?
3) How do different NP sizes and interparticle distances affect grain growth and NP characteristics (e.g., size and spacing) in rapidly solidified microstructures and after heat treatment?
4) How are NP size and distribution correlated with fundamental mechanical properties such as strength and creep resistance?

By answering these questions, the dissertation aims to deepen the understanding of the interrelation between nanoparticle (NP) design, feedstock preparation, and microstructural evolution in PBF-LB/M-processed ODS steels.

1.3 Structure of the Dissertation

This dissertation consists of three peer-reviewed studies that explore various stages of NP integration into Fe20Cr-based ODS alloys (see Appendix A, B, C):

I. Goßling, M., Rittinghaus, S.-K., Bharech, S., Yang, Y., Wilms, M.B., Becker, L., Weber, S., Xu, B.-X., Gökce, B. (2023)
Towards enhancing ODS composites in laser powder bed fusion: Investigating the incorporation of laser-generated zirconia nanoparticles in a model iron–chromium alloy. *Journal of Materials Research*, 39 (5), 774–788.
DOI: 10.1557/s43578-023-01267-4

II. Goßling, M., Rittinghaus, S.-K., Radtke, F., Elsayed, A., Kuşoğlu, I.M., Hariharan, A., Krupp, U., Gökce, B. (2024)
Oxide Distribution in PBF-LB/M-Processed ODS Steel: Effects of Ball Milling and Dielectrophoretic Deposition in Powder Production. *Powder Metallurgy,* 68 (1), 29-40
DOI: 10.1177/00325899241304735

III. Goßling, M., Rittinghaus, S.-K., Radtke, F., Elsayed, A., Barrientos, M. M., Ziesing, U., Becker, L., Kuşoğlu, I.M., Broeckmann, C., Krupp, U., Hariharan, A., Weber, S., Gökce, B. (2025) Mechanical and Microstructural Effects of ZrO_2 Nanoparticles in Fe20Cr Oxide Dispersion-Strengthened Alloys Processed by Laser Powder Bed Fusion
Advanced Engineering Materials, 2500317
DOI: 10.1002/adem.202500317

All three studies are co-authored. Mareen Goßling's specific contributions are outlined in Appendices A–C, while the roles of co-authors are documented within each publication. Journals were selected based on thematic relevance: Journal of Materials Research and Advanced Engineering Materials focus on materials science and microstructure–property relationships, while Powder Metallurgy addresses feedstock-related aspects relevant to NP dispersion.

The dissertation is structured as follows:

- Chapter 1 introduces the motivation, relevance, and research questions.
- Chapter 2 provides the scientific background on ODS steels, strengthening mechanisms, and challenges in AM.
- Chapter 3 summarizes the methodology and main findings of the three core studies.
- Chapter 4 integrates the findings, addressing the research questions through thematic analysis, limitations, and implications for practice.
- Chapter 5 concludes the work, highlighting its main contributions and identifying future research directions.

2. Scientific Background

The following subchapters provide an overview of ODS materials in AM, including the fundamental strengthening mechanisms, the role of NPs, their generation methods, and their significance in enhancing ODS properties.

2.1 Oxide Dispersion Strengthened Steels

ODS alloys have been developed since the 1970s, originally for nuclear applications due to their exceptional thermal and radiation stability. Early ferritic systems, such as DT and DY (13 wt% Cr, CEN/SCK, Belgium) and MA957 (14 wt% Cr, INCO, USA), were tailored for extreme environments. In the 1990s, Japanese research (PNC) refined these materials by optimizing Y_2O_3 dispersion and improving mechanical performance. Around 2000, renewed interest arose following the discovery of nanoclusters in 12YWT alloys, revealing high densities of Ti-, Y-, and O-enriched oxides. [31]

ODS steels are metallic composites containing thermally stable oxide particles that impede dislocation motion and grain boundary migration. This leads to enhanced strength at elevated temperatures, improved creep resistance, and higher radiation tolerance. Their performance depends critically on oxide particle size, distribution, and the nature of the oxide–matrix interface. Powder metallurgy routes—most commonly mechanical alloying followed by consolidation via HIP, hot extrusion, or SPS—are used to achieve these dispersions. Subsequent thermomechanical treatments such as hot rolling can further refine the microstructure and improve creep properties. [32]

The formation and stability of oxides are governed by alloy composition and processing temperature. In Fe–14Cr alloys consolidated by HIP, oxide formation begins around 450 °C and continues up to 1100 °C, with minimal coarsening during annealing.[33] In contrast, Fe–Cr–Al systems show more complex precipitation behaviour, influenced by alloying elements like Al, Zr, or Hf. Depending on the local chemistry, stable oxides such as $YAlO_3$, $Y_3Al_5O_{12}$, Al_2O_3, and Y–Hf–O phases may form. [34, 35] High Cr content and the presence of Al favour phase complexity and promote coarsening. For example, Al-containing ferritic ODS steels often form larger oxide particles (e.g., Y_2O_3, TiO_2), which reduce dispersion effectiveness due to Ostwald ripening. [36] The oxide–matrix orientation relationship is also temperature-sensitive. In PM2000, for instance, cuboid-on-cube alignment of $YAlO_3$-type NPs is observed in the as-extruded state, but this orientation deteriorates after annealing at 1200 °C and partially reorients at 1300 °C. [37]

Overall, these observations highlight the strong interplay between alloy composition, processing conditions, and oxide particle evolution. To isolate and better understand these interactions, this work uses a simplified binary Fe–Cr alloy system (Fe20Cr). This model retains the key features of ferritic ODS steels while reducing compositional complexity, allowing systematic analysis of NP characteristics, dispersion behaviour, and their impact on microstructure and mechanical performance under AM conditions.

2.2 Strengthening Mechanisms in ODS Alloys

The mechanical properties of metals can be improved by various strengthening mechanisms, including solid solution strengthening, work hardening, grain boundary strengthening, precipitation hardening, and Orowan strengthening. In ODS alloys, several mechanisms may contribute, but at elevated temperatures, Orowan-type dislocation bypassing is dominant due to the high number density of stable oxide NPs. [38]

Orowan strengthening describes the bowing of dislocations between non-shearable particles, forming loops that increase the stress required for continued plastic deformation. The corresponding shear stress (τ_{Or}) is given by [39]:

$$\tau_{Or} = \frac{Gb}{L - 2R}$$

where (G) is the shear modulus, (b) the Burgers vector, (L) the interparticle distance (IPD), and ($2R$) the particle diameter. According to theoretical models by Arzt and Rösler, maximum strengthening occurs with particle sizes below ~10 nm, provided the particle spacing is optimized. However, very small particles (<10 nm) may enable thermally activated dislocation detachment, which limits their effectiveness. [39]

If the oxide particles are coherent or semi-coherent, they can be cut by dislocations. In this case, the required shear stress scales with √R. A transition between shearing and bypassing occurs at a critical particle size $\tau \propto R^{1/2}$, which marks the point of maximum yield strength (see Figure 1). [39]

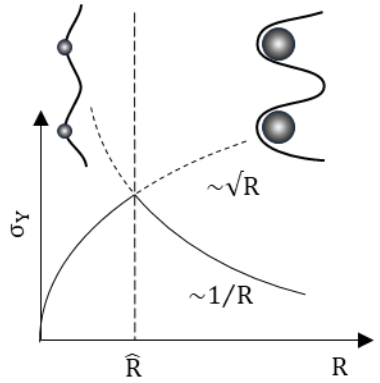

Figure 1 The interplay between dislocation cutting and bypassing results in a peak in yield strength (σ_Y) as a function of particle radius (R). Cutting stress increases with √R, while bypassing stress decreases with $1/R$. The maximum σ_Y occurs at the crossover point with an optimal particle size $\hat{R}$. (redrawn after Gottstein, 2011 [40])

In practical ODS steels, oxides typically range from 1 to 100 nm [32, 36, 41–43], with optimal strengthening achieved by dispersoids between 2 and 10 nm. Particle number densities between 10^{22} and 10^{23} particles per cubic meter [33, 44–46], yielding interparticle distances (IPDs) of 10–1000 nm [44] enhance strength by several hundred MPa [32]. For example, 2–5 nm $Y_2Ti_2O_7$ particles in Fe–14Cr or ~5 nm dispersoids in Fe–12Cr–2W–0.5Y_2O_3 have demonstrated superior high-temperature strength and grain refinement (~280 nm vs. ~350 nm), enhancing creep resistance through Zener pinning. [44, 46]

Besides size and distribution, the chemistry and crystal structure of oxide NPs also affect their performance. Coherent or semi-coherent particles like $Y_4Al_2O_9$ (YAM) below 10 nm can improve strength at intermediate temperatures[47], whereas larger, incoherent particles (>20 nm) offer stronger dislocation resistance but may compromise ductility [47, 48]. Poor bonding or wetting at the interface can lead to clustering and reduced performance [48].

Alloy composition and thermomechanical processing influence both grain structure and oxide behaviour. Alloying with Ti or Al refines grains and improves high-temperature stability [49–51]. Recrystallization and grain growth from 0.4 to 1.1 µm during HT enhance creep resistance [52] and deformation-induced recrystallization has also been observed [53].

However, mechanical alloying—a common method for feedstock preparation—can induce NP agglomeration and deformation, reducing dispersion quality [44, 54]. Prolonged milling affects powder morphology and flowability, complicating subsequent processing steps [55].

At elevated temperatures, creep behaviour is governed not only by classical Orowan mechanisms but also by thermally activated dislocation detachment. According to Rösler and Arzt, the creep rate $\dot{\varepsilon}$ follows an Arrhenius-type equation [56]:

$$\dot{\varepsilon} = \varepsilon_0 \exp\left(-\frac{E_d}{k_B T}\right)$$

where E_d is the activation energy for detachment, k_B the Boltzmann constant, and T the absolute temperature. This model highlights the role of interface properties—such as coherency and bonding strength—in high-temperature deformation.

Experimental data confirm that creep resistance in FeCr-based ODS steels correlates with NP size, particle density, and grain structure. Typical test conditions range from 600–1000 °C and 150–425 MPa. [57] While direct creep rates are rarely reported, derived parameters—activation energies (~581 kJ/mol [58]), stress exponents (n ≈ 5–18 18 [58–60]), and a threshold stress of ~145 MPa [59]—offer insights into the governing mechanisms. Increasing Y_2O_3 content (e.g., from 0.38 to 1 wt%) in Fe–18Cr alloys improves creep strength by increasing the number of effective pinning sites[58].

In summary, the high-temperature performance of ODS steels is enabled by a synergistic interplay of Orowan strengthening, grain boundary pinning, and structural stability. These mechanisms are sensitive to NP size, spacing, chemistry, and matrix interaction—parameters that are in turn dictated by synthesis and additivation strategies. This work specifically investigates how different NP types (ZrO_2 vs. Y_2O_3), synthesis methods (chemical vs. laser-based), and integration routes (mechanical vs. dielectrophoretic) affect NP behaviour and mechanical performance in Fe20Cr-based ODS alloys.

2.3 Additive Manufacturing of ODS Alloys: Opportunities and Challenges

AM, particularly PBF-LB/M, offers promising advantages for ODS alloys, including near-net-shape fabrication, refined microstructure control, and improved material efficiency. However, transferring ODS concepts into AM processes presents significant challenges—chiefly due to the interaction of oxide NPs with the rapidly changing thermal and fluid dynamic environment of the melt pool.

Well before laser exposure, the quality of the powder bed plays a critical role. Flowability and packing density depend on particle morphology, surface texture, and interparticle forces. Mechanically alloyed powders, commonly used in ODS systems, often suffer from irregular shapes and rough surfaces. These characteristics reduce powder bed homogeneity and can lead to density variations in the final part, compromising component integrity. [61–64]

Mechanical alloying methods such as ball milling (BM) are widely applied for NP incorporation [65–67]. Through repeated cold welding and fracturing, a fine oxide dispersion can be achieved. Yet, prolonged milling increases the risk of NP agglomeration and alters powder morphology—leading to reduced flowability and packing density. [68–70]. Thermomechanical effects, such as matrix amorphization or phase changes, may also arise under excessive milling conditions [71, 72]. As milling parameters strongly influence these outcomes, precise control is essential to avoid contamination or work hardening [73, 74].

These powder-related factors carry over into the melting process. Oxide NPs may partially or fully dissolve in the melt pool, especially under high thermal loads or in reactive environments. Their final size and distribution are governed by diffusion kinetics and solidification behaviour [75, 76] While some studies observed complete dissolution of Y_2O_3 and subsequent re-precipitation into Y–Si–O phases [77], others reported thermal stability under milder exposure conditions [78]. When elements like Y and O dissolve and redistribute, complex oxides such as Y–Al–O may form [79], which can reduce strengthening efficiency if not homogeneously integrated. Undissolved or agglomerated particles may migrate to the melt pool surface due to buoyancy effects, forming slag and reducing NP incorporation efficiency [80–82].

Solidification dynamics further influence NP incorporation. At low cooling rates, particles may be rejected at the solid–liquid interface, leading to segregation and heterogeneous microstructures [83–85]. Compared to PBF-LB/M, techniques such as directed energy deposition (DED) typically yield coarser structures and lower NP densities due to larger melt pools and slower cooling rates. [86–88]

Within PBF-LB/M itself, process parameters like laser power and scan speed directly affect dispersoid formation. For example, higher power and slower scanning increase thermal exposure and promote oxide coarsening. Conversely, faster scanning reduces thermal impact, favoring finer and more numerous particles. Hou et al. [89] demonstrated that increasing scan speed from 1.2 to 1.6 m/s reduced the mean Y_2O_3 particle size from 21 to 16 nm and simultaneously increased number density. In comparison, conventional ODS materials such as MA754 exhibit far higher dispersoid densities and volume fractions, highlighting the need for further process optimization in AM. [89]

Alloy composition also plays a role. For instance, increasing aluminum content (0.4 to 2.5 wt%) in 9Cr ODS steels results in coarser Y–Al–O dispersoids (14.2 to 20.9 nm) due to thermodynamic stabilization of $YAlO_3$ and $Y_3Al_5O_{12}$, accompanied by a reduced particle number density. [90] Similar trends have been reported for Ni-based alloys, where Al (1 wt%) promotes the formation of larger inclusions from 21 nm to 27 nm and reduces dispersoid volume fractions from 0.24% to 0.15%. [89]

Direct observation of these effects during processing remains difficult. In-situ X-ray imaging can reveal melt pool phenomena such as porosity or keyhole formation, [91] but lacks the resolution to track nanoscale particles. Tracer particle experiments using larger ceramics (~5 µm) help visualize melt pool flow and redistribution patterns, [92] offering indirect insights into NP behaviour. Nonetheless, the underlying mechanisms of NP evolution in PBF-LB/M remain incompletely understood, complicating process optimization.

Overall, achieving fine and stable oxide dispersions in AM-produced ODS steels requires a detailed understanding of how powder properties, process parameters, alloy composition, and thermal profiles interact. This dissertation addresses these complexities by comparing laser-generated and chemically synthesized NPs, combined with different additivation strategies, to evaluate their impact on NP retention, distribution, and the resulting microstructure in Fe20Cr-based alloys processed via PBF-LB/M.

2.4 ODS Feedstock Preparation

The preparation of NP-functionalized feedstocks is a critical step in fabricating ODS alloys via AM. Not only must the NPs be well-dispersed and thermally stable, but their integration must also preserve powder flowability and ensure compatibility with the PBF-LB/M process. This section outlines the strategies used to modify metal powders with oxide NPs and describes how the synthesis

route affects their size, morphology, and phase composition. These parameters form the basis for the tailored powder systems used in this work.

2.4.1 Nanoparticle Additivation Strategies in Metal Powder Processing

Two complementary techniques were selected for the integration of oxide NPs into Fe20Cr-based powders: mechanical BM and dielectrophoretic deposition (DD). Both aim to achieve homogeneously distributed NPs but differ fundamentally in process conditions and their influence on powder characteristics.

BM relies on repeated cold welding, fracturing, and rewelding under high-energy collisions. This promotes strong connection between metal and oxides and enables atomic-scale mixing. Under optimized conditions, supersaturation of alloying elements and the formation of sub-nanometer clusters can occur, as demonstrated for Y–Ti–O–Cr systems. [93–95] However, prolonged milling promotes agglomeration, surface roughening, and the development of irregular particle shapes—leading to poor flowability and limited PBF-LB/M compatibility. [61–64] Excessive impact energy can also trigger amorphization or unwanted phase transformations in ferritic matrices. [71, 72] To avoid these effects, careful optimization of milling parameters is essential, including energy input, atmosphere, and time. [68, 69, 73, 74, 95]

In contrast, DD enables NP coating via the application of non-uniform electric fields to a suspension containing both metal powders and oxide NPs. The dielectrophoretic force selectively moves particles based on their polarizability relative to the medium, allowing NPs to attach to powder surfaces without mechanical deformation. This preserves powder morphology and flowability, if suspension stability and field strength are well-controlled. Key variables such as solvent properties, NP size, conductivity, and field frequency influence coating homogeneity and prevent clustering or incomplete deposition. [95, 96]

Each strategy exhibits trade-offs: BM ensures strong oxide–matrix interaction but often degrades particle morphology, while DD enables gentle deposition but is more sensitive to processing conditions. This dissertation exploits these contrasts by deliberately applying both methods to produce feedstocks with distinct NP distributions and morphologies. Their influence on NP integration, microstructure evolution, and mechanical behaviour is systematically investigated in the subsequent chapters.

2.4.2 Nanoparticle Synthesis: Conventional and Laser-Based Approaches

The effectiveness of oxide NPs in ODS alloys strongly depends on their physical and chemical characteristics. In this work, two types of ZrO_2 NPs are used: commercially synthesized and laser-generated NPs produced via LAL.

Conventional chemical synthesis techniques such as sol-gel, co-precipitation, and hydrothermal methods offer control over size and morphology by adjusting parameters like precursor concentration, pH, and reaction time. [97–100] However, these methods often yield broad size distributions and irregular morphologies and may require surfactants or stabilizers that hinder NP–matrix bonding. Agglomeration during drying, limited reproducibility, and chemical residues pose further challenges. [101–104]

LAL represents a clean, top-down alternative, where high-energy laser pulses ablate a solid target submerged in liquid, forming a plasma and cavitation bubble in which NPs nucleate and cool rapidly.

[27, 105] This approach avoids chemical precursors and produces ligand-free particles, making it ideal for integration into metal powders. Laser parameters—such as fluence, pulse duration, and repetition rate—as well as the choice of liquid medium significantly affect particle size, crystallinity, and surface properties. [106, 107] Ultrafast lasers tend to yield finer and more uniform particles (<30 nm), while nanosecond lasers produce broader distributions (20–150 nm). [27, 105, 107] Solvent composition and additives like SDS can further modify nucleation dynamics and crystal phase formation. [106]

In this work, the laser-generated ZrO_2 NPs exhibit narrow size distributions below 10 nm, spherical morphology, and a tetragonal crystal structure. These properties are favorable for homogeneous dispersion and effective Orowan strengthening. By contrast, the chemically synthesized ZrO_2 NPs display a wider size range, monoclinic structure, and irregular shapes, potentially leading to larger inclusions and less uniform retention during PBF-LB/M. The contrasting nature of these particles provides a basis for directly comparing how synthesis routes influence final microstructure and mechanical performance.

3. Summary of Publications

In this chapter the three peer-reviewed studies are summarized and form the empirical base of this dissertation. The central objective is to understand how NP characteristics—particularly size, morphology, and crystal structure—as well as their additivation strategy affect NP dispersion, microstructural development, and high-temperature mechanical properties in Fe20Cr-based ODS steels produced via PBF-LB/M.

The studies follow a targeted, hypothesis-driven approach to address four key research questions:

1) How and why do NP characteristics evolve from powder to solid part during the LPBF-LB/M process?
2) How do theoretical predictions for NP size and interparticle distance in the solid part correlate with experimental results?
3) How do different NP sizes and interparticle distances affect grain growth and NP characteristics in rapidly solidified microstructures and after heat treatment?
4) How are NP size and distribution correlated with fundamental mechanical properties such as strength and creep resistance?

Building on the background in Chapters 1 and 2, this chapter positions each study within the process–structure–property framework, which is fundamental to materials science. It highlights how material selection (e.g., Fe20Cr, ZrO_2, Y_2O_3), powder preparation and processing strategies (e.g., PBF-LB/M, LAL, DD, BM), and resulting microstructures (e.g., grain size, NP dispersion) interact to determine the mechanical behaviour of the final part. This conceptual framework is illustrated in Figure 2.

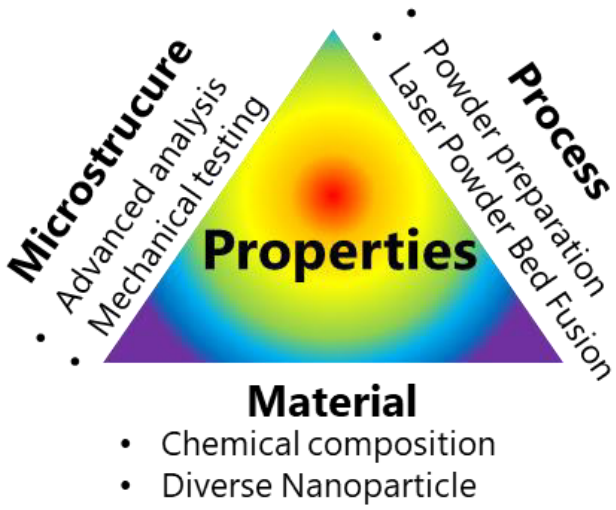

Figure 2 Interrelation of material, process, and microstructure in determining material properties.

Each study targets a specific aspect of this framework:

— Study I assesses the feasibility of using laser-generated ZrO_2 NPs.
— Study II compares additivation methods (BM vs. DD) using Y_2O_3.
— Study III investigates how ZrO_2 synthesis route and content affect microstructure and mechanical performance.

3.1 Overall Methodology

The experimental approach of this dissertation follows a structured three-step workflow (Figure 3):

(a) synthesis of oxide NPs with distinct sizes, morphologies, and crystallographic phases; (b) integration of these NPs into Fe20Cr powder via either BM or DD; and (c) processing of ODS specimens by PBF-LB/M, followed by microstructural and mechanical characterization.

A binary Fe20Cr alloy was used throughout all studies as a simplified model alloy to isolate NP-related effects. Its binary composition avoids complex oxide formation and secondary strengthening mechanisms typical in multicomponent systems (e.g., PM2000, EUROFER97), enabling clearer interpretation of NP behaviour under AM conditions. Two oxide types were investigated; Y_2O_3 (used in Study II to compare additivation methods), and ZrO_2 (studied in Study I and III using both laser-generated and chemically synthesized variants at 0.1 and 1.0 vol%)

NP synthesis was conducted via LAL or chemical sol-gel method, resulting in particles with varied sizes, shapes, and phase compositions. NP integration was achieved by BM or DD, yielding feedstocks with distinct surface coverage, dispersion quality, and retention behaviour. AM was performed using PBF-LB/M with standardized parameters across all studies, followed by selected HT.

Characterization included Scanning Electron Microscope (SEM), Transmission Electron Microscope (TEM), Electron Channeling Contrast Imaging (ECCI), EBSD, and XRD to assess NP dispersion, grain size, and phase composition. Mechanical properties were evaluated via hardness testing, high-temperature compression (600 °C), and steady-state creep measurements.

Based on Study II, which showed that DD offers better dispersion and flowability than BM, the follow-up Study III adopted DD to systematically investigate the effects of NP synthesis route and loading under otherwise identical processing conditions.

Across all investigations, the aim was to establish clear structure–property relationships by linking NP characteristics—size, distribution, morphology, phase stability—with microstructural evolution (e.g., interparticle spacing, grain refinement) and key strengthening mechanisms, especially Orowan strengthening and grain boundary pinning. This methodology directly supports the research questions outlined in Chapter 1 and provides the foundation for the interpretation of AM-processed ODS steels presented in Chapter 4.

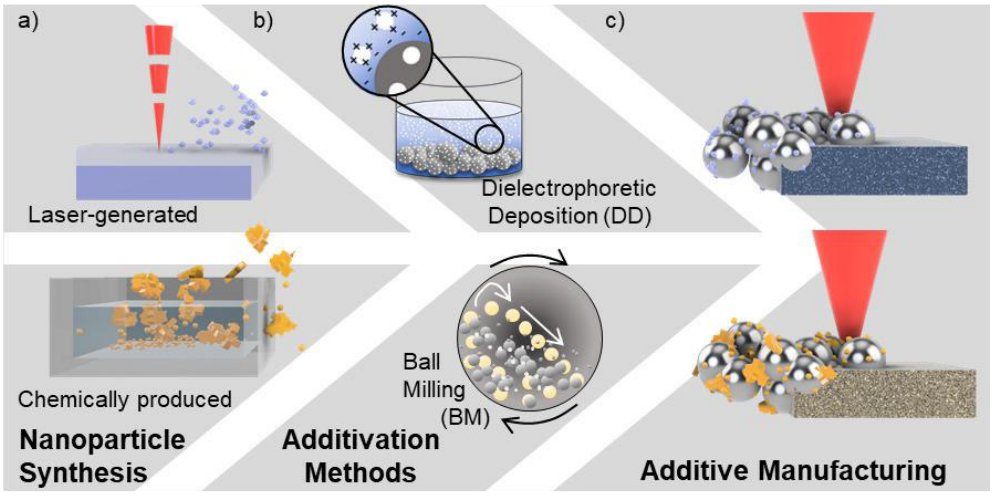

Figure 3 Overview of processes analysed within this dissertation.

3.2 Study I

Goßling, M., Rittinghaus, S.-K., Bharech, S., Yang, Y., Wilms, M.B., Becker, L., Weber, S., Xu, B.-X., Gökce, B. (2024)

Towards enhancing ODS composites in laser powder bed fusion: Investigating the incorporation of laser-generated zirconia nanoparticles in a model iron–chromium alloy.

Journal of Materials Research, 39 (5), 774–788

DOI: 10.1557/s43578-023-01267-4

CRediT Authorship Contribution of Mareen Goßling: Investigation, visualization (lead), writing-original draft preparation (lead).

3.2.1 Objective

This study aimed to evaluate the feasibility of a fully laser-assisted process chain for producing ODS composites using PBF-LB/M. The approach combines LAL for synthesizing ZrO_2 NPs, DD for powder additivation, and AM via PBF-LB/M. The central goal was to trace NP behaviour during each processing stage and explore whether laser-generated ZrO_2 NPs could be effectively integrated into a Fe20Cr matrix to enhance material properties.

3.2.2 Key Findings

The study successfully established a fully laser-assisted process chain combining LAL for NP synthesis, DD for powder additivation, and PBF-LB/M for consolidation. Laser-generated ZrO_2 NPs with a narrow size distribution (d_{50} ≈ 3.8 nm; d_{90} ≈ 10 nm) were homogeneously deposited onto Fe20Cr powders without altering particle morphology or flowability. The consolidated parts were dense and crack-free, exhibiting a relative density of 98.3%, slightly below the 99.7% of the non-additivated reference. Despite the relatively high NP loading (0.8 wt% ≈ 1.0 vol%), no significant grain refinement was observed in the as-built (AB) state, and the room-temperature hardness remained nearly unchanged at 217.4 ± 11 $HV_{0.1}$ compared to 219.2 ± 9 $HV_{0.1}$ for the reference material. These findings were attributed to the limited wetting behaviour of ZrO_2 in the Fe–Cr melt, which hindered heterogeneous nucleation during solidification and leading to lower densities.

3.2.3 Conclusion

Study I contributes to the first and second research questions of this dissertation. It provides direct numerical and experimental evidence for the evolution of NP size and distribution during processing, as well as initial comparisons with theoretical dispersion expectations. At the high NP concentration of 1 vol%, no noticeable changes in grain size were observed, which was in line with expectations. In contrast, Study III reported clear grain refinement under similar conditions, due to the use of SEM-EBSD analysis, whereas the present study relied on Light optical microscopy (LOM) with limited spatial resolution. (cf. Chapter 3.3).

The study thus confirms the technical feasibility of using laser-generated ZrO_2 NPs for ODS production via AM and highlights DD as a promising additivation technique. However, it also reveals that microstructural and mechanical enhancements remain moderate unless agglomeration, wetting, and dispersion behaviour are precisely controlled and analysed with appropriate microstructural techniques.

In the broader context of this thesis, Study I serves as a methodological and conceptual foundation: it validates the process chain and identifies key variables—NP size, wetting, agglomeration—which must be optimized to realize effective particle strengthening in ODS steels. Future studies build upon these findings to refine the relationships between NP characteristics, dispersion, and high-temperature mechanical performance.

3.3 Study II

Goßling, M., Rittinghaus, S.-K., Radtke, F., Elsayed, A., Kuşoğlu, I.M., Hariharan, A., Krupp, U., Gökce, B. (2024)

Oxide Distribution in PBF-LB/M-Processed ODS Steel: Effects of Ball Milling and Dielectrophoretic Deposition in Powder Production.

Powder Metallurgy, 68 (1), 29-40

DOI: 10.1177/00325899241304735

CRediT Authorship Contribution of Mareen Goßling: conceptualization (lead), writing – original draft (lead) and investigation.

3.3.1 Objective

This study compared two additivation techniques—BM and DD—for incorporating 1 vol% Y_2O_3 NPs into Fe20Cr powder. The goal was to assess how each method affects powder morphology, NP retention, and the resulting distribution and size of NPs in PBF-LB/M parts. These findings directly inform Research Questions 1 and 3.

3.3.2 Key Findings

Both methods enabled production of dense parts (>99.8% relative density). DD preserved powder morphology and achieved slightly finer and more homogeneous NP dispersion (74 nm size, 826 nm IPD) compared to BM/120 min (77 nm, 790 nm) and BM/40 min (108 nm, 1114 nm). SEM confirmed better surface coating via DD, while BM induced minor deformation.

Powder flowability and packing density were superior for DD (Hausner ratio 1.09, packing density 50.5%), due to the spherical morphology and reduced interparticle friction. Yttrium retention decreased during processing for both methods (~65–70% loss), attributed to evaporation and ejection effects.

Although all methods enabled NP integration, DD resulted in a more favorable combination of dispersion, flowability, and powder morphology. Notably, differences in NP positioning—embedded in BM vs. surface-coated in DD—influence NP–melt interaction, affecting final distribution.

3.3.3 Conclusion

Both BM and DD are suitable for preparing ODS feedstocks for PBF-LB/M. However, DD achieved slightly better NP dispersion and powder handling characteristics. Despite similar Y_2O_3 loadings, DD showed slightly reduced Y content in the final part, underlining integration challenges in AM. These results emphasize the importance of optimized additivation strategies for achieving homogeneous NP distribution and highlight DD as a promising route for future development.

3.4 Study III

Goßling, M., Rittinghaus, S.-K., Radtke, F., Elsayed, A., Barrientos, M. M., Ziesing, U., Becker, L., Kuşoğlu, I.M., Broeckmann, C., Krupp, U., Hariharan, A., Weber, S., Gökce, B. (2025)

Mechanical and Microstructural Effects of ZrO_2 Nanoparticles in Fe20Cr Oxide Dispersion-Strengthened Alloys Processed by Laser Powder Bed Fusion

Advanced Engineering Materials, 2500317

DOI: 10.1002/adem.202500317

CRediT Authorship Contribution of Mareen Goßling: Conceptualization (equal), Writing - Original Draft (lead), Investigation

3.4.1 Objective

Study III examined how the synthesis route and loading of ZrO_2 NPs influence their integration, distribution, and strengthening behaviour in Fe20Cr ODS steels fabricated by PBF-LB/M. Chemically synthesized and laser-generated NPs were each added at 0.1 and 1.0 vol%, allowing comparison under standardized processing conditions. The study focused on how initial NP features (size, morphology, crystallographic phase) affect dispersion, IPD, grain evolution, and mechanical performance after PBF-LB/M and HT.

3.4.2 Key Findings

Laser-generated NPs exhibited narrow size distributions (D_{90}≈10 nm) and a tetragonal phase, resulting in fine grain structures (~0.45 µm at 0.1 vol%) in the AB state. Chemically synthesized NPs were larger (D_{90}≈1257 nm, monoclinic) and less uniform but enabled better grain size stability post-HT.

Agglomeration was more pronounced in high-loading (1.0 vol%) laser NP samples, which increased IPD (734 ± 475 nm) and reduced particle integration, despite favorable initial dispersion. Compression testing at 600 °C showed the highest flow stress (252 ± 7 MPa) for samples with 0.1 vol% chemical synthesized NPs, correlating with small grains and moderate IPD. Creep testing at 600 °C and 50 MPa, however, identified samples with 1.0 vol% Laser generated NPs as the best performer ($5.0 \times 10^{-8}\,s^{-1}$), despite larger IPD, due to retained small NP size and higher particle count.

Thus, short-term strength correlated with grain size, whereas long-term creep resistance was more sensitive to NP retention and dispersion quality. Excessive NP loading (1.0 vol% laser-generated) led to clustering but still outperformed other variants in creep resistance due to its fine, stable dispersoids.

3.4.3 Conclusion

Study III highlights the interplay between NP type, size, and dispersion in determining microstructure and mechanical response. Laser-generated NPs provide initial benefits in refinement and dispersion but show limitations at higher concentrations due to agglomeration. Chemically synthesized NPs offer better stability after HT and perform more consistently at lower loadings.

The findings emphasize that high creep resistance is achieved through stable, finely dispersed NPs at sufficient concentrations, while short-term strength is governed by grain size. These results provide a clear pathway for tailoring NP-based strengthening strategies in AM-processed ODS steels.

4. Integration of Findings and Discussion

This chapter discusses the core findings of the three studies in direct relation to the research questions posed at the beginning of this work. Rather than restating individual results, the aim is to provide a thematic synthesis that clarifies where the studies align, diverge, or expand on existing knowledge, and how they collectively deepen our understanding of NP-reinforced ODS steels under PBF-LB/M conditions.

The discussion is structured around four central research questions:

1) How and why do NP characteristics (size, morphology, chemistry) evolve from powder to solid part during the LPBF-LB/M process?
2) How do theoretical predictions (e.g., by Rösler and Arzt) for NP size and interparticle distance in the solid part correlate with experimental results?
3) How do different NP sizes and interparticle distances affect grain growth and NP characteristics (e.g., size and spacing) in rapidly solidified microstructures and after heat treatment?
4) How are NP size and distribution correlated with fundamental mechanical properties such as strength and creep resistance?

Special attention is given to the NP synthesis and additivation strategies, as these were identified as key parameters influencing dispersion quality, integration, and strengthening effectiveness. The chapter concludes with a summary of the research questions and outlines implications for the future design and integration of oxide NPs in elevated temperature AM applications.

4.1 Nanoparticle Evolution during PBF-LB/M: From Powder to Part

The first research question of this dissertation addresses how and why NP characteristics—such as size, morphology, distribution, and phase—change during the PBF-LB/M process. While initial properties are determined by the synthesis route, it is the thermal and fluid-dynamic environment of the melt pool that governs their transformation and retention in the final part.

Across all three studies, a clear trend of NP loss was observed during processing. Particularly in samples prepared via DD, where particles are attached to the surface, significant losses occurred—due to ejection, evaporation, or insufficient embedding. BM, in contrast, facilitated deeper particle integration into the powder and resulted in higher retention. For example, Y retention in Study II reached 0.22 wt% for BM compared to 0.15 wt% for DD. This leads to the conclusion that integration and dispersion also correlate with particle positioning. While DD enables more uniform surface coating and smaller final NP sizes, it exposes particles directly to the melt pool, increasing the risk of loss. BM, in contrast, sacrifices some homogeneity but enhances thermal shielding.

Study III showed that laser-generated ZrO_2 NPs, although initially fine ($D_{90} \approx 10$ nm), were susceptible to agglomeration and coarsening. Chemically synthesized ZrO_2 NPs, despite a much broader and larger size distribution ($D_{90} > 1200$ nm), remained more size stable during PBF-LB/M. This may be due to weaker van der Waals forces acting between the larger particles, combined with their lower number density in the melt pool—reducing collision frequency and aggregation.

In addition the SEM and ECCI analysis in Study III showed that ZrO_2 NPs tend to segregate to grain boundaries during solidification—likely due to being pushed ahead of the solid–liquid interface, a

phenomenon described in prior AM literature [83–85]. Notably, the applied scan speeds (up to 915 mm/s) were lower than those in other studies that achieved full NP embedding (1600 mm/s in [89]), potentially limiting retention. Compared to other laser-based AM systems in the literature, which typically operate with laser spot sizes of 80–150 µm, the Aconity MINI system used in Studies I–III features a smaller spot diameter of 50 µm. This reduced spot size results in smaller melt pools and higher cooling rates, yet it appears insufficient to fully prevent NP segregation.

Complementary findings from Studies I, II and III point toward a lower agglomeration tendency for ZrO_2 compared to Y_2O_3, supported by numerical simulations in Study I and experimentally verified in Study II with SEM and Study III via ECCI and SEM. For instance, the average IPD for ZrO_2 was 445 ± 309 nm, while Y_2O_3 reached 826 ± 103 nm at the same volumetric loading (cf. Figure 4). This difference occurred despite Y_2O_3's finer initial size, suggesting that small particles are more prone to clustering due to stronger surface forces and higher number density (cf. Figure 5). The potential influence of material constants—such as the Hamaker constant—was initially modeled in Study I and may partly explain the superior dispersion of ZrO_2. However, a direct comparison using matched particle size and morphology would be necessary to isolate material-specific effects from those arising due to synthesis or integration. Differences in imaging sensitivity and particle statistics between studies further complicate this interpretation and highlight the need for consistent analysis protocols.

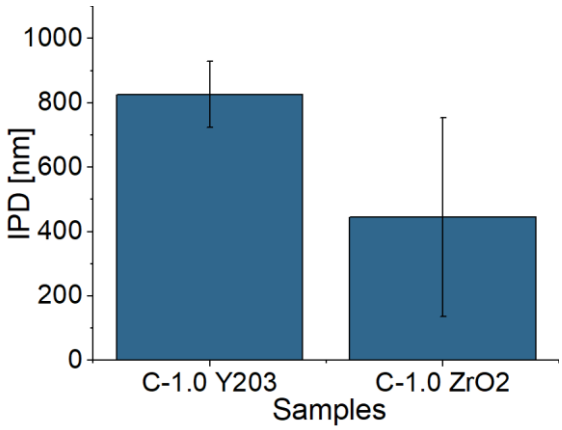

Figure 4 Interparticle distance of PBF-LB/M Samples containing 1 vol% of chemically produced Y_2O_3 and ZrO_2 additivaded via dielectrophoretic deposition onto Fe20Cr pre-processing.

However, a direct comparison is complicated by differences in the initial NP properties, which arise from varying suppliers and synthesis methods (see Figure 5). The Y_2O_3 particles in Study II had nominal sizes of 32–36 nm, with undefined morphology ranging from spherical to plate-like (c-e). X-ray diffraction (XRD) confirmed a cubic crystal structure (a). In contrast, the ZrO_2 NPs used in Study III exhibited a significantly broader size distribution (D_{90} > 1200 nm), dendritic morphology (f, g), and a monoclinic crystal structure (b), with only a small fraction of sub-20 nm spherical particles(h). These differences in size, morphology, and crystal structure must be considered alongside the Hamaker constant when interpreting agglomeration behaviour.

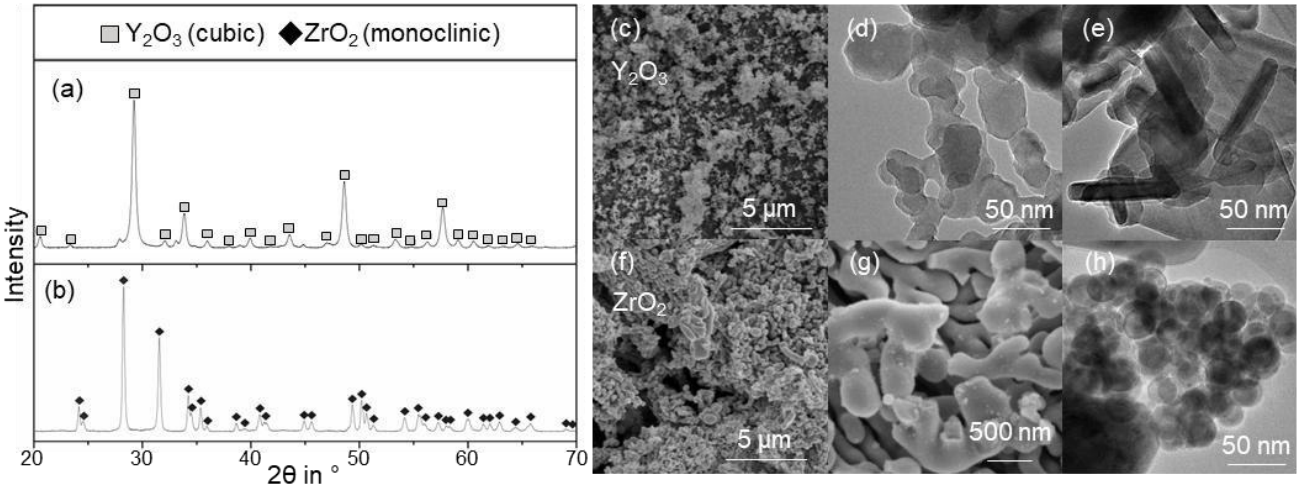

Figure 5 XRD of chemically produced ZrO_2(a), Y_2O_3(b) and electron imaging in different magnifications of ZrO_2 (c-e) and Y_2O_3 (f-h)

The role of synthesis method becomes even more apparent when considering phase stability. Laser-generated ZrO_2 showed a tetragonal structure, while chemically produced ZrO_2 particles were monoclinic. No direct phase transformation was observed during processing, but the tetragonal phase may be metastable and sensitive to thermal or residual stress. Whether phase changes occur during PBF-LB/M or post-processing remains an open question and warrants further study, for instance using ATOM PROBE TOMOGRAPHY (APT) or TEM.

In summary, the evolution of NPs during PBF-LB/M depends not only on their initial size and phase, but on their ability to withstand rapid thermal cycling, survive melt pool turbulence, and avoid clustering. While laser-generated NPs offer ideal starting characteristics, chemically synthesized particles proved more stable and better retained. Thus, successful NP integration requires balancing initial morphology, embedding depth, and compatibility with the process conditions.

4.2 Nanoparticle Spacing and Deviation from Theoretical Models

The second research question examines how theoretical predictions regarding optimal NP (NP) size and IPD—such as those proposed by Rösler, Arzt, and Scattergood & Bacon—compare with experimental observations in PBF-LB/M-processed ODS steels. While these models offer useful frameworks for maximizing Orowan strengthening (e.g., particles <10 nm, closely spaced, thermally stable), their assumptions often diverge from the complexities of AM practice.

The model by Scattergood and Bacon [108] introduced a combined parameter $X = \left(\frac{1}{R} - \frac{1}{L}\right)^{-1}$, linking particle radius R and spacing L to account for dislocation bowing between obstacles. As R decreases, the required bypass stress increases—but only under the condition of uniform, non-agglomerated particles. Conversely, larger particles can achieve similar strengthening effects at wider spacing. This trade-off between particle size and spacing is critical for translating idealized Orowan strengthening into processable alloy systems. However, implementing such theoretical ideals in AM practice is challenging, as demonstrated by the experimental data from Studies II and III.

Study II provided the first experimental IPD data for PBF-LB/M-processed Fe20Cr steels containing chemically synthesized Y_2O_3. IPDs ranged from 826 to 1114 nm, with average particle diameters between 74 and 108 nm—well above theoretical targets. Although DD improved particle dispersion and flowability, clustering and partial sintering during processing limited spacing control.

Study III expanded this view by comparing ZrO_2 particles produced via LAL and sol-gel synthesis. Despite a higher IPD (~734 ± 475 nm) for laser-generated NPs, the corresponding sample showed the lowest steady-state creep rate—linked to the smallest retained particle size post-processing. Chemically synthesized ZrO_2 yielded closer spacing (445 ± 309 nm), but slightly lower creep performance, highlighting that particle size and stability can outweigh IPD as dominant factors in long-term strengthening.

These findings challenge the assumption that spacing alone governs Orowan strengthening. Especially under high-temperature loading, particle coarsening resistance and final retained size appear more critical than perfect spacing. This shift in perspective is essential when designing alloys for creep resistance under rapid thermal cycling.

It should be noted, however, that the applied imaging techniques (SEM, ECCI) impose detection limits (~20–50 nm in SEM; ~10–15 nm in ECCI), overlooking smaller, yet strengthening-relevant particles. Furthermore, all IPDs were derived from 2D images, introducing stereological uncertainty. Advanced techniques such as TEM or APT would be required for precise 3D quantification but were beyond the scope of this study. In contrast to idealized assumptions, AM introduces unavoidable deviations through particle agglomeration during feedstock preparation, coarsening during melting, and segregation during solidification. Even monodisperse, laser-generated NPs (~10 nm) tend to form larger clusters under specific process conditions. Chemically synthesized particles, though larger initially, exhibited better thermal stability and unexpectedly tighter spacing after consolidation.

Unlike traditional ODS processing—which relies on long-term thermomechanical treatment to achieve optimal NP distributions—PBF-LB/M benefits from rapid solidification, producing ultrafine grains (~10–20 µm) that respond well to Zener pinning, partially compensating for suboptimal NP spacing. Taken together, the results suggest three practical strategies: First, achieving a well-defined small initial particle size is crucial, as demonstrated by the superior consolidation behaviour of laser-generated NPs; even when agglomerated, they retain advantageous dimensions post-processing. Second, agglomeration prior to melting must be minimized by selecting chemically stable oxide types (e.g., ZrO_2 over Y_2O_3) and employing additivation methods that minimize direct NP–NP contact and reduce the risk of agglomeration prior to melting. Third, agglomeration during melting can be suppressed by limiting melt pool dimensions and enhancing solidification rates, thereby reducing turbulent flow and particle mobility. While exact control remains difficult in practice, these findings suggest that targeting the minimal NP content necessary for effective strengthening—while preserving dispersion stability—may offer a more robust path than simply maximizing volume fraction.

4.3 Grain Structure Evolution and Thermal Stability

The third research question of this dissertation addresses the influence of NP size and distribution—specifically IPD —on grain growth and microstructural stability in PBF-LB/M-processed ODS steels. This includes the grain structure in the AB condition as well as after HT.

Study III showed that laser-generated ZrO_2 NPs, with narrow size distributions (~10 nm) and a tetragonal phase, led to significant grain refinement in the AB state (average grain size ~1 µm). This aligns with literature findings, where finer oxide dispersoids (~5 nm) promote stronger grain boundary pinning and grain sizes below 300 nm, compared to coarser particles (~12 nm) which result in larger grains and lower creep resistance [44].

This refinement is due to multiple factors: the small size and uniform dispersion of laser-generated NPs, their clean surfaces from LAL synthesis, and potentially favorable wetting and interfacial energies that support heterogeneous nucleation during rapid solidification. Their tetragonal crystal structure may also foster orientation relationships with the ferritic matrix, though it remains unclear whether refinement arises from nucleation effects, delayed recrystallization, or Zener pinning. Further high-resolution characterization is needed to clarify the dominant mechanism.

However, HT resulted in substantial grain coarsening in these samples—up to 25 µm for 1 vol% laser-generated ZrO_2—along with pronounced grain anisotropy. In contrast, samples with chemically synthesized ZrO_2 NPs, which had coarser initial grains (~5 µm at 0.1 vol%), retained or even refined their grain structure after HT (~1 µm). This suggests that despite their size, chemically synthesized NPs offer improved long-term stability, due to higher interfacial energy and lattice mismatch, which promote particle-stimulated nucleation or stable boundary pinning.

These differences highlight the importance of particle–matrix interactions. Small NPs (<10 nm) are often coherent or semi-coherent with the matrix, enabling strong dislocation interactions and grain stabilization. Larger NPs (>20 nm), while stronger obstacles, tend to become incoherent, reducing ductility and stability at elevated temperatures. [47, 48] Coherency is also influenced by lattice mismatch, synthesis route, and potential stress relaxation during HT, which may trigger loss of coherency.

Study I, which used the same type and concentration of laser-generated ZrO_2 NPs as Study III, did not report grain refinement—due to the limited resolution of optical microscopy. EBSD data from Study III suggest that refinement would have been detectable with more sensitive techniques. Study II, though lacking direct grain size data, supports these findings indirectly. It showed that DD yields finer NP dispersion and shorter IPDs than BM—factors known to enhance grain refinement and thermal stability. These outcomes were later confirmed in Study III using powders derived from DD.

In conclusion, NP size, spacing, and interface characteristics (e.g., wettability, coherency) play a significant role in controlling grain evolution in ODS steels. Laser-generated NPs support pronounced refinement in the AB state but are less stable during HT, while chemically synthesized NPs—despite coarser morphology—contribute to improved grain stability post-treatment, particularly at lower loading levels.

4.4 Mechanical Response: Strengthening Mechanisms and Creep Behaviour

The final research question examines how NP size and distribution influence the mechanical behaviour of PBF-LB/M-processed Fe20Cr-based ODS steels, with particular focus on strength and creep resistance. Insights are drawn primarily from Studies I and III, evaluating the role of grain refinement, Orowan strengthening, and NP stability.

In Study I, 1.0 vol% laser-generated ZrO_2 NPs led to moderate room-temperature hardness (217 HV0.1), but no grain refinement was detected—due to the limited resolution of LOM, which cannot resolve submicron grains. However, Study III, using the same NP type and concentration, confirmed significant grain refinement (~1 µm) via EBSD. This suggests that refinement effects were present in Study I but remained undetected. The comparatively lower mechanical performance may also reflect a reduced part density (~98%) relative to the ~99–99.9% densities achieved in Study III, which limits absolute strengthening.

In contrast, Study III established a clearer correlation between NP characteristics and mechanical response. Compression tests at 600 °C showed the highest flow stress (252 ± 7 MPa) in samples with 0.1 vol% chemically synthesized ZrO_2 NPs, which retained a refined grain structure (~1 µm) after HT. This is attributed to effective grain boundary pinning by coarser, thermally stable NPs with moderate IPD (520 ± 348 nm). Meanwhile, the sample with 1 vol% laser-generated ZrO_2—despite exhibiting higher hardness in the AB state (171 HV1)—showed lower flow stress (229 ± 12 MPa) post-HT, highlighting that fine NPs alone do not ensure superior high-temperature strength if grain coarsening and anisotropy occur.

Creep testing at 600 °C and 50 MPa provided further insights into long-term performance. The 1 vol% laser-generated ZrO_2 sample exhibited the lowest steady-state creep rate (5.0×10^{-8} s^{-1}), outperforming both the chemically synthesized NP variant (7.0×10^{-8} s^{-1}) and the reference alloy. This enhanced creep resistance is attributed to the small, retained particle size and high NP number density, which enable effective Orowan pinning—even at larger average IPD.

Taken together, the studies demonstrate that mechanical behaviour in AM-processed ODS steels is governed by timescale-dependent mechanisms: grain refinement dominates under short-term high-temperature loads, while dispersoid size and stability control long-term creep resistance. Hence, tailoring mechanical performance requires careful optimization of both NP synthesis and integration strategies, balancing initial refinement with thermal stability throughout processing and application.

4.5 Analytical Limitations and Sources of Uncertainty

Although the three studies presented in this dissertation offer important insights into NP integration and performance in PBF-LB/M-processed ODS steels, analytical and methodological limitations must be acknowledged.

A primary constraint lies in the resolution of the imaging techniques used to characterize NP size and distribution. SEM and ECCI limited reliable detection to particles larger than ~20–50 nm and ~10–15 nm, respectively. As a result, the smallest and potentially most effective NPs—especially in laser-generated systems—may have gone undetected. Moreover, IPDs were derived from 2D surface sections and extrapolated into 3D via stereological assumptions. While large datasets were used (e.g., ~13,000 particles in Study III), inherent uncertainties remain—particularly in cases of clustered or anisotropic dispersions. Access to high-resolution methods such as TEM, APT, or selected area electron diffraction was limited. Consequently, critical parameters such as coherency state, elemental partitioning, or phase transformation (e.g., tetragonal-to-monoclinic ZrO_2) could not be directly confirmed and remain speculative.

In terms of mechanical testing, creep experiments in Study III were conducted as single-point trials due to time constraints. Although general trends correspond well with microstructural findings, the lack of replication introduces uncertainty in absolute creep rates. Additionally, the Y_2O_3 and ZrO_2 particles used in Studies II and III originated from different suppliers and synthesis routes, affecting their surface chemistry, morphology, and dispersion behaviour—factors that could not be fully decoupled from the integration strategy. Finally, while the simplified Fe20Cr model alloy enabled controlled comparisons and mechanistic insights, it limits the direct transferability of results to industrial-grade ODS steels with more complex chemistries.

Despite these limitations, all experiments applied consistent imaging, stereological, and quantification protocols. This methodological continuity allows for robust relative comparisons

across studies and supports the validity of observed structure–property relationships. Nonetheless, future investigations should include nanoscale characterization and replicated mechanical testing to further substantiate and extend the findings presented here.

4.6 Implementation for Additive Manufacturing

The integration of laser-generated oxide NPs into metal powders offers a promising pathway for producing high-performance components for high-temperature applications in AM. LAL enables the synthesis of high-purity, size-controlled oxide NPs without environmentally harmful by-products. Although current production capacities (~1 g/h) remain at the laboratory scale, the method aligns well with regulatory demands due to its moderate energy requirements and chemical-free processing, providing a sustainable foundation for future upscaling.

Compatibility with established AM workflows has been confirmed. In particular, the combination of LAL and DD allows for the integration of oxide NPs into Fe20Cr powders while preserving powder sphericity and flowability. PBF-LB/M builds with 1 vol% NP loading achieved relative densities of up to 99.9%.. However, further optimization is required when transferring NP-DD-loaded powders to other AM platforms such as Electron Beam Melting or DED. Although initial trials in Electron Beam Melting and DED are promising, specific interactions with shielding gases or vacuum conditions may lead to NP evaporation or defect formation.

Tailored NP dispersions enable microstructure control, offering new alloy design strategies. For instance, LAL-derived tetragonal ZrO_2 contributed to grain refinement and enhanced creep resistance at 600 °C. However, its effect on strength at lower temperatures was limited. Additionally, Fe20Cr must be further alloyed (e.g., with Al or Ti) to meet industrial mechanical property targets.

From a practical perspective, key implementation challenges include reproducibility and powder recyclability. Batch-to-batch variation in NP content and limited data on powder reuse may impair process reliability. Although the AM process chain is largely compatible with standard routines, consistent mechanical performance will require optimized heat treatment strategies tailored to oxide-reinforced systems.

In summary, combining LAL and AM offers a viable route for designing oxide-strengthened alloys with customizable microstructures and improved thermal performance. Future work should focus on refining powder integration, processing stability, and scaling pathways to bridge the gap between laboratory validation and industrial application.

4.7 Research Outlook

Building on the findings of this dissertation, several research directions are essential for translating LAL-based oxide NP integration into reliable AM practice.

Scalability and Automation: To meet industrial demand, LAL systems must evolve beyond batch processing. Future research should focus on continuous, automated production systems with inline monitoring to ensure consistent particle characteristics and high-throughput synthesis (>100 g/h), while retaining LAL's environmentally sustainable advantages.

Feedstock Robustness and Recycling: Reliable powder properties are critical for industrial adoption. Investigations should address long-term storage stability, powder reuse, and the impact of NP

content variation on processability and part performance. This includes the development of standard quality metrics for NP-loaded powders and their recyclability.

Alloy System Expansion: While Fe20Cr served as an ideal model system, the methodology must be extended to application-relevant alloys. Future studies should examine how laser-generated NPs interact with more complex alloy chemistries during melting and solidification. Alloying strategies incorporating Al, Ti, or rare earths must be systematically combined with tailored NP designs to meet mechanical, oxidation, and corrosion resistance demands.

High-Temperature Validation: While short-term creep testing has demonstrated the feasibility of NP-based reinforcement, real-world validation requires long-duration tests under mechanical and environmental loads. Such testing will be essential for structural components in energy, aerospace, or nuclear systems and should be paired with in-depth microstructural tracking to correlate NP evolution with long-term behaviour.

Microstructure Engineering and Simulation: Advanced simulations—such as CALPHAD and phase-field modeling—can accelerate the design of oxide-dispersed AM alloys with predictable properties. Coupling these models with experimental data on NP retention, morphology, and dispersion will enable rational alloy design tailored to specific service conditions.

Alternative AM Platforms and Transferability: Exploring the transfer of NP-loaded feedstocks to AM methods beyond PBF-LB/M—such as DED or high-speed cladding—could open new applications, including component repair and surface functionalization. Here, process-specific adjustments (e.g., laser-material interaction tuning) will be required to preserve NP benefits.

Sustainability and Safety: In addition to technical performance, future research must address environmental and occupational safety aspects. These include NP behaviour during powder handling, potential fume generation, and inhalation risks. Lifecycle assessments and safe-by-design strategies should be integrated from the outset.

In summary, the combined use of LAL and AM forms a flexible and sustainable platform for engineering high-performance alloys. Unlocking its full potential requires interdisciplinary collaboration spanning materials science, process engineering, safety research, and digital design—paving the way toward robust industrial implementation.

4.8 Answers to the Research Questions

The overarching aim of this dissertation was to understand the influence of NP characteristics—such as size, distribution, and phase composition—and their integration strategy on the microstructural evolution and mechanical performance of Fe20Cr-based ODS steels fabricated by PBF-LB/M. Based on the cumulative insights gained across Studies I to III, this section provides concise, research-question-focused answers that consolidate the thematic findings discussed in the previous sections.

1) How and why do NP characteristics (size, morphology, phase, distribution) evolve from powder to solid part during PBF-LB/M?

NP evolution is strongly influenced by the thermal gradients and melt pool dynamics of PBF-LB/M. Laser-generated ZrO_2 NPs, although initially fine (~3.8 nm median), tend to agglomerate, coarsen, and partially dissolve—particularly at higher loadings—due to recoil pressure and insufficient embedding. In contrast, larger, chemically synthesized NPs exhibit better morphological stability, due

to reduced solubility and lower collision frequency. Integration method plays a key role: BM results in deeper embedding and better integration, while DD offers improved initial dispersion but exposes NPs more directly to melt pool effects. Overall, both synthesis route and additivation strategy determine how effectively NPs are retained and transformed during processing.

2) How do theoretical predictions regarding optimal NP size and interparticle distance compare with experimental results?

While theoretical models suggest optimal strengthening with sub-10 nm particles and narrow, uniform IPD, experimental data show significantly larger particle sizes (74–108 nm) and IPDs (445–1114 nm). Despite this deviation, the sample with the largest IPD (1 vol% laser-generated ZrO_2) exhibited the best creep resistance, attributed to the presence of small, stable particles post-processing. This suggests that, under AM conditions, retained particle size and thermal stability may outweigh geometric ideals such as tight spacing or theoretical dimensions—particularly in creep-dominated applications.

3) How do NP size and interparticle distance affect grain growth and microstructural stability before and after heat treatment?

Laser-generated ZrO_2 NPs promoted significant grain refinement in the AB state (~1 µm), but these fine grains coarsened during HT, reflecting limited long-term stability. Chemically synthesized NPs, though initially coarser, maintained finer grains after HT, particularly at low concentrations (0.1 vol%). This indicates more effective Zener pinning. Beyond size and spacing, crystallographic phase also plays a role: metastable tetragonal phases (laser-generated) appear less persistent under thermal exposure than the monoclinic phases (chemically synthesized), which support sustained grain boundary stabilization.

4) How are NP size and distribution correlated with fundamental mechanical properties such as strength and creep resistance?

Mechanical behaviour is governed by different mechanisms depending on timescale and temperature. Under short-term high-temperature compression, strength increased with decreasing grain size: the highest flow stress (252 MPa) was observed for 0.1 vol% chemically synthesized ZrO_2 NPs, which retained refined grains after HT. In contrast, long-term creep resistance correlated more closely with dispersoid stability and size: the sample with 1 vol% laser-generated NPs exhibited the lowest creep rate ($5.0 \times 10^{-8}\ s^{-1}$), despite a wider IPD, due to its high number density of small, retained particles. This confirms that grain boundary strengthening dominates short-term behaviour, whereas Orowan-type mechanisms from stable dispersoids govern long-term performance.

5. Conclusion and Future Work

This dissertation explored how NP characteristics—such as size, morphology, and phase composition—as well as their additivation strategies affect microstructure formation and mechanical performance in additively manufactured Fe20Cr-based ODS steels. By systematically comparing different NP types (laser-synthesized vs. chemically produced ZrO_2) and additivation methods (BM vs. DD), this work aimed to identify the mechanisms governing NP behaviour during LBF-LB/M and their contribution to alloy strengthening.

5.1 Summary of Key Contributions

The table below summarizes how the presented studies address existing gaps in the field and contribute novel insights into the design and processing of ODS alloys for AM:

State of the Art	**Contribution of this Work**
Isolated studies on various NP/matrix combinations	Direct comparison of laser-generated and chemically synthesized ZrO_2, under controlled conditions along the entire PBF-LB/M chain
Limited data on NP evolution	Multi-stage analysis of NP transformation from synthesis to consolidated part (size, morphology, integration)
Overlapping strengthening mechanisms	Differentiation of Orowan and grain boundary effects via Fe20Cr model alloy and systematic variation of NP type and volume
Limited data on NP retention	Quantitative retention analysis via XRF before/after AM and correlation with mechanical properties
Low-resolution or localized IPD data	High-resolution particle mapping and IPD statistics across multiple studies
Lack of comparative analysis between BM and DD	First systematic comparison in identical alloy + AM parameter setup
Unclear effects of NP morphology and phase	Correlation between NP phase (tetragonal vs. monoclinic) and thermal stability in PBF-LB/M processed Fe20Cr
Focus on initial strength only	Inclusion of long-term creep testing for different NP systems
Focus on TEM-scale characterization with low statistical validity	Statistically robust analysis of >13,000 NPs using ECCI and automated image quantification
Lack of IPD validation	Experimental vs. theoretical IPD comparison
Narrow focus on Y_2O_3-based ODS systems studied	Expanded scope to ZrO_2 systems with two crystal structures (monoclinic/tetragonal)
AM parameter studies often decoupled from NP behaviour	Standardized AM parameters across all powders to isolate NP effects
Unclear relationship between NP retention, spacing and creep	Showed that NP size and retention, not IPD alone, govern creep resistance

5.2 Overarching Synthesis of the Work

The results of this dissertation support the core finding that the performance of ODS steels in AM is not determined by the initial properties of the oxide NPs alone, but by their process stability—their ability to maintain a favorable size, distribution, and phase during thermal cycling and consolidation. While this concept has been discussed in theory, this work provides one of the first quantitative experimental demonstrations linking NP synthesis route, process-induced transformations, and mechanical performance under standardized conditions.

Two key insights emerge:

- Short-term strength is governed by grain refinement, which is promoted by fine, closely spaced NPs that limit grain growth during solidification and HT.
- Long-term creep resistance, in contrast, is controlled by retained NP size and stability after thermal exposure—even in systems with large IPDs.

These results highlight the importance of application-specific alloy design strategies: tailoring NP type and integration method not only to the process, but to the expected service conditions. This perspective is still underrepresented in current AM-focused ODS research, which often prioritizes printability over long-term performance.

From a methodological viewpoint, the dissertation offers three advances:

- A controlled comparison of BM and DD for NP additivation in AM powders, highlighting trade-offs between dispersion quality and particle integration.
- High-throughput, image-based quantification of NP distributions to statistically support structure–property correlations.
- Isolation of NP synthesis effects by controlling alloy composition and process parameters across all experiments.

Taken together, these findings support a shift toward mechanism-informed NP integration in ODS alloy development—moving away from empirical powder modification and toward reproducible, design-driven strategies. The framework developed here is applicable beyond Fe20Cr and PBF-LB/M and may support the design of future high-temperature alloys for energy and aerospace applications.

By revisiting the original motivation—to support more efficient, thermally robust materials for decarbonized energy systems—this dissertation contributes to enabling a more sustainable, performance-focused use of AM in structural materials design.

References

1 Stępień, Z. (2021) A Comprehensive Overview of Hydrogen-Fueled Internal Combustion Engines: Achievements and Future Challenges. *Energies*, **14** (20), 6504.

2 Olhoff, A., Bataille, C., Christensen, J., Elzen, M. den, Fransen, T., Grant, N., Blok, K., Kejun, J., Soubeyran, E., Lamb, W., Levin, K., Portugal-Pereira, J., Pathak, M., Kuramochi, T., Strinati, C., Roe, S., Rogelj, J. (2024) *Emissions Gap Report 2024: No more hot air … please! With a massive gap between rhetoric and reality, countries draft new climate commitments*, United Nations Environment Programme.

3 Intergovernmental Panel on Climate Change (ed) (2023) *Climate Change 2023: Synthesis Report. Contribution of Working Groups I, II and III to the Sixth Assessment Report of the Intergovernmental Panel on Climate Change (AR6)*, Geneva, Switzerland.

4 *World Energy Outlook 2019* (2019), International Energy Agency, Paris.

5 Vasserman, A.A. and Shutenko, M.A. (2017) Methods of increasing thermal efficiency of steam and gas turbine plants. *J. Phys.: Conf. Ser.*, **891**, 12248.

6 Gao, J., Wang, X., Song, P., Tian, G., Ma, C. (2022) Review of the backfire occurrences and control strategies for port hydrogen injection internal combustion engines. *Fuel*, **307**, 121553.

7 Eswarappa Prameela, S., Pollock, T.M., Raabe, D., Meyers, M.A., Aitkaliyeva, A., Chintersingh, K.-L., Cordero, Z.C., Graham-Brady, L. (2023) Materials for extreme environments. *Nat Rev Mater*, **8** (2), 81–88.

8 Kimura, A., Kasada, R., Iwata, N., Kishimoto, H., Zhang, C.H., Isselin, J., Dou, P., Lee, J.H., Muthukumar, N., Okuda, T., Inoue, M., Ukai, S., Ohnuki, S., Fujisawa, T., Abe, T.F. (2011) Development of Al added high-Cr ODS steels for fuel cladding of next generation nuclear systems. *Journal of Nuclear Materials*, **417** (1-3), 176–179.

9 Li, X.P., Ji, G., Chen, Z., Addad, A., Wu, Y., Wang, H.W., Vleugels, J., van Humbeeck, J., Kruth, J.P. (2017) Selective laser melting of nano-TiB2 decorated AlSi10Mg alloy with high fracture strength and ductility. *Acta Materialia*, **129**, 183–193.

10 Wang, P., Gammer, C., Brenne, F., Niendorf, T., Eckert, J., Scudino, S. (2018) A heat treatable TiB2/Al-3.5Cu-1.5Mg-1Si composite fabricated by selective laser melting: Microstructure, heat treatment and mechanical properties. *Composites Part B: Engineering*, **147**, 162–168.

11 Hall, E.O. (1951) The Deformation and Ageing of Mild Steel: III Discussion of Results. *Proc. Phys. Soc. B*, **64** (9), 747–753.

12 Meyers, M.A. and Chawla, K.K. (2012) *Mechanical Behavior of Materials*, Cambridge University Press, Cambridge.

13 Martin, J.H., Yahata, B.D., Hundley, J.M., Mayer, J.A., Schaedler, T.A., Pollock, T.M. (2017) 3D printing of high-strength aluminium alloys. *Nature*, **549** (7672), 365–369.

14 Chawla, V., Prakash, S., Sidhu, B.S. (2007) State of the Art: Applications of Mechanically Alloyed Nanomaterials—A Review. *Materials and Manufacturing Processes*, **22** (4), 469–473.

15 Wilms, M.B., Rittinghaus, S.-K., Goßling, M., Gökce, B. (2023) Additive manufacturing of oxide-dispersion strengthened alloys: Materials, synthesis and manufacturing. *Progress in Materials Science*, **133**, 101049.

16 Gu, D., Shi, X., Poprawe, R., Bourell, D.L., Setchi, R., Zhu, J. (2021) Material-structure-performance integrated laser-metal additive manufacturing. *Science (New York, N.Y.)*, **372** (6545).

17 Pilone, D., Pulci, G., Paglia, L., Mondal, A., Marra, F., Felli, F., Brotzu, A. (2020) Mechanical Behaviour of an Al2O3 Dispersion Strengthened γTiAl Alloy Produced by Centrifugal Casting. *Metals*, **10** (11), 1457.
18 Tang, H., Chen, X., Chen, M., Zuo, L., Hou, B., Wang, Z. (2014) Microstructure and mechanical property of in-situ nano-particle strengthened ferritic steel by novel internal oxidation. *Materials Science and Engineering: A*, **609**, 293–299.
19 Tang, Y., Yang, S., Zhao, Y.F. (2016) Sustainable Design for Additive Manufacturing Through Functionality Integration and Part Consolidation, in *Handbook of Sustainability in Additive Manufacturing* (eds S.S. Muthu and M.M. Savalani), Springer Singapore, Singapore, pp. 101–144.
20 Liu, W., Liu, X., Liu, Y., Wang, J., Evans, S., Yang, M. (2023) Unpacking Additive Manufacturing Challenges and Opportunities in Moving towards Sustainability: An Exploratory Study. *Sustainability*, **15** (4), 3827.
21 Cai, Y., Wang, L., Li, J., Yang, M., Feng, Q., Liu, T. (2023) *Influences of Adding Y2ti2o7 and Hfh1.98 Nanoparticles on the Microstructure and Mechanical Properties of Oxide Dispersion Strengthen Steels*.
22 Ashong, A.N., Na, M.Y., Chang, H.J., Park, T., Jun, G.U., Noh, S., Kim, J.H. (2022) Manganese effect on the microstructural transformation and mechanical properties of oxide dispersion strengthened steels fabricated with pre-alloyed powders. *Materials Science and Engineering: A*, **830**, 142282.
23 Zhang, Z. and Pantleon, W. (2018) Response of oxide nanoparticles in an oxide dispersion strengthened steel to dynamic plastic deformation. *Acta Materialia*, **149**, 235–247.
24 Wassermann, N.A., Li, Y., Myers, A.J., Kantzos, C.A., Smith, T.M., Beuth, J.L., Malen, J.A., Shao, L., McGaughey, A.J., Narra, S.P. (2024) Limits of dispersoid size and number density in oxide dispersion strengthened alloys fabricated with powder bed fusion-laser beam. *Additive Manufacturing*, **81**, 104022.
25 Hassin, M.J. and Salman, T.A. (2022) Review of Green Synthesis and Anticorrosion Applications for Yttrium Oxide Nanoparticles. *IJDDT*, **12** (04).
26 Sagadevan, S., Podder, J., Das, I. (2016) Hydrothermal synthesis of zirconium oxide nanoparticles and its characterization. *J Mater Sci: Mater Electron*, **27** (6), 5622–5627.
27 Zhang, D., Gökce, B., Barcikowski, S. (2017) Laser Synthesis and Processing of Colloids: Fundamentals and Applications. *Chemical Reviews*, **117** (5), 3990–4103.
28 Husák, R., Hadraba, H., Chlup, Z., Heczko, M., Kruml, T., Puchý, V. (2019) ODS EUROFER Steel Strengthened by Y-(Ce, Hf, La, Sc, and Zr) Complex Oxides. *Metals*, **9** (11), 1148.
29 Zhang, C.H., Kimura, A., Kasada, R., Jang, J., Kishimoto, H., Yang, Y.T. (2011) Characterization of the oxide particles in Al-added high-Cr ODS ferritic steels. *Journal of Nuclear Materials*, **417** (1-3), 221–224.
30 Poudel, B., Nguyen, H.X., Kwon, P., Chung, H. (2023) Selective laser melting of oxide dispersion strengthened MA956 alloy and its surface finishing by magnetic field assisted finishing. *Journal of Manufacturing Processes*, **97**, 220–234.
31 *History and outlook of ODS/NFA ferritic alloys for nuclear applications* (2018).
32 Hilger, I., Boulnat, X., Hoffmann, J., Testani, C., Bergner, F., Carlan, Y. de, Ferraro, F., Ulbricht, A. (2016) Fabrication and characterization of oxide dispersion strengthened (ODS) 14Cr steels consolidated by means of hot isostatic pressing, hot extrusion and spark plasma sintering. *Journal of Nuclear Materials*, **472**, 206–214.

33 Spartacus, G., Malaplate, J., Geuser, F. de, Sornin, D., Gangloff, A., Guillou, R., Deschamps, A. (2020) Nano-oxide precipitation kinetics during the consolidation process of a ferritic oxide dispersion strengthened steel. *Scripta Materialia*, **188**, 10–15.
34 Singh, R., Prakash, U., Kumar, D., Laha, K. (2022) Nano oxide particles in 18Cr oxide dispersion strengthened (ODS) steels with high yttria contents. *Materials Characterization*, **189**, 111936.
35 Unocic, K.A., Pint, B.A., Hoelzer, D.T. (2016) Advanced TEM characterization of oxide nanoparticles in ODS Fe–12Cr–5Al alloys. *J Mater Sci*, **51** (20), 9190–9206.
36 Ganesan, D., Sellamuthu, P., Prashanth, K.G. (2020) Vacuum Hot Pressing of Oxide Dispersion Strengthened Ferritic Stainless Steels: Effect of Al Addition on the Microstructure and Properties. *JMMP*, **4** (3), 93.
37 Zhang, Z. and Pantleon, W. (2017) Oxide nanoparticles in an Al-alloyed oxide dispersion strengthened steel: crystallographic structure and interface with ferrite matrix. *Philosophical Magazine*, **97** (21), 1824–1846.
38 Deng, L., Luo, J., Tu, J., Hu, R., Guo, N., Zeng, W., Wang, C., He, P., Zhang, Y. (2023) Achieving excellent mechanical properties of ODS steel by Y2O3 addition. *Materials Science and Engineering: A*, **872**, 145008.
39 Arzt, E. (1998) Size effects in materials due to microstructural and dimensional constraints: a comparative review. *Acta Materialia*, **46** (16), 5611–5626.
40 Gottstein, G. (2011], 2010) *Physical foundations of materials science*, Springer, Berlin, London.
41 Jue, J., Gu, D., Chang, K., Dai, D. (2017) Microstructure evolution and mechanical properties of Al-Al2O3 composites fabricated by selective laser melting. *Powder Technology*, **310**, 80–91.
42 Vasquez, E., Giroux, P.-F., Lomello, F., Chniouel, A., Maskrot, H., Schuster, F., Castany, P. (2019) Elaboration of oxide dispersion strengthened Fe-14Cr stainless steel by selective laser melting. *Journal of Materials Processing Technology*, **267**, 403–413.
43 J. Tatlock, G., Dawson, K., Boegelein, T., Moustoukas, K., R. Jones, A. (2016) High resolution microstructural studies of the evolution of nano-scale, yttrium-rich oxides in ODS steels subjected to ball milling, selective laser melting or friction stir welding. *Materials Today: Proceedings*, **3** (9), 3086–3093.
44 Susila, P., Sturm, D., Heilmaier, M., Murty, B.S., Subramanya Sarma, V. (2011) Effect of yttria particle size on the microstructure and compression creep properties of nanostructured oxide dispersion strengthened ferritic (Fe–12Cr–2W–0.5Y2O3) alloy. *Materials Science and Engineering: A*, **528** (13-14), 4579–4584.
45 Ramar, A., Baluc, N., Schäublin, R. (2009) On the lattice coherency of oxide particles dispersed in EUROFER97. *Journal of Nuclear Materials*, **386-388**, 515–519.
46 Wu, Y., Ciston, J., Kräemer, S., Bailey, N., Odette, G.R., Hosemann, P. (2016) The crystal structure, orientation relationships and interfaces of the nanoscale oxides in nanostructured ferritic alloys. *Acta Materialia*, **111**, 108–115.
47 Hsiung, L.L. (2010) *HRTEM study of oxide nanoparticles in Fe-16Cr ODS ferritic steel developed for fusion energy*.
48 Zhai, W., Zhou, W., Nai, S.M.L. (2024) Effect of Interface Wettability on Additively Manufactured Metal Matrix Composites: A Case Study of 316L-Y2O3 Oxide Dispersion-Strengthened Steel. *Metals*, **14** (2), 170.
49 Dou, P., Jiang, S., Qiu, L., Kimura, A. (2020) Effects of contents of Al, Zr and Ti on oxide particles in Fe–15Cr–2W–0.35Y2O3 ODS steels. *Journal of Nuclear Materials*, **531**, 152025.

50 Jia, H., Zhang, R., Long, D., Sun, Y., Zhou, Z. (2022) Effect of zirconium content on mechanical properties of ODS FeCrAl alloy. *Materials Science and Engineering: A*, **839**, 142824.
51 Kumar, P.K., Sai, N.V., Krishna, A.G. (2018) Effect of Y2O3 and ZrO2 on the microstructure and mechanical properties of nano-ODS 21Cr-9Mn-6Ni steels. *Mater. Tehnol.*, **52** (4), 493–497.
52 *Korean J. Met. Mater.*, **55** (12) (2017) Effect of Heat-Treatment on the Elevated Temperature Compression and Compressive Creep Properties of Fe-14Cr Ferritic Oxide Dispersion Strengthened (ODS) Steel.
53 Zhu, W., Zhang, Z., Long, D., Li, H., Yu, L. (2023) Creep Deformation Behavior, Microstructure Evolution, and Damage Mechanism of Super304H ODS Steel. *Metals*, **13** (6), 1106.
54 Zhao, Q., Yu, L., Liu, Y., Li, H. (2015) Morphology and structure evolution of Y2O3 nanoparticles in ODS steel powders during mechanical alloying and annealing. *Advanced Powder Technology*, **26** (6), 1578–1582.
55 Zhai, W., Zhou, W., Nai, S.M.L., Wei, J. (2020) Characterization of nanoparticle mixed 316 L powder for additive manufacturing. *Journal of Materials Science & Technology*, **47**, 162–168.
56 Rösler, J. and Arzt, E. (1990) A new model-based creep equation for dispersion strengthened materials. *Acta Metallurgica et Materialia*, **38** (4), 671–683.
57 Imagawa, Y., Hashidate, R., Miyazawa, T., Onizawa, T., Ohtsuka, S., Yano, Y., Tanno, T., Kaito, T., Ohnuma, M., Mitsuhara, M., Toyama, T. (2024) Creep deformation and rupture behavior of 9Cr-ODS steel cladding tube at high temperatures from 700°C to 1000°C. *Journal of Nuclear Science and Technology*, **61** (6), 762–777.
58 Singh, R., Prakash, U., Kumar, D., Laha, K. (2023) Development of creep resistant high yttria 18Cr ferritic ODS steel through hot powder forging route. *Journal of Nuclear Materials*, **584**, 154566.
59 Ren, J., Yu, L., Liu, C., Ma, Z., Li, H., Wang, Z., Liu, Y., Wang, H. (2022) Creep properties, microstructural evolution, and fracture mechanism of an Al added high Cr ODS steel during creep deformation at 600 °C. *Journal of Nuclear Materials*, **558**, 153376.
60 Srolovitz, D., Petkovic-Luton, R., Luton, M.J. (1982) On dislocation-incoherent particle interactions at high temperatures. *Scripta Metallurgica*, **16** (12), 1401–1406.
61 Vasquez, E., Giroux, P.-F., Lomello, F., Nussbaum, M., Maskrot, H., Schuster, F., Castany, P. (2020) Effect of powder characteristics on production of oxide dispersion strengthened Fe 14Cr steel by laser powder bed fusion. *Powder Technology*, **360**, 998–1005.
62 Dobson, S.D. and Starr, T.L. (2021) Powder characterization and part density for powder bed fusion of 17-4 PH stainless steel. *RPJ*, **27** (1), 53–58.
63 Haferkamp, L., Haudenschild, L., Spierings, A., Wegener, K., Riener, K., Ziegelmeier, S., Leichtfried, G.J. (2021) The Influence of Particle Shape, Powder Flowability, and Powder Layer Density on Part Density in Laser Powder Bed Fusion. *Metals*, **11** (3), 418.
64 Kiani, P., Scipioni Bertoli, U., Dupuy, A.D., Ma, K., Schoenung, J.M. (2020) A Statistical Analysis of Powder Flowability in Metal Additive Manufacturing. *Adv Eng Mater*, **22** (10).
65 Park, C.W., Choi, W.J., Byun, J., Do Kim, Y. (2022) Effect of high-energy ball milling on the microstructure and mechanical properties of Ni-based ODS alloys fabricated using gas-atomized powder. *J Mater Sci*, **57** (38), 18195–18204.
66 Dai, L., Liu, Y., Dong, Z. (2012) Size and structure evolution of yttria in ODS ferritic alloy powder during mechanical milling and subsequent annealing. *Powder Technology*, **217**, 281–287.
67 Eiselt, C.C., Schendzielorz, H., Seubert, A., Hary, B., Carlan, Y. de, Diano, P., Perrin, B., Cedat, D. (2016) ODS-materials for high temperature applications in advanced nuclear systems. *Nuclear Materials and Energy*, **9**, 22–28.

68 Shi, W., Yu, L., Liu, C., Ma, Z., Li, H., Wang, Z., Liu, Y., Gao, Q., Wang, H. (2022) Evolution of Y2O3 precipitates in ODS-316 L steel during reactive-inspired ball-milling and spark plasma sintering processes. *Powder Technology*, **398**, 117072.
69 He, P., Hoffmann, J., Möslang, A. (2018) Effect of milling time and annealing temperature on nanoparticles evolution for 13.5% Cr ODS ferritic steel powders by joint application of XAFS and TEM. *Journal of Nuclear Materials*, **501**, 381–387.
70 Bor, A., Jargalsaikhan, B., Uranchimeg, K., Lee, J., Choi, H. (2021) Particle morphology control of metal powder with various experimental conditions using ball milling. *Powder Technology*, **394**, 181–190.
71 Cintins, A., Anspoks, A., Purans, J., Kuzmin, A., Timoshenko, J., Vladimirov, P., Gräning, T., Hoffmann, J. (2015) ODS steel raw material local structure analysis using X-ray absorption spectroscopy. *IOP Conf. Ser.: Mater. Sci. Eng.*, **77**, 12029.
72 SALUR, E. (2022) Structural evolution of mechanically alloyed ODS steel powders during ball milling and subsequent annealing treatment. *International Advanced Researches and Engineering Journal*, **6** (2), 80–89.
73 Dharmalingam, G., Prasad, M.A., Salunkhe, S. (2021) Optimization of milling speed and time in mechanical alloying of ferritic ODS steel through taguchi technique. *Int. J. Simul. Multidisci. Des. Optim.*, **12**, 25.
74 Xu, H., Lu, Z., Jia, C., Feng, D., Liu, C. (2016) Influence of Mechanical Alloying Time on Morphology and Properties of 15Cr-ODS Steel Powders. *High Temperature Materials and Processes*, **35** (5), 473–477.
75 Zhou, Y., Yin, S., Jiang, Y., Zhou, Q., Peng, J., Yan, Y. (2022) Wire and arc additive manufacturing fabrication of ODS-RAFM steels and preliminary evaluation on microstructures and mechanical properties. *Journal of Nuclear Materials*, **572**, 154068.
76 Mansur, L.K. (1994) Theory and experimental background on dimensional changes in irradiated alloys. *Journal of Nuclear Materials*, **216**, 97–123.
77 Ghayoor, M., Lee, K., He, Y., Chang, C., Paul, B.K., Pasebani, S. (2020) Selective laser melting of austenitic oxide dispersion strengthened steel: Processing, microstructural evolution and strengthening mechanisms. *Materials Science and Engineering: A*, **788**, 139532.
78 Rakhmonov, J.U., Kenel, C., Luca, A. de, Leinenbach, C., Dunand, D.C. (2022) Effect of Y2O3 dispersoids on microstructure and creep properties of Hastelloy X processed by laser powder-bed fusion. *Additive Manufacturing Letters*, **3**, 100069.
79 Luu, D.N., Zhou, W., Nai, S.M.L. (2022) Influence of nano-Y2O3 addition on the mechanical properties of selective laser melted Inconel 718. *Materials Science and Engineering: A*, **845**, 143233.
80 Kenel, C., Luca, A. de, Joglekar, S.S., Leinenbach, C., Dunand, D.C. (2021) Evolution of Y2O3 dispersoids during laser powder bed fusion of oxide dispersion strengthened Ni-Cr-Al-Ti γ/γ′ superalloy. *Additive Manufacturing*, **47**, 102224.
81 Luca, A. de, Kenel, C., Pado, J., Joglekar, S.S., Dunand, D.C., Leinenbach, C. (2021) Thermal stability and influence of Y2O3 dispersoids on the heat treatment response of an additively manufactured ODS Ni–Cr–Al–Ti γ/γ′ superalloy. *Journal of Materials Research and Technology*, **15**, 2883–2898.
82 Shi, Y., Lu, Z., Xu, H., Xie, R., Ren, Y., Yang, G. (2019) Microstructure characterization and mechanical properties of laser additive manufactured oxide dispersion strengthened Fe-9Cr alloy. *Journal of Alloys and Compounds*, **791**, 121–133.

83 Wang, Y. and Shi, J. (2019) Engulfment and distribution of second-phase nanoparticle during dendrite solidification of an Al–Si binary alloy: a simulation study. *Appl. Phys. A*, **125** (6).
84 Stefanescu, D.M., Shangguan, D., den Brincken, P. von (1991) Particle Engulfment and Pushing by Solidifying Interfaces (PEPSI). *MSF*, **77**, 25–42.
85 Chen, X.-H. and Yan, H. (2016) Solid–liquid interface dynamics during solidification of Al 7075–Al2O3np based metal matrix composites. *Materials & Design*, **94**, 148–158.
86 Wang, J., Zhou, X., Li, J., Zhu, J., Zhang, M. (2022) A comparative study of Cu–15Ni–8Sn alloy prepared by L-DED and L-PBF: Microstructure and properties. *Materials Science and Engineering: A*, **840**, 142934.
87 Wilms, M.B., Pirch, N., Gökce, B. (2023) Manufacturing oxide-dispersion-strengthened steels using the advanced directed energy deposition process of high-speed laser cladding. *Prog Addit Manuf*, **8** (2), 159–167.
88 Doñate-Buendia, C., Kürnsteiner, P., Stern, F., Wilms, M.B., Streubel, R., Kusoglu, I.M., Tenkamp, J., Bruder, E., Pirch, N., Barcikowski, S., Durst, K., Schleifenbaum, J.H., Walther, F., Gault, B., Gökce, B. (2021) Microstructure formation and mechanical properties of ODS steels built by laser additive manufacturing of nanoparticle coated iron-chromium powders. *Acta Materialia*, **206**, 116566.
89 Hou, W., Stubbs, T., DeBeer-Schmitt, L., Chang, Y.-T., Charpagne, M.-A., Smith, T.M., Huang, A., Cordero, Z.C. (2024) Dissolution zone model of the oxide structure in additively manufactured dispersion-strengthened alloys. *Additive Manufacturing*, **96**, 104554.
90 Xu, S., Zhou, Z., Jia, H., Yao, Z. (2019) Microstructure Characterization and Mechanical Properties of Al Alloyed 9Cr ODS Steels with Different Al Contents. *steel research int.*, **90** (7).
91 Huang, Y., Fleming, T.G., Clark, S.J., Marussi, S., Fezzaa, K., Thiyagalingam, J., Leung, C.L.A., Lee, P.D. (2022) Keyhole fluctuation and pore formation mechanisms during laser powder bed fusion additive manufacturing. *Nat Commun*, **13** (1), 1170.
92 Guo, Q., Zhao, C., Qu, M., Xiong, L., Hojjatzadeh, S.M.H., Escano, L.I., Parab, N.D., Fezzaa, K., Sun, T., Chen, L. (2020) In-situ full-field mapping of melt flow dynamics in laser metal additive manufacturing. *Additive Manufacturing*, **31**, 100939.
93 Williams, C.A., Unifantowicz, P., Baluc, N., Smith, G.D., Marquis, E.A. (2013) The formation and evolution of oxide particles in oxide-dispersion-strengthened ferritic steels during processing. *Acta Materialia*, **61** (6), 2219–2235.
94 Zhang, J., Li, Y., Bao, F., Rui, X., Duan, Z., Yan, W., Shi, Q., Wang, W., Shan, Y., Yang, K. (2021) Study on the formation mechanism of Y-Ti-O oxides during mechanical milling and annealing treatment. *Advanced Powder Technology*, **32** (2), 582–590.
95 Koncz, P., Horváth, Á., Balázsi, K., Şahin, F.Ç., Göller, G., Onüralp, Y., Balázsi, C. (2012) Correlation between Milling Parameters, Structural and Mechanical Properties of Nanostructured Austenitic Y_2O_3 Strengthened Steels. *MSF*, **729**, 409–414.
96 Reichenberger, S., Marzun, G., Muhler, M., Barcikowski, S. (2019) Perspective of Surfactant-Free Colloidal Nanoparticles in Heterogeneous Catalysis. *ChemCatChem*, **11** (18), 4489–4518.
97 Feld, A., Weimer, A., Kornowski, A., Winckelmans, N., Merkl, J.-P., Kloust, H., Zierold, R., Schmidtke, C., Schotten, T., Riedner, M., Bals, S., Weller, H. (2019) Chemistry of Shape-Controlled Iron Oxide Nanocrystal Formation. *ACS nano*, **13** (1), 152–162.
98 Dankesreiter, S. (2015) Synthese und Charakterisierung photokatalytisch aktiver PbBiO2Br-Nanopartikel. Universität Regensburg.

99 Müller, A., Karthikeyan, C.S., Neukam, M., Willert-Porada, M. (2006) Mikrowellen-unterstützte Herstellung von TiO2 und Gd2O3 Nanopartikeln und deren Charakterisierung. *Mat.-wiss. u. Werkstofftech.*, **37** (4), 298–300.
100 Olliges-Stadler, I. (2011) Chemical formation and crystallization mechanisms of tungsten oxide nanoparticles in organic solvents. ETH Zurich.
101 Thanh, N.T.K., Maclean, N., Mahiddine, S. (2014) Mechanisms of nucleation and growth of nanoparticles in solution. *Chemical Reviews*, **114** (15), 7610–7630.
102 Parashar, M., Shukla, V.K., Singh, R. (2020) Metal oxides nanoparticles via sol–gel method: a review on synthesis, characterization and applications. *J Mater Sci: Mater Electron*, **31** (5), 3729–3749.
103 Kumari, S., Raturi, S., Kulshrestha, S., Chauhan, K., Dhingra, S., András, K., Thu, K., Khargotra, R., Singh, T. (2023) A comprehensive review on various techniques used for synthesizing nanoparticles. *Journal of Materials Research and Technology*, **27**, 1739–1763.
104 Sathishkumar, M., Sneha, K., Yun, Y.-S. (2010) Immobilization of silver nanoparticles synthesized using Curcuma longa tuber powder and extract on cotton cloth for bactericidal activity. *Bioresource technology*, **101** (20), 7958–7965.
105 Kim, M., Osone, S., Kim, T., Higashi, H., Seto, T. (2017) Synthesis of Nanoparticles by Laser Ablation: A Review. *KONA*, **34** (0), 80–90.
106 Sasaki, T., Shimizu, Y., Koshizaki, N. (2006) Preparation of metal oxide-based nanomaterials using nanosecond pulsed laser ablation in liquids. *Journal of Photochemistry and Photobiology A: Chemistry*, **182** (3), 335–341.
107 Streubel, R., Barcikowski, S., Gökce, B. (2016) Continuous multigram nanoparticle synthesis by high-power, high-repetition-rate ultrafast laser ablation in liquids. *Optics letters*, **41** (7), 1486–1489.
108 Scattergood, R.O. and Bacon, D.J. (1975) The Orowan mechanism in anisotropic crystals. *Philosophical Magazine*, **31** (1), 179–198.

Appendices

Appendix A: Study I

Appendix B: Study II

Appendix C: Study III

Appendix D: CV/ Lebenslauf

Appendix A: Study I

Goßling, M., Rittinghaus, S.-K., Bharech, S., Yang, Y., Wilms, M.B., Becker, L., Weber, S., Xu, B.-X., Gökce, B. (2024)

Towards enhancing ODS composites in laser powder bed fusion: Investigating the incorporation of laser-generated zirconia nanoparticles in a model iron–chromium alloy.

Journal of Materials Research, 39 (5), 774–788

DOI: 10.1557/s43578-023-01267-4

Journal of MATERIALS RESEARCH

Article
DOI:10.1557/s43578-023-01267-4

Towards enhancing ODS composites in laser powder bed fusion: Investigating the incorporation of laser-generated zirconia nanoparticles in a model iron–chromium alloy

Mareen Goßling[1], Silja-Katharina Rittinghaus[1], Somnath Bharech[2], Yangyiwei Yang[2], Markus B. Wilms[1], Louis Becker[3], Sebastian Weber[3], Bai-Xiang Xu[2], Bilal Gökce[1,a)]

[1] *Chair of Materials Science and Additive Manufacturing, School of Mechanical Engineering and Safety Engineering, University of Wuppertal, Gaußstraße 20, 42119 Wuppertal, Germany*
[2] *Mechanics of Functional Materials Division, Institute of Materials Science, Technische Universität Darmstadt, Otto-Berndt-Strasse 3, 64287 Darmstadt, Germany*
[3] *Chair of Materials Technology, Institute for Materials, Ruhr-Universität Bochum, Universitätsstraße 150, 44801 Bochum, Germany*
[a)] Address all correspondence to this author. e-mail: goekce@uni-wuppertal.de

Received: 14 September 2023; accepted: 7 December 2023

Oxide dispersion-strengthened (ODS) steel is a sought-after composite material known for its high demand in high-temperature and corrosive environments. Achieving the desired ODS steel properties requires specific conditions for the size and nanoparticles (NP) distribution in the printed part. Laser ablation in liquid (LAL) enables precise NP size adjustment. At the same time, the dynamic melt pool solidification in the Laser Powder Bed Fusion (PBF-LB/M) process complements this by creating favorable conditions for successful ODS processing. In this study, ZrO_2 NP with a small and narrow particle size distribution (d_{50} = 3.8 nm; d_{90} = 10 nm) is produced by LAL. Dielectrophoretic deposition achieves the homogeneous, deformation-free coating of the binary Fe20Cr (wt.-%) matrix powder with NP. PBF-LB/M printed parts out of the oxide-additivated powder exhibit a crack-free structure and a density of up to 98%. Expectedly, the metal matrix grain sizes and room temperature microhardness (~ 220 HV) are not affected by NP addition. NP tracing by 2D simulation indicates a homogeneous NP distribution and less than 10% NP to be agglomerated in the solidified part. Thus, a promising perspective for a complete laser-based process chain for generating and processing ODS alloys is outlined.

Introduction

In recent years, the additive manufacturing (AM) commercialization has experienced substantial growth. However, a significant challenge is the limited range of available materials [1]. This limitation poses a considerable obstacle to the widespread adoption and advancement of this technique [2]. Materials being investigated for AM encompass a broad range, including high-entropy alloys, shape memory alloys, and intermetallic compounds. Additionally, there is a growing emphasis on researching magnetic alloys and novel metal composite structures [3]. Composite materials often involve nanomaterials inclusion, such as carbides [4] or ceramic nanoparticles (NP), in a metal matrix. The NP use aims to positively influence the matrix and achieve tailored material properties that suit specific applications. One well-known composite material example of high technical relevance are oxide-dispersion-strengthened (ODS) alloys, which ensure exceptional strength in high-temperature regimes, particularly regarding creep properties [5, 6]. Therefore, these alloys are of high interest in modern combustion engines [7]. Moreover, due to their resistance to high-energy neutron irradiation, ODS alloys are also candidates for use in novel nuclear and future fusion power plants [8]. The conventional ODS materials production by powder metallurgical processing requires multiple subsequent processing steps, while AM allows for direct near-net-shape production. By avoiding repetitive sintering, heat treatment procedures, and mechanical finishing

processes, the manufacturing route efficiency can thus be significantly increased, which makes ODS AM a promising field of research [9]. The unique AM process characteristics, including high solidification rates [10], allow rapid melt pool solidification and highly dynamic melt pool flow [11], preventing NP agglomeration in the melt pool and enabling homogenous ceramic NP dispersion, therefore meeting the requirements for the advanced ODS materials manufacturing [12].

ODS materials are characterized by nano-scaled oxide particles homogeneously dispersed in a metallic matrix and are considered a particular type of metal-ceramic composite material [6, 13, 14]. The typical matrix-incoherent particles can only be bypassed by dislocation rather than penetrated, leading to retardation of dislocation movements with extra energy provided, which ultimately leads to material strengthening. This effect is known as the Orowan mechanism [15].

Nevertheless, AM of ODS materials faces challenges, especially regarding suitable powder material production. ODS materials, which were already successfully manufactured by AM of a variety of matrix and oxide materials [16], typically consist of powder composites produced by mechanical alloying [16–18]. However, the reduced flowability of mechanically alloyed powder material due to mechanical deformation [9, 19] results in smaller process windows [20], which makes the development of powder composites with high sphericity necessary, typically exhibiting improved flowabilities [21, 22]. In this case, macro powder additivation by dielectrophoretic deposition can remedy the situation by maintaining the sphericity of the gas-atomized base powder and retaining the flowability. The successful dielectrophoretic deposition demonstration of the iron-chromium-based ferritic steel PM2000 and Y_2O_3 NP is further elaborated in [23].

Regarding the NP strengthening effect in ODS material, the theoretical optimum NP size in the bulk material is expected to be below 10 nm [24] to fully exploit the benefits of rapid solidification and low agglomeration and obtain maximum creep resistance. Typically, commercially available NP range in size from 20 nm up to micro-sized particles and are produced by liquid-based processing (sol–gel or chemical reduction), milling, or from the vapor phase (physical/chemical vapor deposition and flame synthesis), which ends in chemically contaminated NP-surfaces. The two main disadvantages of chemically produced NP—namely, broad size distribution and ligand-contaminated surfaces—can be circumvented by producing NP using Laser Ablation in Liquid (LAL). LAL advantages include the environment friendly, ligand-free production of a comprehensive materials variety such as noble metals [25], alloys [26], or oxides [27, 28]. Thus, this process offers favorable prerequisites for NP generation and a wide range of composites production to be processed with powder-based AM. Additionally, LAL can be scaled up to industrial quantities [29] and thus allows for the further development of tailored, application-driven material solutions that will further push AM commercialization.

Combining the advantages of laser-based ceramic additivated powder production and processing to a composite, this study considers the entire process chain using the ODS steel example. To assess the benefits and limitations of the laser-based process chain, it is essential to understand the effects of the spherical LAL-generated NP and the deformation-free additivation process. This understanding should be compared with conventionally produced NP and mechanical alloying to examine the resulting NP size and distribution in ODS composites. These properties play a crucial role in influencing high-temperature mechanical properties. Due to the NP inaccessibility during the processing and the impossibility of performing in-situ measurements of their movement, the combination of simulations with the experimental characterization of the NP-additivated powder and the manufactured ODS steel provides the best approach to understanding and controlling the PBF-LB/M processing of ODS steels. Therefore, NP tracing simulations based on a kinematic model considering NP-NP and flow-NP interactions are performed to study the migration and additivated NP distribution. The information of the melt flow under-prescribed processing parameters (majorly the laser power, scan speed, and laser spot size) is provided by heat-melt-microstructure (HMM)-coupled non-isothermal phase-field simulation [30]. To study the influence of NP on material strengthening by the Orowan mechanism, other strengthening mechanisms, such as, e.g., grain refinement or solid-solution strengthening, must be prevented; otherwise, interfering influences will prevent accurate investigation. Thus, this study uses a Fe20Cr model material to avoid undesirable reactions between nanoparticles and the elements present in the melt. LAL-generated zirconia (ZrO_2) NP are used for this binary steel oxide reinforcement system. ZrO_2 NP are frequently used to reinforce steels [31], titanium [32], aluminum [33], and copper [34] alloys. Compared to typically used yttrium-based NP for ODS alloys with a melting temperature of 2425 °C, ZrO_2 has a higher melting temperature of 2715 °C which ends up in higher thermal NP stability [35], which is beneficial for manufacturing processes with high peak intensities like PBF-LB/M.

Additionally, compared to Y_2O_3, ZrO_2 is expected to have a lower agglomeration behavior due to the lower attractive forces between the particles, characterized by a relatively low Hamaker constant. This expectation leads to the anticipation of less agglomeration in the melt pool during the PBF-LB/M process and, consequently, more minor NP accumulations in the solid. According to the theory of Arzt and Rößler [36], this contributes to an increased temperature resistance of the material as the NP distribution is decisive for the stress required to activate dislocation passing. The numerical simulation compares the agglomeration behavior of the different NP materials.

ZrO_2 is already successfully produced with LAL. To emphasize the possibility of economically scaling the whole process for industrial use, in the production of NP in LAL, a readily commercially available zirconium (Zr700) target material is used for producing NP with LAL. By ablation in water, the material reacts to form zirconia and can be used for additivated metal powder production of the ODS material.

In this study, the complete laser-based ODS steel processing route is investigated using the Fe20Cr-0.8 ZrO_2 (wt.-%) example consisting of LAL-NP generation, oxide-additivated metal powder production, and forming a composite by PBF-LB/M. The products of the different fabrication steps are studied and correlated with the resulting consolidated PBF-LB/M material properties. Special attention is paid to the NP size and distribution evolution during the single stages. The experimental data interpretation is supported with results from numerical simulation to gain deeper insight into the influencing physical and processing parameters and conditions.

Results

Size distribution and chemical composition of nanoparticles generated by LAL from Zr700

In Fig. 1(a), the size distribution of the LAL-generated zirconia NP is presented. The polydispersity index (PDI) can be used to evaluate the monodispersity of the NP. It is calculated as a variance ($\sigma 2$) divided by xc2 values from the log-normal fit function. The higher the variances and the standard deviation are, the broader the size distribution. For a homogenous NP distribution, monodispersity, a small PDI < 10%, is desirable [37]. With a PDI of 9.13%, the size distribution shown in Fig. 1(a) can be categorized as monodisperse. In Fig. 1(b), the results of EDS measurements on exemplary NP are presented. In the top left BFTEM image, homogeneously distributed small NP (< 15 nm, marked with white arrow) as well as a few larger NP (> 15 nm, marked with black arrow) are indicated. The NP tend to agglomerate in the liquid, which can also be seen from the superimposed BFTEM image of the NP (Fig. 1(a)). In Fig. 1(b), TEM-EDS maps of Zr, Hf, and O with a corresponding BFTEM image are depicted. The examined elements are homogeneously distributed in both small (< 15 nm) and large (> 15 nm) NP. The overall measured elemental distribution is noted, respectively, emphasizing a mostly stoichiometric composition of ZrO_2 with residual elements accounting for approx. 1.1 at.-%.

In Fig. 1(c), TEM-EDS line scans of individual NP are depicted. The upper line scan in Fig. 1(c) shows one of the few larger NP with a diameter of approximately 60 nm to illustrate the composition of the NP in detail. In the lower line scan in Fig. 1(c), a comparatively small particle of around 5 nm diameter is shown, which is in the range of the average NP diameter. Both scans show an increase of the elements Zr and O over the particle radius. In addition to these expected elements, the Hf content also increases over the radius of the particles. The base signal noise of Hf is anticipated as this element is already in the metal target before ablation. Hf oxides may have also formed, but no individual Hf oxide particles could be detected. As Hf and Zr have similar chemical properties and similar lattice structures, it is reasonable to expect that Hf replaces a few Zr lattice positions, forming a complex oxide compound $(Zr, Hf)O_2$. The signals for Fe and Cr can be categorized as background noise, proving that the dielectrophoretic deposition process has no impact on the chemical composition of the NP.

The diffractogram of the zirconia NP is shown in Fig. 2 and reveals the characteristic reflections of ZrO_2. In addition, various other reflections can be detected, suggesting the presence of pure Zr and orthorhombic and monoclinic HfO_2. However, the characteristic reflections of all phases are difficult to distinguish, as can be seen from the double and triple occupation of

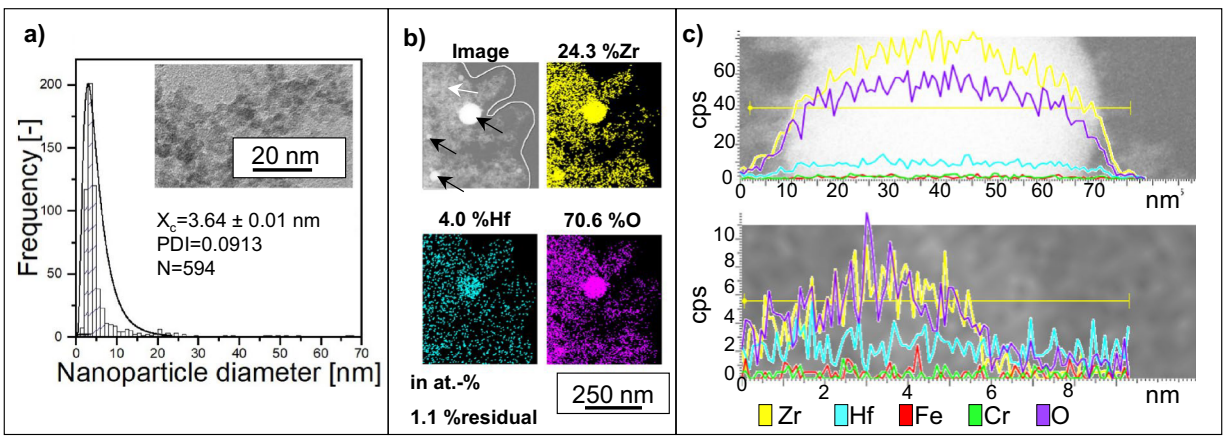

Figure 1: NP generated by LAL of a Zr700 target (a) Feret diameter size distribution derived by BFTEM image processing; (b) TEM-EDS mapping of generated NP including respective TEM-EDS measurement results; (c) TEM-EDS line scan results of individual NP with diameters of 60 nm and 5 nm.

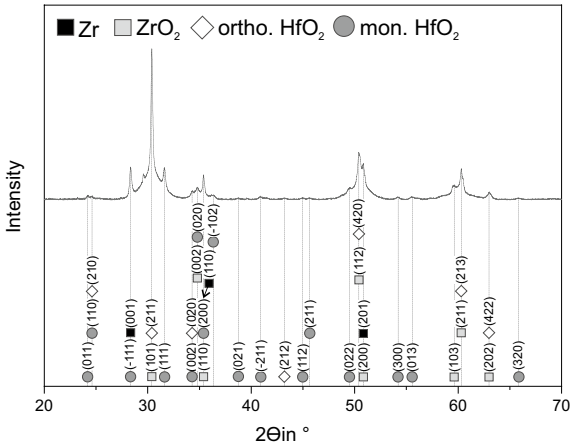

Figure 2: Diffraction pattern of zirconia NP indicating the characteristic reflections of Zr, ZrO_2, orthorhombic HfO_2 and monoclinic HfO_2.

individual reflections in Fig. 2. Considering the results already shown from the chemical analysis utilizing XRF and EDS, it can be stated that besides tetragonal ZrO_2, mainly monoclinic HfO_2 is present. This conclusion is based on the reflections of the monoclinic HfO_2 as in the example of the (111)-reflection at approx. 31.6° 2Θ also partly exists without interference with reflections of the ZrO_2 or the other phases. Admittedly, this also applies in part, to reflexes of orthorhombic HfO_2 (e.g., (212)-reflection at approx. 43.6° 2Θ). However, these show a much lower intensity compared to monoclinic HfO_2. The occurrence of pure Zr, demonstrated by the EDS and XRF measurements, cannot be clearly detected using XRD due to the aforementioned phase interferences.

Chemical and morphological characteristics of oxide-additivated metal powder

In Fig. 3, SEM images of Fe20Cr particles (a, b) and Fe20Cr additivated with ZrO_2 NP (c, e, f) with different magnifications presented. Compared to the base Fe20Cr metal powder (Fig. 3(a, b)), NP are visible on the surface of the oxide-additivated metal powder depicted in Fig. 3(c, e, f), resulting in a rough surface texture. On the surface of both powder materials, satellites can be seen (indicated with orange arrows). Small agglomerates of NP are visible on the microparticles (white arrows in Fig. 3(e)). Only small areas appear not covered by NP (green arrow). All in all, the NP are homogeneously dispersed on the surface of the microparticles, and the size of the agglomerates is small compared to mechanically alloyed ODS powder, e.g., 20–200 nm used in [38] or 30–50 nm used in [39], and the additivated powder has maintained a spherical shape. The spherical shape originating from the deformation-free dielectrophoretic additivation process makes the material particularly suitable for AM. Figure 3(d) shows the EDS measurements of the oxide-additivated metal powder. The intensity of the signal for the elements Fe and Cr is constant, thereby homogeneously distributed over the powder particle.

Since no increased concentration of Fe and Cr is detected on the particle edges, it can be hypothesized that these elements' signals originate from the initial Fe20Cr powder matrix. Due to the measurement method, a stronger signal is detected from elements close to the surface, i.e., Zr and O, indicated by the orange arrows in Fig. 3(d). In addition to that, the uniform distribution of O and Zr detection suggests that the matrix particle surface is evenly wetted with NP. The areas for detecting Zr and O overlap, making it evident that ZrO_2 coats the surface. The regions with increased Zr and O content are indicated with white arrows. Thus, it can be concluded that a more significant agglomeration of ZrO_2 can be found at these locations. XRF measurements revealed a global composition of the oxide-additivated metal powder of 78.20Fe-20.80Cr-0.79Zr-0.12Si (wt.-%) thus, considering the statistical error of 0.26% for Zr, being a good agreement with the nominal composition.

Microstructure and hardness of bulk material built by PBF-LB/M

Figure 4 displays the microstructure of Fe20Cr and Fe20Cr-0.8 ZrO_2 (wt.-%) ODS composite material consolidated through PBF-LB/M, observed in cross-sections. A notable difference is observed between the two materials, with the ODS material exhibiting a higher presence of pores (f) and consequently a lower density of 98.3% compared to the 99.7% density of raw Fe20Cr steel (a). Figure 4(b) and (g) show cross-sections of the 45 s specimens etched with Nital (10%). The microstructure is characterized by small (approx. 10 to 100 µm width) elongated (up to several 100 µm length) epitaxially grown grains. The grain size of the ODS material is similar compared to the base metal matrix, leading to the conclusion that the NP do not affect grain growth, which could be reasoned by the low wettability of ZrO_2 in Fe–Cr melt, inhibiting heterogeneous nucleation and thus otherwise expected grain refinement. The composite hardness at room temperature with 217.4 ± 11 HV0.1 is similar to the hardness of base Fe20Cr with 219.2 ± 9 HV0.1, indicating similar mechanical room temperature properties. These analytical results fit well with grain size since solid-solution strengthening and grain boundary strengthening are the dominant reinforcing effects in soft matrices at room temperature. At high temperatures, the hindering of dislocation movement by particle hardening in ODS alloys is expected to result in pronounced strengthening, e.g., observed in [18] for a similar system. In Fig. 4(c)

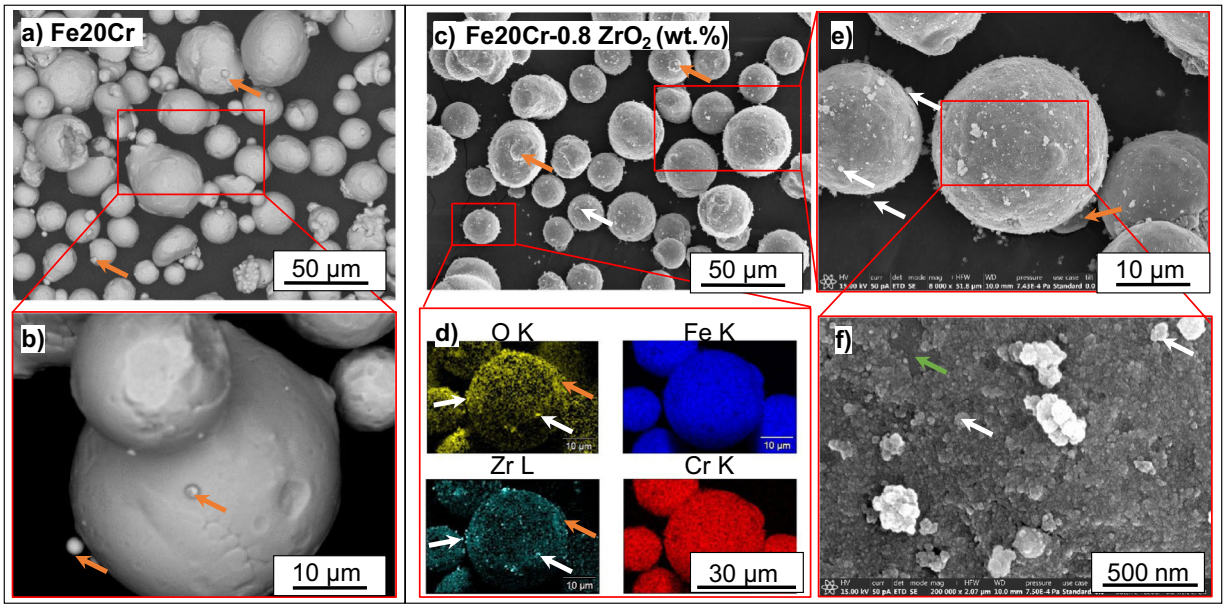

Figure 3: SEM images of Fe20Cr-powder (a, b) and oxide-additivated metal powder (c, e, f) in different magnification, (d) SEM–EDS mapping of elements from Fe20Cr-0.8 ZrO_2 (wt.-%) powder.

and (d), SEM images of the Fe20Cr without NP are depicted in different magnifications. A yellow dashed line indicates a grain boundary, and etching defects (whitish areas) are visible in (d). A comparable extract was selected in image (i) from Fig. 4 for the Fe20Cr-ODS sample. In comparison, the whitish areas of the composite (i) are smaller and more finely distributed than in (d).

Localized EDS surface scans of different microstructural features provide information on the local elemental composition, as summarized in Table 1.

The results show negligible traces of Zr in the Fe20Cr alloy without NP (spectrum 1 and 2 in Table 1 and Fig. 4(d)), but a significant amount in the entire composite sample (spectrum 3 and 4 in Table 1 and Fig. 4(i)). Similarly, a higher Zr proportion is detected in spectrum 4 compared to spectrum 3, suggesting the ZrO_2 accumulation in the bright region. From this, it can be concluded that some white areas in Fig. 4(h) represent NP agglomerates. However, no clear visible distinction between etched microstructural features and Zr-enriched, presumably NP areas is possible. From EDS measurements depicted in Fig. 4(j), in addition to a weak, likely background noise signal for Zr (also visible in Fig. 4(e)), apparently randomly distributed Zr clusters can be observed. These clusters indicate a Zr accumulation and thus ZrO_2 NP agglomerates, especially regarding dimensions of up to several 10 nm. Individual NP are very small, and considering the given noise signal, EDS mappings cannot determine their size and exact distribution. However, no specific concentration at, e.g., grain boundaries is visible, which supports the assumption of a homogeneous distribution that requires to be confirmed in future investigations.

Simulation of the influence of NP type and size on agglomeration during PBF-LB/M

As explained in "Numerical Study of nanoparticle evolution in PBF-LB/M melt pool" section, simulations are conducted with a smaller number of NP compared to the experiment to compensate for the substantial computational power requirements. To investigate the influence of NP size on agglomeration properties, the varying size of NP additivated to the Fe20Cr powder is simulated and then correspondingly traced during the process simulations. Figure 5(b) shows the comparison of size distributions of NP produced by LAL (cf. Fig. 1(a) for experimental values), NP traced during PBF-LB/M simulations and the size distribution of the simulation in Yang et al. [40]. In the case of smaller NP, a large number of NP are traced to represent the same NP mass fraction θ in the oxide-additivated metal powder, thereby requiring denser decoration on the single metal particles; in other words, the interparticle distance is significantly reduced.

The agglomeration behavior strongly depends on the (van der Waals) attraction force and the particle distances. The van der Waals attraction force between the two most widely used nano-additives for manufacturing ODS alloys Y_2O_3 and ZrO_2 as a function of the surface distance between two NP is analytically compared and depicted in Fig. 5(a). The attractive force increases as the interparticle distance between two NP decreases, leading to a higher agglomeration for closely packed small NP. As expected by physical principles, the tendency of NP to agglomerate decreases with increasing size. From Fig. 5(a), it can also be concluded that ZrO_2 NP undergo lower attractive force, suggesting lower agglomeration than Y_2O_3. Figure 5(c)

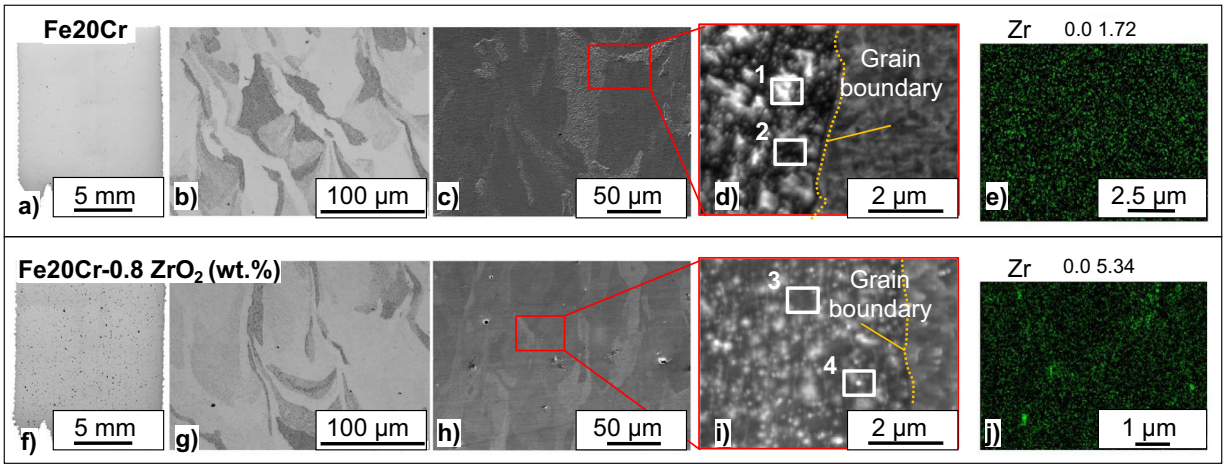

Figure 4: Cross sections PBF-LB/M parts of Fe20Cr (a–e) and Fe20Cr-0.8 ZrO_2 (f–j), in etched state; SEM images Fe20Cr (b–d) and Fe20Cr-0.8 ZrO_2 (g–i), and respective EDS mappings of Zr (e, j).

TABLE 1: Chemical composition of bulk material from EDS examinations of PBF-LB/M consolidated Fe20Cr and Fe20Cr-0.8 ZrO_2 (wt.-%).

Alloy	Fe20Cr		Fe20Cr-0.8 ZrO_2 (wt.-%)	
Area in Fig. 4	1 (wt.-%)	2 (wt.-%)	3 (wt.-%)	4 (wt.-%)
O	0.97	0.71	0.82	1.29
Si	0.06	0.05	0.07	0.08
Cr	21.13	21.37	21.12	20.93
Fe	77.76	77.83	77.79	76.82
Zr	0.07	0.04	0.2	0.88

presents the destination statistics of migrating NP and the corresponding classification of agglomerated/non-agglomerated Y_2O_3 and ZrO_2 NP traced during the PBF-LB/M process simulations. The results exhibit that ~ 33% of Y_2O_3 NP participate in agglomeration, while only ~ 26% of ZrO_2 NP are agglomerated. Moreover, in both cases, most NP are enclosed in grains, but the ZrO_2 NP agglomeration in grains is 7.3% lower than the Y_2O_3 NP, suggesting better ZrO_2 NP dispersion in the base metal matrix.

The blue size distribution [Fig. 5(b)] is used to study the ZrO_2 NP evolution during PBF-LB/M. Due to their size and concentration, the NP are closely packed in a 2D simulation domain; they undergo high attractive forces [compare Fig. 5(a)].

The particles tend to accelerate towards each other, potentially on a collision path. However, there is the potential 'overshooting' NP where the NP migrates with high velocities due to an instantaneous strong attractive acceleration, thereby missing the supposed collision at the next step. This discrepancy may be caused by the time discretization scheme employed in this work, in which the melt flow dynamics and nanoparticle kinematics share the same time increment and discretization form (i.e., backward Euler form). It should be discussed in the upcoming works. To avoid this the overshooting NP discrepancy, the on-site magnitude of melt flow is taken as the velocity threshold for the NP. When an NP crosses that threshold velocity, it is effectively captured by the melt. It assumes the velocity from the melt for that particular time step, which is physically interpreted as the NP should not overtake the melt flow in the sense of a complete inelastic collision. As a result, the explosive drifting of NP while being suspended in the melt is prevented mainly, as shown in Fig. 5(c).

NP evolution during processing is graphically displayed in Fig. 5(d), presenting the trajectories and the final position of the NP dispersed in the PBF-LB/M-processed Fe20Cr alloy matrix. It is essential to state that the markers represent only the center locations and not the size of the NP. In contrast, the color of the markers is used to describe the final positions of the NP in the microstructure.

In Fig. 5(d), three scopes are chosen and magnified to visualize the NP and their potential agglomerations. On the microscale, one might prematurely suspect the presence of heavy agglomeration in these regions. However, upon finer inspection, one can quickly discover the presence of locally enriched isolated NP and some small NP agglomerates.

A statistical analysis of the agglomeration of NP is presented in Fig. 5(e), wherein the fraction of NP agglomerated is further classified based on their cluster size. Most of the NP remain non-agglomerated; only 7.9% of NP are observed to have participated in agglomeration. The agglomerate clusters formed by the NP are relatively small, with 85.8% of the agglomerated NP forming a 2-particle cluster. The relatively bigger clusters are rare, suggesting that the size distribution of nano inclusions in the processed part would not differ drastically from the size of NP additivated to the alloy powder particles.

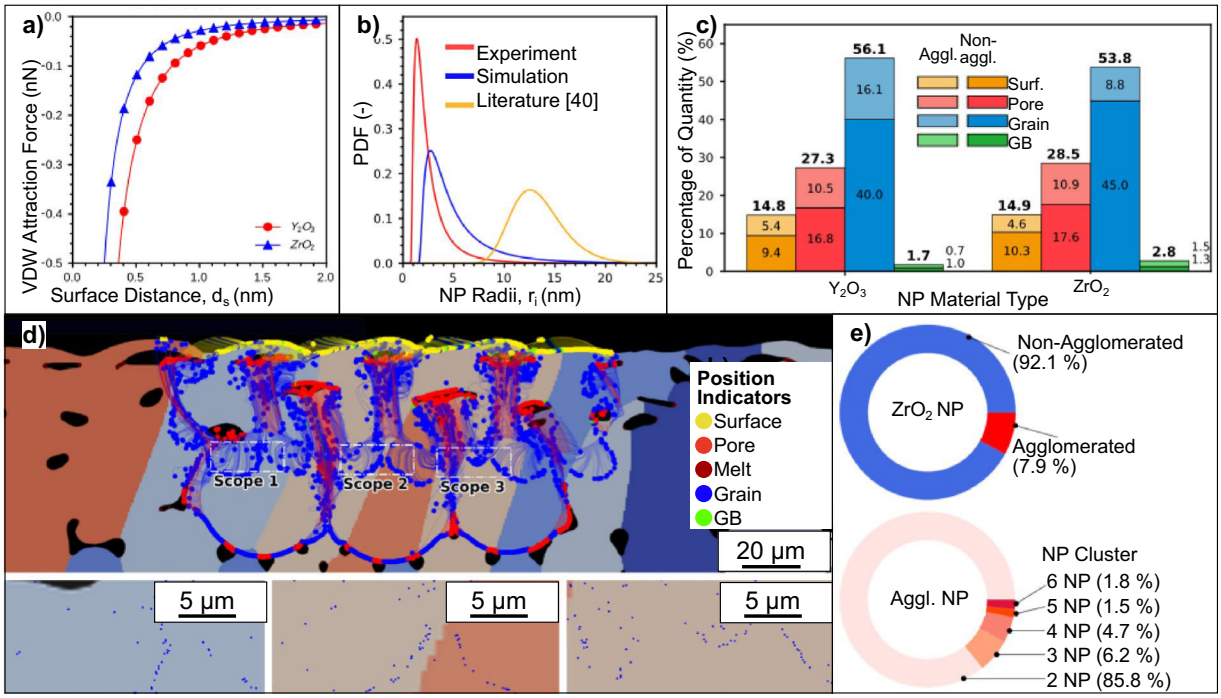

Figure 5: Simulation results of NP tracing in PBF-LB/M; (a) Attractive interaction force with varying interparticle surface distance for different NP dispersed in the melt. Surface distance, d_S represents the distance between the surfaces of two NP with $d_S = d_C - (r_i + r_j)$, where d_C is the distance between the centres of two NP and r_i and r_j are their respective radii; (b) experimentally and numerically determined ZrO_2 NP size distribution; (c) comparison of agglomeration statistics in PBF-LB/M solids with different NP for identical process conditions, NP size distribution and NP load; (d) simulated NP distribution in PBF-LB/M solids; (e) classification of the traced ZrO_2 NP as agglomerated or non-agglomerated NP after a single scan of PBF-LB/M and further analysis of the agglomerated NP in the formation of various cluster sizes.

Discussion and conclusions

In this study, a laser-assisted process chain for the fabrication of composites in AM is demonstrated, focusing on the feasibility of the process for the fabrication of oxide-dispersion-reinforced (ODS) composites. Laser ablation in liquid is used to produce oxide NP with an average diameter of 7 nm ($d_{50} = 3.8$ nm, $d_{90} = 10$ nm). The homogeneous distribution of NP on Fe20Cr macroparticles is achieved by dielectrophoretic deposition, and the resulting oxide-additivated metal powder is processed by PBF-LB/M, producing composite samples with a density higher than 97%. At room temperature, the hardness of the material remained unchanged around 220 HV0.1, and the microstructure of the metal matrix is not significantly affected by the NP. These results demonstrate the basic feasibility of the laser-assisted process chain for producing advanced composites for AM. Moreover, the applied simulation approach provided the first insights into the agglomeration behavior of ZrO_2 NP by 2D tracing.

Comparative simulation of the agglomeration behavior of Y_2O_3 and ZrO_2 NP based on their material properties supports the selection of NP for ODS, as ZrO_2 NP exhibited better dispersion compared to Y_2O_3, which is considered desirable for improving high-temperature mechanical properties in ODS steels. The findings from the numerical study suggest that the size and dispersion of resulting nano agglomerates in ODS steels manufactured by PBF-LB/M can be engineered to achieve desirable mechanical properties by controlling the size of the initial NP introduced in the oxide-additivated metal powder. The simulation of the degree of agglomeration dependent on the NP sizes suggests that the fraction of NP participating in agglomeration increases for decreasing NP size. However, as revealed in the statistical analysis of the agglomerated NP, most agglomerates are small and formed by only 2–4 NP, thus still expected to be magnitudes smaller and consequently more effective compared to conventionally produced NP with typical sizes around 50 nm in diameter. An exciting subsequent research question is whether an optimized balance between initial NP size and agglomeration rates and types can be achieved. Simulations with further NP sizes can help to answer this question and motivate NP production of specific sizes with LAL.

One advantageous characteristic of the oxide nanoparticle-additivated metal powder production by dielectrophoretic deposition is that the powder particles' sphericity, size distribution, and shape are unaffected. The powder remains flowable and, thus, ensures the requirements for good processability. While dielectrophoretic deposition yielded the expected and desired results, demonstrating low agglomeration and homogeneous NP distribution on the metal powder surface, the comparatively

low density of the resulting Fe20Cr-0.8 ZrO_2 (wt.-%) samples requires further attention. Spherical pores can be observed in the microstructure of the ODS material, indicating evaporation of the residual moisture. The detected difference in the humidity of both materials supports this assumption (0.08 wt.-% H_2O for Fe20Cr vs. 0.12 wt.-% H_2O for the additivated powder). Other reasons for different behavior in the PBF-LB/M process could be different absorption properties for laser radiation of the ODS material, which can lead to altered energy input. In contrast, laser parameters remain the same, thus defects in the microstructure. An extended parameter study and re-drying of the additivated powder is believed to lead to higher densities prospectively. Once a higher relative density of PBF-LB/M processed parts is achieved, mechanical characterization, including tensile and creep tests at elevated temperatures, is to be performed to investigate the strengthening effect of the NP and deformation behavior of the composite under load.

Regarding grain size and morphology of printed specimen, the microstructure formation is not visibly affected by NP addition; it can be concluded that no additional effect, such as grain refinement or significant changes in solidification conditions, is caused. This leads to the hypothesis that any strengthening determined in upcoming investigations can be attributed to particle hardening due to the Orowan mechanism. However, it has to be considered that grain refinement by oxide NP is possibly dependent on the alloy system [41]. Hence, this finding for the investigated model alloy is not generally valid. Additionally, chemical reactions between the matrix and NP need to be considered for the transfer to more complex systems [30]. Although further studies are needed to understand all underlying mechanisms fully, these results contribute to understanding the behavior of NP in PBF-LB/M-processed materials and emphasize the importance of consideration of the entire system.

It can be hypothesized that oxide NP would hinder dislocations even at room temperature, leading to an increase in hardness. Contrary to this expectation, however, the hardness of our ODS alloy does not increase significantly compared to the pure iron-chromium alloy. This behavior is consistent with observations described in [30, 42]. In [30], despite constant hardness at room temperature, a higher compressive strength was demonstrated at elevated temperatures, which is attributed to the Orowan mechanism. Similarly, [42] found a significant increase in tensile strength at high temperatures, which was not apparent when comparing the hardness of the pure alloy with the corresponding ODS alloy at room temperature. A possible explanation for the consistent hardness at room temperature could be the pronounced agglomeration of the nanoparticles within our printed components. In Fig. 4, spectrum 4 indicates a nanoparticle size of approximately 150 nm. With an initial size of approx. 7 nm, before consolidation via PBF-LB/M, this agglomeration size may reduce the number density and distribution degree of the nanoparticles, resulting in a significantly bigger interparticle distances. These larger interparticle distances substantially reduce the efficiency of hindering the dislocation mobility by the Orowan mechanism, making it difficult to detect an Orowan-induced increase by Vickers hardness measurements. Furthermore, it could be hypothesized that the very soft Fe–Cr matrix causes a displacement of the NPs along the dislocation planes upon penetration of the Vickers indenter, leading to comparable hardness to the non-reinforced counterpart. In summary, despite the lack of a detectable increase in hardness induced by the Orowan mechanism at room temperature, the literature [30, 42] supports the expectation of strain hardening by the Orowan mechanism at elevated temperatures. However, tensile characterization of our printed ODS material is underway to confirm our findings.

An existing challenge is the seamless alignment of experiment and simulation, which requires large analytical efforts and computational capacities. It has to be mentioned that the PBF-LB/M process parameters used in the phase-field simulations differ from the ones used in the experiment. The laser beam power used in the simulation (160 W) is comparable to the experimental parameter (150 W), but a larger beam spot (160 µm diameter) is used for simulation. Simulating a smaller beam spot would mean a higher intensity of laser power and, therefore, increased melt flow drifts, potentially resulting in the formation of spatters [43]. These would affect the resultant microstructure and NP dispersion throughout the metal matrix.

Further research is required to discover the influence of laser beam spot size on the microstructure evolution and the NP distribution by experiment and simulation. As the NP mass fraction utilized in the numerical study is meager (0.005 wt.-%) compared to the experiment (0.8 wt.-%), the influence on the melt properties and, subsequently, the final microstructure was considered to be negligible and, therefore, neglected. However, this consideration aligns with the experimental observation, where even a considerably high amount of NP showed no apparent influence on the matrix microstructure. Despite the computational constraints posing limitations like insufficiently small time increment, inadequate size distribution, and number of NP in the simulation domain, the kinematic model could trace ZrO_2 NP throughout a single scan of PBF-LB/M processing. Thus, the NP evolution and resultant agglomeration behavior could be revealed. Although this is not statistically validated regarding cluster sizes, it still appears to be of the same magnitude order as indicated by EDS element maps. The distribution on the smaller nanoscale is prospective to be verified by TEM investigation of the built Fe20Cr + ZrO_2 part.

To gain additional understanding of the mechanical properties of the resulting alloy, it would be beneficial to investigate the reinforcement of the composite with various NP loadings. By varying the loading of oxide NP, the mechanical properties of

the composite could be tailored for specific applications. Studies are revealing the influence of NP on melt dynamics [44], solidification behaviour [45], porosity [46], and melt properties such as viscosity, surface tension and thermal conductivity [47–49]. The NP load used in the numerical study presented here is significantly lower, and therefore, the exclusion of potential effects on the melting behaviour and its properties is justified. However, higher NP loads and their influence on melt properties and the resultant microstructure will be investigated in future works.

In summary, the present study provides a promising starting point for further research on laser-assisted composite manufacturing for additive manufacturing. Based on the findings and methods presented here, it may be possible to develop and economically produce new and advanced composites with a wide range of customizable properties, enabling applications in highly demanding environments.

Materials and methods

Materials

Zirconia NP were fabricated from Zr700 material (VDM Metals, Altona, Germany) using LAL in deionized (DI) water. The composition of the target material is characterized by X-ray fluorescence (XRF) and revealed a composition of 98.70 wt.-% Zr, 1.23 wt.-% Hf, and a residual of 0.07 wt.-%.

Micrometer-sized metal powder with the nominal composition Fe20Cr (wt.-%) was used as the base material for the oxide-additivated metal powder production. The initial particle size distribution given by the manufacturer (Rosswag GmbH, Pfinztal, Germany) was 15 µm to 45 µm (d_{10} = 19 µm, d_{50} = 29 µm, d_{90} = 43 µm). The chemical composition of the Fe20Cr (wt.-%) powder was verified by XRF, confirming a chemical composition of 78.7Fe-21.2Cr (wt.-%).

Analytical methods

LAL-generated NP were investigated by transmission electron microscopy (TEM) using a JEM-2200FS (JOEL GmbH, Freising, Germany). The size distribution was obtained via image analysis of the bright field TEM in the software ImageJ (Version 1.53 T). X-ray diffraction (XRD) of the zirconia NP was carried out to characterize the phase composition of the bulk NP material. A D8 Advanced system (Bruker Corporation) was used for the investigation, working according to the Bragg–Brentano setup and emitting CuKα radiation (wavelength: 1.5406 Å). The diffractogram was recorded in the 20–70° 2Θ using a step size of 0.01° and an acquisition time of 5 s per step. The obtained diffractogram was analyzed using the software DIFFRAC.EVA V3.0. To load the NP into the sample holder of the measuring device, they were dried and glued to a C-pad in advance so that the entire surface of the C-pad was covered with NP. A diffractogram was also recorded from the C-pad without NP addition to ensure that the carbon pad did not significantly influence the measurement. It turned out that the C-pad shows reflection, but these are mainly lost in the noise of the NP measurement due to their low intensity.

The moisture of powder samples before AM was determined by the loss-on-drying method, using an HX204 gravimetric moisture analyzer (Mettler Toledo GmbH, Gießen, Germany) to ensure sufficient flowability before consolidation via AM. The solid bulk composite samples, fabricated using PBF-LB/M from the oxide-additivated metal powder, were subjected to a 45-s etching with Nital (10%) solution. Subsequently, the NP distribution and size within the matrix were analyzed by EDS mapping using a scanning electron microscope (Apreo S LoVac, Thermo Fisher Scientific). The chemical composition of the PBF-LB/M samples was determined by EDS area scans using an MIRA3 instrument (TESCAN GmbH) equipped with a Nordlys nano detector (Oxford) and Aztec software (Oxford). Measurements were performed using an accelerating voltage of 20 kV and a working distance of 15 mm. The metal matrix Fe20Cr and the oxide-additivated metal powder Fe20Cr-0.8 ZrO_2 (wt.-%) were analyzed by XRF using an S8 Tiger (Bruker Corporation) equipped with a rhodium X-ray tube, a beryllium window, and a power of 4 kW. Each sample with 3 g of powder material was measured and analyzed via a quantitative method (Quant-Express) developed for the Bruker device, which uses the Kα lines to determine each element's weight percentage (wt.-%). Microstructural characterization was performed by light optical microscopy (LOM) (Leica, DM-2700) of metallographically prepared cross-sections. Densities were determined using the software ImageJ (Version 1.53 T). The PBF-LB/M samples were evaluated for microhardness using the Vickers HV 0.1 test method with 10 s indentation time and a Carat 930 (ATM Qness GmbH, Mammelzen, Germany). Five measurements were randomly distributed over the 10 mm cube for each specimen.

Nanoparticle synthesis by LAL

In LAL, a laser beam is focused on a target that is surrounded by liquid. The ablated material is converted into a plasma phase with laser pulse irradiation. [50, 51] By reaching the ablation threshold, NP are removed from the surface of the target and carried away by the flowing liquid. In addition to the surrounding liquid and the laser parameters, it is primarily the target material that influences the chemical composition of the NP produced. In [52], the possibilities to influence the LAL-generated NP and their desired composition by variating the composition and element distribution of the target are described. Here, the setup to ablate zirconium material in water includes a YLPN-0.5–1 × 5–80 ytterbium pulsed fiber laser in pulsed mode (IPG Laser GmbH, Burbach, Germany) with a maximum power of 80 W, a wavelength of 1064 nm and a pulse duration of 1 ns.

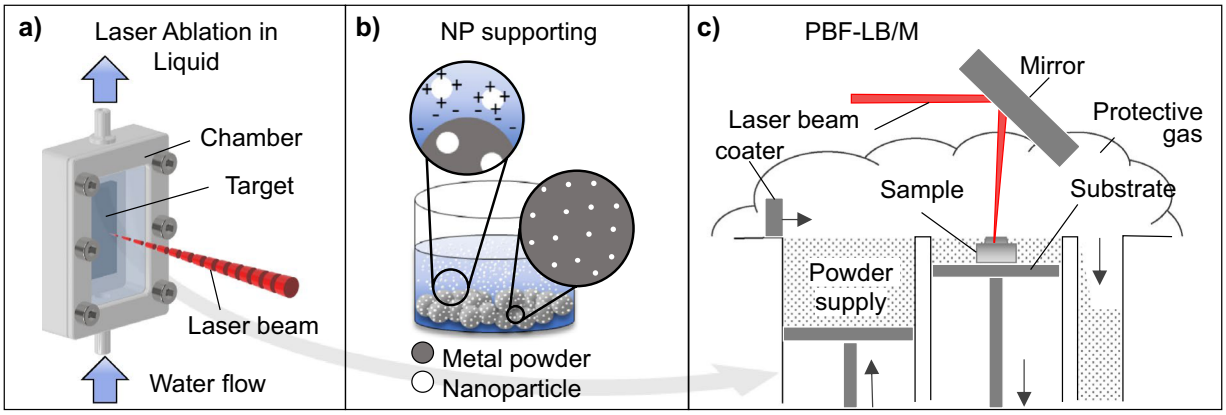

Figure 6: Schemes of (a) LAL process, (b) NP supporting, and (c) PBF-LB/M process scheme.

Focusing the laser beam is achieved by an f-theta lens with a focal distance of $f = 167$ mm. The experimental setup scheme is shown in Fig. 6(a). A spiral scanning pattern is applied for ablation, enabled using a galvanometric scanning unit MINISCAN III-14 (Raylase GmbH, Weßling, Germany). A peristaltic pump LabV3 (Baoding Shenchen Precision Pump Co. Ltd, Baoding China) with a constant flow rate of 150 ml/min is used to create a continuous flow of DI water during the ablation. The NP used as additives for the oxide-additivated metal powder are synthesized with a laser power (P_L) of 61 W and a repetition rate (R_{Rep}) of 3 MHz. The laser fluence (F) of 6.5 J/cm2 is calculated with a beam spot diameter (D_{beam}) of 40 µm.

Nanoparticle supporting on metallic powder by dielectrophoretic deposition

The dielectrophoretic deposition created an oxide-additivated metal powder from ZrO_2-NP and Fe20Cr metallic micro-sized powder. Water was used as the solvent along with the Fe20Cr metal powder and the laser-generated ZrO_2 nanoparticles in a ratio of 0.8 wt.-% ZrO_2. The mixture was stirred in a rotary evaporator at 70 rpm and 60 °C under a 200 mbar atmosphere. The moisture content of the metal base material was 0.08 wt.-% H_2O, remaining moisture of the oxide-additivated metal powder after deposition was 0.12 wt.-% H_2O. The scheme of the process is shown in Fig. 6(b).

Additive manufacturing by PBF-LB/M

The Fe20Cr metal powder (as reference) and the Fe20Cr-0.8 ZrO_2 (wt.-%) powder were processed by PBF-LB/M using an Aconity MINI laboratory printer (Aconity3D GmbH, Herzogenrath, Germany). Figure 6(c) shows the process scheme where a laser beam is scanned over the surface of the powder bed placed onto the substrate plate, selectively melting and fusing the powder particles. The build platform is subsequently lowered by the defined layer height distance, and a new layer of powder material is applied by the coater, followed by laser exposure. This process is repeated until the cubic structures are entirely built. In this study, the powder materials are processed by a laser with a focal spot with a diameter of 48 µm and a wavelength of 1064 nm on a 316L substrate base plate. All samples were built with an energy density (VED) of 78 J/mm^3 calculated from 150 W laser power (P_L), 800 mm/s scan velocity (v_s), and 80 µm hatch distance (D_s) with a 30 µm layer height (Δz_s) in an Argon atmosphere.

Numerical Study of nanoparticle evolution in PBF-LB/M melt pool

The numerical study for NP migration during the PBF-LB/M process is based on the schematic shown in Fig. 7, where in HMM—coupled phase-field model transfers transient microstructure along with other relevant data into the NP kinematic model to estimate the migration of NP in the melt. A non-isothermal phase-field model was employed to simulate the microstructure evolution of Fe20Cr alloy manufactured by the PBF-LB/M process, details of which are sufficiently expressed in our previous works [40, 53].

However, to ensure thoroughness, the essentials of the model employed are summarized in this section. A stable PBF-LB/M process was considered without significant vaporization and resulting phenomena such as keyholing and spattering. The simulation provided coupled evolution of polycrystalline microstructure, melt flow dynamics, and heat transfer on the mesoscale (0.1–100 µm). The possible impact of NP on these mesoscale effects was tentatively omitted in this study, as the size of NP is negligible compared to the characteristic scale of the mentioned physical processes. A conserved order parameter (OP), ρ was used to represent the substance field (when $\rho = 1$) and the atmosphere/pore region (when $\rho = 0$). Another non-conserved OP, ϕ was used to represent the solid substance, and as the existence of solid and liquid phases were constrained within only the substance region, $(\rho - \phi)$ describes the liquid substance. A series of non-conserved

OP $\{\eta_\alpha\}$ were employed to represent the grain orientations. To limit the polycrystalline orientations inside the solid substance, a polycrystal constraint $(1-\phi)+\sum_\alpha \eta_\alpha = 1$ was implemented. The following equations governed the heat-melt coupled microstructure evolution (1, 2, 3, 4, 5, 6):

$$\nabla \cdot \mathbf{u} = 0 \tag{1}$$

$$\frac{\mathrm{D}\boldsymbol{u}}{\mathrm{D}t} = -\nabla p + \frac{1}{\mathrm{Re}}\nabla^2 \boldsymbol{u} + \frac{1}{\mathrm{Fr}^2}\widehat{\mathbf{g}} \tag{2}$$

$$\frac{\mathrm{D}T}{\mathrm{D}t} + \frac{1}{\mathrm{Ste}_\phi}\frac{\mathrm{D}\phi}{\mathrm{D}t} = \nabla \cdot \left(\frac{1}{\mathrm{Pe}_T}\nabla T\right) + q_\mathrm{v} \tag{3}$$

$$\frac{\mathrm{D}\rho}{\mathrm{D}t} = \nabla \cdot \left(\frac{1}{\mathrm{Pe}_\rho}\nabla \frac{\delta \mathcal{F}}{\delta \rho}\right) \tag{4}$$

$$\frac{\mathrm{D}\phi}{\mathrm{D}t} = -\frac{1}{\mathrm{Ac}_\phi}\frac{\delta \mathcal{F}}{\delta \phi} \tag{5}$$

$$\frac{\mathrm{D}\eta_\alpha}{\mathrm{D}t} = -\frac{1}{\mathrm{Ac}_\eta}\frac{\delta \mathcal{F}}{\delta \eta_\alpha} \tag{6}$$

with $q_\mathbf{v} = \Phi_{\mathrm{ss}}\beta P_L p_x p_z$

Equations (1) and (2) govern the melt flow with the flow velocity $\boldsymbol{u}$. Equation (3) regulates the thermal evolution of the transient microstructure coupled with the melt flow dynamics. Equation (4) is based on the conservation of mass. Equations (5) and (6) take the form of Allen–Cahn equations to govern the melting-solidification phenomenon and the grain growth dynamics during the PBF-LB/M process. The explicit formulation for free energy $\mathcal{F}$, detailed parameterization of the dimensionless numbers, namely the Reynolds number (Re), the Froude number (Fr), the Stefan number (Ste), the Péclet numbers (Pe), and the Allen–Cahn numbers (Ac) and the fitting of relevant model parameters are well reported in our previous work [40]. The thermal effect from the laser beam was modeled as an internal heat source term $q_\mathbf{v}$, moving with the scan velocity $\boldsymbol{v}$. Φ_{ss} is the interpolation function used for the substance field, β is the attenuation coefficient, p_x and p_z dictate the power distribution in scanning (x) and build (z) directions, respectively.

Transient thermal-microstructure, simulated for a single scan of PBF-LB/M processing with $P_\mathrm{L} = 160$ W, $v_\mathrm{s} = 800$ mm/s and a laser beam diameter of 160 µm was employed to investigate the NP migration during the PBF-LB/M process [40]. Two different NP compositions, i.e., Y_2O_3 and ZrO_2, were compared to justify the selection of NP in experiment. Table 2 shows the Hamaker constants and densities of these NP compositions. $A_{\mathrm{p:v}}$ and $A_{\mathrm{p:m}}$ are Hamaker constants that quantify the interactions between NP dispersed in the vacuum and the melt, respectively. Equation (7) shows the kinematic model for estimating the NP migration

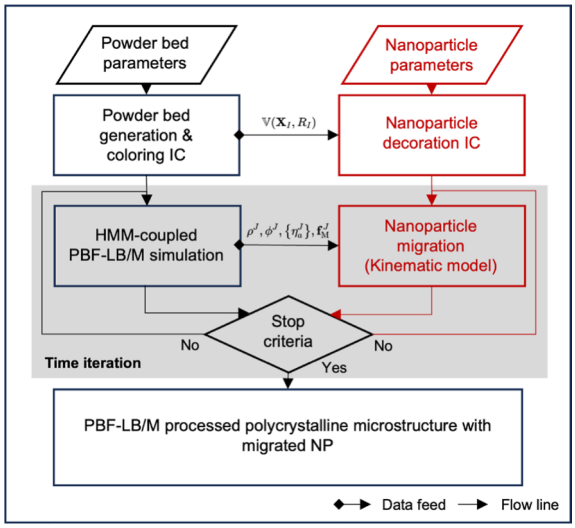

Figure 7: Schematic for the simulation workflow, including Heat-Melt-Microstructure (HMM)—coupled phase-field simulation for PBF-LB/M process and subsequent NP kinematic model with data received from the phase-field simulation, to estimate the NP migration. The workflow is based on our previous work from Yang et al. [40].

during the PBF-LB/M process. The model considered force balance on the dispersed rigid NP (labeled as i) with density ϱ_i, radii r_i, and the translation velocity v_i in the melt. Force density due to melt flow driven, (f_M) was calculated and imported from the phase-field simulations. Furthermore, the influence of gravity (ϱ_ig) and van der Waals interaction force density between NP (f_A) was also considered. f_A depends on $A_{\mathrm{p:m}}$, the distance between the centers of NP (d_C) and their corresponding radii (r_i, r_j). Notably, the influence of electrostatic interaction between NP was excluded due to the strong screening effect of background-free electrons in the melt [54, 55].

$$\varrho_i \frac{\mathrm{d}\mathbf{v}_i}{\mathrm{d}t} = \varrho_i \mathbf{g} + \mathbf{f}_\mathrm{M} + \mathbf{f}_\mathrm{A} \tag{7}$$

with, $\boldsymbol{f}_\mathrm{M} = \varrho_\mathrm{m}\left(\frac{\mathrm{D}\mathbf{u}}{\mathrm{D}t}\Big|_{\boldsymbol{x}_i} - \frac{1}{\mathrm{Fr}^2}\widehat{\mathbf{g}}\right)$,

and $\boldsymbol{f}_\mathrm{A} = -\frac{32A_{\mathrm{p:m}}d_\mathrm{C}(r_i r_j)^3}{3V_i\left[d_\mathrm{C}^4 - 2d_\mathrm{C}^2\left(r_i^2+r_j^2\right)+\left(r_i^2-r_j^2\right)^2\right]^2}\frac{\mathbf{x}_i-\mathbf{x}_j}{d_\mathrm{C}}$

Considering the additivation of NP on surfaces of the powder particles in a 3D simulation, the number of NP to be additivated and traced during the processing simulation would be derived from the mass fraction of the NP, θ as shown in Eq. (8), where ϱ_m and ϱ_i are the densities of powder material and NP, respectively. $\mathrm{R_I}$ and $\mathrm{r_i}$ represent their corresponding radii. However, in the case of a 2D scenario, the number of NP to be traced is given by Eq. (9).

$$N_p^{3D} = \frac{\theta \varrho_\mathrm{m} R_I^3}{\varrho_\mathrm{i} r_i^3}, \tag{8}$$

TABLE 2: Density and Hamaker constants for interactions between NP in a vacuum ($A_{p:v}$) and in the melt ($A_{p:m}$) for Y_2O_3 and ZrO_2.

Material	ϱ (kg m^{-3})	$A_{p:v}$ (10^{-20} J)	$A_{p:m}$ (10^{-20} J)	References
Y_2O_3	5010	14.0	5.43	[40]
ZrO_2	5850	20.0	2.58	[56, 57]

$$N_p^{2D} = \frac{\theta \varrho_m R_I^2}{\varrho_i r_i^2} \tag{9}$$

The number of NP required to be traced in a 2D simulation is one order lower than in the 3D scenario. It is worth noting that the reduced number of NP in 2D tracing may eventually lead to a possible low agglomeration fraction compared to the actual one from experiments. Yet, it can deliver the phenomenological understanding of agglomeration affected by the varying NP properties. The NP trajectories were then calculated numerically by discretizing the kinematic model in the backward differences scheme, wherein the time increment for NP trajectory modification was sourced from the phase-field-based process simulation. Agglomerated NP were identified by employing an adjacency test, where the distance between the NP (d_C) centers is individually compared with the corresponding sum of their radii ($r_i + r_j$). Subsequently, the NP were classified as agglomerated or non-agglomerated.

Adopting the NP size distribution with mean radii 13.4 nm and mass fraction 0.005 wt.-% from the former research [40], seven powder particles are additivated with 930 and 1092 NP to compare the agglomeration statistics between ZrO_2 and Y_2O_3, respectively. Based on the adjacency test, the traced NP are classified as agglomerated or non-agglomerated, as well as their final positions in the microstructure, i.e., grain, grain boundaries, pores, and surface.

To accurately simulate the NP tracing during the PBF-LB/M process in a 2D simulation domain, seven powder particles are required to be additivated by approximately 8.09 million NP with mean radii 1.82 nm, thereby implementing 0.8 wt.- % following the experimental parameters for NP size and mass fraction. However, owing to the constraints posed due to limited computational resources, the actual size distribution and mass fraction of ZrO_2 NP generated from LAL could not be employed, and therefore, 4278 ZrO_2 NP with mean radii 6.25 nm were additivated on the seven powder particles, representing 0.005 wt.-% NP load and simultaneously traced during a single scan of PBF-LB/M.

Acknowledgments

The authors would like to express their sincere gratitude to several individuals who contributed to the successful completion of this study. We want to thank Jonas Hankel for his expertise and assistance with the hardness measurements. We also thank Prof. Matthias Epple for the use of their SEM, Daniel Behrens for his help with experimental tasks, and Dr. I. Murat Kusoglu, who contributed to this study by performing the XRF measurements of the zirconium target, the additivated powder, and the LAL-generated NP powder. Finally, S. Bharech, Y. Yang, and B.-X. Xu greatly appreciate the access to the Lichtenberg II High-Performance Computer (HPC) and the technique support from the HHLR, Technical University of Darmstadt. The computation time on the HPC is granted by the NHR4CES Resource Allocation Board under the project "special00007".

Author contributions

MG: investigation, visualization (lead), writing-original draft preparation (lead). S-KR: writing—review & editing, project administration. SB: investigation, software, writing—original draft preparation (support), visualization (support). YY: writing—review & editing, software. MBW: writing-original draft preparation (support). LB: investigation, writing-original draft preparation (support). SW: resources, writing- reviewing and editing. B-XX: resources, writing- reviewing and editing, funding acquisition. BG: conceptualization, resources, writing- reviewing and editing, project administration, funding acquisition.

Funding

Open Access funding enabled and organized by Projekt DEAL. This study is part of a research project funded by the German Research Foundation (DFG) under Priority Program 2122 "Materials for Additive Manufacturing" (SPP 2122, project number 493889809, GO 2566/13-1 and XU 121/20-1). B. Gökce additionally acknowledges funding from the DFG within the Heisenberg Program, project GO 2566/10-1 (445127149).

Data availability

Data sets generated during the current study are available from the corresponding author on reasonable request.

Declarations

Conflict of interest On behalf of all authors, the corresponding author states that there is no conflict of interest.

Open Access

References

1. S.-K. Rittinghaus, E.A. Jägle, M. Schmid, B. Gökce, New frontiers in materials design for laser additive manufacturing. Materials **15**(17), 6172 (2022)
2. A. Vafadar, F. Guzzomi, A. Rassau, K. Hayward, Advances in metal additive manufacturing: a review of common processes, industrial applications, and current challenges. Appl. Sci. **11**(3), 1213 (2021)
3. J.H. Martin, B.D. Yahata, E.C. Clough, J.A. Mayer, J.M. Hundley, T.A. Schaedler, Additive manufacturing of metal matrix composites via nanofunctionalization. MRS Commun. **8**(2), 297–302 (2018)
4. J. Luo, R. Khattinejad, A. Assari, M. Tayyebi, B. Hamawandi, Microstructure, mechanical and thermal properties of Al/Cu/SiC laminated composites, fabricated by the ARB and CARB processes. Crystals **13**(2), 354 (2023)
5. M. Bartsch, A. Wasilkowska, A. Czyrska-Filemonowicz, U. Messerschmidt, Dislocation dynamics in the oxide dispersion strengthened alloy INCOLOY MA956. Mater. Sci. Eng. A **272**(1), 152–162 (1999)
6. M.C. Brandes, L. Kovarik, M.K. Miller, G.S. Daehn, M.J. Mills, Creep behavior and deformation mechanisms in a nanocluster strengthened ferritic steel. Acta Mater. **60**(4), 1827–1839 (2012)
7. Z. Min, S.N. Parbat, L. Yang, B. Kang, M.K. Chyu, Fabrication and characterization of additive manufactured nickel-based oxide dispersion strengthened coating layer for high-temperature application. J. Eng. Gas Turbine. Power (2018). https://doi.org/10.1115/1.4038351
8. J. Gao, P. Song, Y.-J. Huang, K. Yabuuchi, A. Kimura, K. Sakamoto, S. Yamashita, Effects of neutron irradiation on 12Cr–6Al-ODS steel with electron-beam weld line. J. Nucl. Mater. **524**, 1–8 (2019)
9. J.J. Park, S.M. Hong, E.K. Park, M.K. Lee, C.K. Rhee, Synthesis of Fe based ODS alloys by a very high speed planetary milling process. J. Nucl. Mater. **428**(1–3), 35–39 (2012)
10. P.A. Hooper, Melt pool temperature and cooling rates in laser powder bed fusion. Addit. Manuf. **22**, 548–559 (2018)
11. Q. Guo, C. Zhao, M. Qu, L. Xiong, S.M.H. Hojjatzadeh, L.I. Escano, N.D. Parab, K. Fezzaa, T. Sun, L. Chen, In-situ full-field mapping of melt flow dynamics in laser metal additive manufacturing. Addit. Manuf. **31**, 100939 (2020)
12. W.H. Yu, S.L. Sing, C.K. Chua, C.N. Kuo, X.L. Tian, Particle-reinforced metal matrix nanocomposites fabricated by selective laser melting: a state of the art review. Prog. Mater. Sci. **104**, 330–379 (2019)
13. M. Miller, D. Hoelzer, E. Kenik, K. Russell, Nanometer scale precipitation in ferritic MA/ODS alloy MA957. J. Nucl. Mater. **329–333**, 338–341 (2004)
14. G.R. Odette, N.J. Cunningham, T. Stan, M.E. Alam, Y. de Carlan, Nano-oxide dispersion-strengthened steels, in *Structural alloys for nuclear energy applications*. (Elsevier, Amsterdam, 2019), pp.529–583
15. E. Orowan, Symposium on internal stresses, London (1947)
16. M.B. Wilms, S.-K. Rittinghaus, M. Goßling, B. Gökce, Additive manufacturing of oxide-dispersion strengthened alloys: materials, synthesis and manufacturing. Prog. Mater. Sci. **133**, 101049 (2023)
17. T. Boegelein, E. Louvis, K. Dawson, G.J. Tatlock, A.R. Jones, Characterisation of a complex thin walled structure fabricated by selective laser melting using a ferritic oxide dispersion strengthened steel. Mater Charact **112**, 30–40 (2016)
18. M.B. Wilms, R. Streubel, F. Frömel, A. Weisheit, J. Tenkamp, F. Walther, S. Barcikowski, J.H. Schleifenbaum, B. Gökce, Laser additive manufacturing of oxide dispersion strengthened steels using laser-generated nanoparticle-metal composite powders. Procedia CIRP **74**, 196–200 (2018)
19. C. Suryanarayana, T. Klassen, E. Ivanov, Synthesis of nanocomposites and amorphous alloys by mechanical alloying. J. Mater. Sci. **46**(19), 6301–6315 (2011)
20. E. Vasquez, P.-F. Giroux, F. Lomello, M. Nussbaum, H. Maskrot, F. Schuster, P. Castany, Effect of powder characteristics on production of oxide dispersion strengthened Fe 14Cr steel by laser powder bed fusion. Powder Technol. **360**, 998–1005 (2020)
21. C. Doñate-Buendía, D. Gu, M. Schmidt, S. Barcikowski, A.M. Korsunsky, B. Gökce, On the selection and design of powder materials for laser additive manufacturing. Mater. Des. **204**, 109653 (2021)
22. M.A. Spurek, L. Haferkamp, C. Weiss, A.B. Spierings, J.H. Schleifenbaum, K. Wegener, Influence of the particle size distribution of monomodal 316L powder on its flowability and processability in powder bed fusion. Prog. Addit. Manuf. (2021). https://doi.org/10.1007/s40964-021-00240-z
23. R. Streubel, M.B. Wilms, C. Doñate-Buendía, A. Weisheit, S. Barcikowski, J.H. Schleifenbaum, B. Gökce, Depositing laser-generated nanoparticles on powders for additive manufacturing of oxide dispersed strengthened alloy parts via laser metal deposition. Jpn. J. Appl. Phys. **57**(4), 40310 (2018)
24. E. Arzt, Size effects in materials due to microstructural and dimensional constraints: a comparative review. Acta Mater. **46**(16), 5611–5626 (1998)

25. W.T. Nichols, T. Sasaki, N. Koshizaki, Laser ablation of a platinum target in water. II. Ablation rate and nanoparticle size distributions. J. Appl. Phys. **100**(11), 114912 (2006)
26. S.-H. Tsai, Y.-H. Liu, P.-L. Wu, C.-S. Yeh, Preparation of Au–Ag–Pd trimetallic nanoparticles and their application as catalyst-sElectronic supplementary information (ESI) available: UV-vis spectra and EDX analysis of Au–Ag–Pd colloidal suspensions. J. Mater. Chem. **13**(5), 978–980 (2003)
27. C. Zhu, X. Dong, X. Mei, M. Gao, K. Wang, D. Zhao, General fabrication of metal oxide nanoparticles modified graphene for supercapacitors by laser ablation. Appl. Surf. Sci. **568**, 150978 (2021)
28. T. Sasaki, Y. Shimizu, N. Koshizaki, Preparation of metal oxide-based nanomaterials using nanosecond pulsed laser ablation in liquids. J. Photochem. Photobiol. A **182**(3), 335–341 (2006)
29. R. Streubel, S. Barcikowski, B. Gökce, Continuous multigram nanoparticle synthesis by high-power, high-repetition-rate ultrafast laser ablation in liquids. Opt. Lett. **41**(7), 1486–1489 (2016)
30. C. Doñate-Buendia, P. Kürnsteiner, F. Stern, M.B. Wilms, R. Streubel, I.M. Kusoglu, J. Tenkamp, E. Bruder, N. Pirch, S. Barcikowski, K. Durst, J.H. Schleifenbaum, F. Walther, B. Gault, B. Gökce, Microstructure formation and mechanical properties of ODS steels built by laser additive manufacturing of nanoparticle coated iron-chromium powders. Acta Mater. **206**, 116566 (2021)
31. S. Ahda, A. Sujatno, D. Hairani, N. Shabrina, S. Giat, Bandriyana, Microstructure and oxidation behavior of the oxide dispersion strengthened stainless steel 316l with zirconia dispersion. J. Ind. Tech. Ass. **15**(2), 115 (2021)
32. A. Hattal, K. Mukhtarova, M. Djemai, T. Chauveau, A. Hocini, J.J. Fouchet, B. Bacroix, J. Gubicza, G. Dirras, Effect of hot isostatic pressing on microstructure and mechanical properties of Ti6Al4V-zirconia nanocomposites processed by laser-powder bed fusion. Mater. Des. **214**, 110392 (2022)
33. S. Zhang, Z. Chen, P. Wei, K. Huang, Y. Zou, S. Yao, M. Li, B. Lu, J. Xing, Microstructure and properties of a nano-ZrO2-reinforced AlSi10Mg matrix composite prepared by selective laser melting. Mater. Sci. Eng. A **838**, 142792 (2022)
34. M. Galatanu, M. Enculescu, A. Galatanu, Thermophysical properties of Cu-ZrO2 composites as potential thermal barrier materials for a DEMO W-monoblock divertor. Fusion Eng. Des. **127**, 179–184 (2018)
35. T.B. Massalski, H. Okamoto, P.R. Subramanian, L. Kacprzak, Binary alloy phase diagrams Vol. 1, The Materials Information Society, ASM International (1990)
36. J. Rösler, E. Arzt, A new model-based creep equation for dispersion strengthened materials. Acta Metall. Mater. **38**(4), 671–683 (1990)
37. S. Barcikowski, V. Amendola, G. Marzun, C. Rehbock, S. Reichenberger, D. Zhang, B. Gökce, Handbook of laser synthesis of colloids (2016)
38. M. Lenling, H. Yeom, B. Maier, G. Johnson, T. Dabney, J. Graham, P. Hosemann, D. Hoelzer, S. Maloy, K. Sridharan, Manufacturing oxide dispersion-strengthened (ODS) steel fuel cladding tubes using the cold spray process. JOM **71**(8), 2868–2873 (2019)
39. M. Nagini, R. Vijay, K.V. Rajulapati, K.B.S. Rao, M. Ramakrishna, A.V. Reddy, G. Sundararajan, Effect of process parameters on microstructure and hardness of oxide dispersion strengthened 18Cr ferritic steel. Metall. Mat. Trans. A **47**(8), 4197–4209 (2016)
40. Y. Yang, C. Doñate-Buendía, T.D. Oyedeji, B. Gökce, B.-X. Xu, Nanoparticle tracing during laser powder bed fusion of oxide dispersion strengthened steels. Materials (Basel, Switzerland) (2021). https://doi.org/10.3390/ma14133463
41. D. Zhang, A. Prasad, M.J. Bermingham, C.J. Todaro, M.J. Benoit, M.N. Patel, D. Qiu, D.H. StJohn, M. Qian, M.A. Easton, Grain refinement of alloys in fusion-based additive manufacturing processes. Metall. Mat. Trans. A **51**(9), 4341–4359 (2020)
42. D.J. Park, H.G. Kim, Y.I. Jung, J.H. Park, B.K. Choi, J.H. Yang, Y.H. Koo, Fabrication and mechanical properties of an oxide-dispersion-strengthened FeCrAl alloy. Fusion Eng. Des. **139**, 81–85 (2019)
43. M.C. Sow, T. de Terris, O. Castelnau, Z. Hamouche, F. Coste, R. Fabbro, P. Peyre, Influence of beam diameter on laser powder bed fusion (L-PBF) process. Addit. Manuf. **36**, 101532 (2020)
44. C. Ma, L. Chen, J. Xu, J. Zhao, X. Li, Control of fluid dynamics by nanoparticles in laser melting. J. Appl. Phys. **117**(11), 114901 (2015)
45. C. Ma, L. Chen, C. Cao, X. Li, Nanoparticle-induced unusual melting and solidification behaviours of metals. Nat. Commun. **8**(1), 14178 (2017)
46. M. Qu, Q. Guo, L.I. Escano, S.J. Clark, K. Fezzaa, L. Chen, Mitigating keyhole pore formation by nanoparticles during laser powder bed fusion additive manufacturing. Addit. Manuf. Lett. **3**, 100068 (2022)
47. O.A. Alawi, N.A.C. Sidik, H.W. Xian, T.H. Kean, S.N. Kazi, Thermal conductivity and viscosity models of metallic oxides nanofluids. Int. J. Heat Mass Transf. **116**, 1314–1325 (2018)
48. C. Ma, J. Zhao, C. Cao, T.-C. Lin, X. Li, Fundamental study on laser interactions with nanoparticles-reinforced metals—part I: effect of nanoparticles on optical reflectivity, specific heat, and thermal conductivity. J. Manuf. Sci. Eng. (2016). https://doi.org/10.1115/1.4033392
49. C. Ma, J. Zhao, C. Cao, T.-C. Lin, X. Li, Fundamental study on laser interactions with nanoparticles-reinforced metals—part II: effect of nanoparticles on surface tension, viscosity, and laser melting. J. Manuf. Sci. Eng. (2016). https://doi.org/10.1115/1.4033446
50. E. Fazio, B. Gökce, A. de Giacomo, M. Meneghetti, G. Compagnini, M. Tommasini, F. Waag, A. Lucotti, C.G. Zanchi, P.M. Ossi, M. Dell'Aglio, L. D'Urso, M. Condorelli, V. Scardaci, F. Biscaglia, L. Litti, M. Gobbo, G. Gallo, M. Santoro, S. Trusso, F. Neri, Nanoparticles engineering by pulsed laser ablation in liquids: concepts and applications. Nanomaterials (2020). https://doi.org/10.3390/nano10112317

51. D. Zhang, B. Gökce, S. Barcikowski, Laser synthesis and processing of colloids: fundamentals and applications. Chem. Rev. **117**(5), 3990–4103 (2017)
52. F. Waag, W.I.M.A. Fares, Y. Li, C. Andronescu, B. Gökce, S. Barcikowski, Identification of the main mixing process in the synthesis of alloy nanoparticles by laser ablation of compacted micropowder mixtures. J. Mater. Sci. **57**(4), 3041–3056 (2022)
53. Y. Yang, P. Kühn, M. Yi, H. Egger, B.-X. Xu, Non-isothermal phase-field modeling of heat–melt–microstructure-coupled processes during powder bed fusion. JOM **72**(4), 1719–1733 (2020)
54. J.Q. Xu, L.Y. Chen, H. Choi, X.C. Li, Theoretical study and pathways for nanoparticle capture during solidification of metal melt. J. Phys. Condens. Matter **24**(25), 255304 (2012)
55. J. Xu, Achieving uniform nanoparticle dispersion in metal matrix nanocomposites. UCLA Dissertations, 2015
56. L. Bergström, A. Meurk, H. Arwin, D.J. Rowcliffe, Estimation of Hamaker constants of ceramic materials from optical data using Lifshitz theory. J. Am. Ceram. Soc. **79**, 339–348 (1996)
57. German Social Accident Insurance Information system on hazardous substances (GESTIS). https://gestis-database.dguv.de/. Accessed 28 Nov 2022

Appendix B: Study II

Goßling, M., Rittinghaus, S.-K., Radtke, F., Elsayed, A., Kuşoğlu, I.M., Hariharan, A., Krupp, U., Gökce, B. (2024)

Oxide Distribution in PBF-LB/M-Processed ODS Steel: Effects of Ball Milling and Dielectrophoretic Deposition in Powder Production.

Powder Metallurgy, 68 (1), 29-40

DOI: 10.1177/00325899241304735

Original Research Article

I·M3 Institute of Materials, Minerals & Mining

Powder Metallurgy
1–12

DOI: 10.1177/00325899241304735
journals.sagepub.com/home/pmg


Oxide distribution in PBF-LB/M-processed ODS steel: Effects of ball milling and dielectrophoretic deposition in powder production

Mareen Goßling[1], Silja-Katharina Rittinghaus[1], Felix Radtke[2], Abdelrahman Elsayed[3], Ihsan Murat Kuşoğlu[4], Avinash Hariharan[3], Ulrich Krupp[3] and Bilal Gökce[1]

Abstract

This study provides key insights into the critical role of nanoparticle distribution in oxide dispersion-strengthened (ODS) powders for laser powder bed fusion (PBF-LB/M). A comparative analysis of mechanical (ball milling, BM) and liquid-based (dielectrophoretic deposition, DD) additivation methods was conducted to produce ODS feedstocks by integrating 1 vol.-% yttria (Y_2O_3) nanoparticles into Fe20Cr metal powder. ODS materials enhance high-temperature strength and creep resistance by dispersing fine, stable oxide particles within a metal matrix. This makes the precise size and distribution of nanoparticles crucial in the final bulk material. Powder characterisation shows that while both methods produce powders suitable for high-density parts, the DD method achieves higher uniform nanoparticle distribution, with smaller average particle sizes (74 nm) and interparticle distances (826 nm). In contrast, longer milling durations resulted in slightly larger particle sizes (77 nm) and distances (790 nm), while shorter milling times produced even larger nanoparticles (108 nm) with greater interparticle distances (1114 nm). These results suggest that DD offers advantages in optimising the distribution of oxide nanoparticles to enhance the strengthening effects in high-temperature applications.

Keywords

nanoparticle additivation, laser powder bed fusion, mechanical alloying, liquid-based, interparticle distance

Received: 13 September 2024; accepted: 18 November 2024

Introduction

Additive manufacturing (AM) has emerged as a transformative technology with significant implications for modern industries. Particularly in producing complex geometries, the versatility of AM has positioned it as a crucial player in advancing manufacturing processes. Among the materials explored for AM, oxide dispersion strengthened (ODS) steels stand out due to their unique properties, such as high-temperature resistance and mechanical strength, making them particularly relevant for high-temperature applications such as fusion power plants.[1]

ODS steels are engineered to withstand extreme thermal and mechanical conditions, preventing creep deformation in challenging environments.[2] Due to the strong interaction between dislocations and nanoscale oxide particles, they exhibit significantly enhanced creep resistance compared to dispersion-free ferritic steels. This dislocation interaction stabilises the microstructure during creep and forms dislocation loops around the oxide nanoparticles (ONP), impeding dislocation movement and delaying high-temperature deformation.[3] Well-known ODS steels, including EUROFER,[4] MA956[5] and PM2000, show 20% increase in compression strength at 600°C for ODS fabricated via AM compared to raw steel matrix.[6] The conventional manufacturing of ODS steels involves intricate and expensive processes with several process steps, such as sintering with subsequent high isostatic pressing (HIP), to ensure the homogeneous distribution of ONPs within the

[1]Chair of Materials Science and Additive Manufacturing, University of Wuppertal, Wuppertal, Germany
[2]Chair and Institute for Materials Applications in Mechanical Engineering, RWTH Aachen University, Aachen, Germany
[3]Chair of Materials Engineering of Metals at IEHK Steel Institute, RWTH Aachen University, Aachen, Germany
[4]Technical Chemistry I, Center for Nanointegration Duisburg-Essen (CENIDE), University of Duisburg, Essen, Germany

Corresponding author:
Bilal Gökce, Chair of Materials Science and Additive Manufacturing, University of Wuppertal, Wuppertal, Germany.
Email: goekce@uni-wuppertal.de

metallic matrix. This homogeneous distribution is crucial for the Orowan mechanism to function effectively at high temperatures.[7] Both ONP size and distance are essential criteria for achieving the desired properties.[4] This makes homogeneous ODS powder material a critical precondition, as this initially defines the best possible outcome.

While AM offers the advantage of producing complex geometries, the limited availability of powder variants, particularly for high-demand applications, poses a significant challenge. Specifically, the demand for and research on ODS materials continuously increases[8] as AM represents a comparatively uncomplicated process family for producing this type of material. Thus, the successful integration of AM in processing ODS steels has already been demonstrated multiple times,[8–10] but choosing suitable powder production processes remains a critical factor. For high-quality ODS powders, ONP must be combined with micron-size metal particles so that the metallic particles are homogeneously covered with ONP, while agglomeration or the loss of ONP is to be avoided. This is even more important as the involvement of a liquid phase and melt pool currents increases the risk of ONP assemblages occurring.[11–13] Mechanically alloying is the most widely employed method due to its ease of use. However, mechanically alloyed powder is often deformed due to the high applied forces during milling.[14] Deviations from the spherical shape may hinder flowability,[15] which is crucial for a homogeneous powder spread during layer-wise manufacturing. Thus, the quality of the resulting parts can be seriously affected.[16] Gentler methods, for example, mixing in a tumble mixer, pose the risk of insufficient bonding of ONP and metal particles and, thus, inhomogeneous distribution of ONP in the final part.[17] More elaborate methods, such as liquid-based, seem counterintuitive at first glance, as incorporating liquids in preferably dry powders to minimise gas porosity is not the most apparent solution. However, recent studies have shown that this process is suitable for producing ODS powders for high-density parts.[18]

Most studies in the field of ODS powders focus on a single powder production method or limited powder characteristics, such as particle size or chemical composition.[16,19–21] This has resulted in a lack of comprehensive comparative studies that quantitatively evaluate how different ODS powder production processes influence the properties of the final powder. Furthermore, the use of various matrices (PM2000,[22] MA956,[5] 14YWT,[10] and aluminum alloys)[23,24] complicates direct comparisons. To address this gap, the present study conducts an in-depth investigation of two distinct powder additivation methods—ball milling (BM) with varying durations and dielectrophoretic deposition (DD)—for producing ODS powders specifically tailored for AM via laser powder bed fusion (PBF-LB/M). The focus is on incorporating 1 vol.-% (~0.6 wt.-%) yttria (Y_2O_3) nanoparticles into Fe20Cr metallic powder. By evaluating powder characteristics in detail, the study aims to assess the effectiveness of each additivation method in achieving uniform dispersion of oxide nanoparticles within the metallic matrix, which is critical for successful processing in PBF-LB/M. The microstructural analysis conducted here will be crucial for understanding the impact of these powder preparation methods on the subsequent consolidation behaviour during PBF-LB/M processing.

Materials and Methods

Micrometer-sized metal powder with the nominal composition Fe20Cr (wt.-%) was used as the base material for producing oxide-additivated metal powder. The initial particle size distribution (PSD), as provided by the manufacturer (Rosswag GmbH, Pfinztal, Germany), ranged from 15 to 45 µm ($d_{10} = 20.16$ µm, $d_{50} = 34.92$ µm, $d_{90} = 62.50$ µm). The chemical composition of the Fe20Cr powder was verified by X-ray fluorescence (XRF), confirming a composition of 79.6Fe-20.4Cr (wt.-%, 78.43Fe-21.57Cr at.-%). Ceramic Y_2O_3 ONPs with an average particle diameter of 32 to 36 nm and a purity of 99.9% from Goodfellow Cambridge Ltd were used for additivation. As a PBF-LB/M platform substrate material, AISI 316L was used.

Processing. Low-energy BM was performed using a centrifugal mill (Retsch S1). For producing ODS powder, an empty yttrium-stabilized zirconium oxide (YSZ) container (500 ml) was initially loaded with 300 g of YSZ milling balls (10 mm in diameter). Fe20Cr metal powder (300 g) was then added, followed by the ONPs, which were spread over the metal powder and manually pre-mixed with a spatula to ensure initial distribution. This mixture was then transferred into the centrifugal mill for further mechanical mixing. Longer grinding times can lead to a finer distribution of the ONPs,[25] improving the final material's homogeneity properties. However, a longer grinding time can also lead to more significant deformation and fragmentation of the powder particles, resulting in smaller particle sizes and potential flowability issues.[26] The ball-to-powder ratio (BPR), which significantly impacts the morphology and consequently the flowability of the powder compared to grinding time,[14] was therefore kept constant in this study. Two parameter sets were applied on different powder batches: two cycles of 60 minutes at 70 rpm in air (BM/120 min) and two cycles of 20 minutes at 70 rpm in argon (Ar4.6) atmosphere (BM/40 min). This variation allows the study of ONP distribution in the powder and its subsequent effect on the properties of the printed parts produced with PBF-LB/M.

For the DD process,[27] 250 ml of deionised water (pH 8) was first added to a 1-litre vessel, followed by the addition of 300 g of Fe20Cr metal powder. This mixture was briefly pre-mixed manually to ensure even dispersion of the metal powder. Separately, the ONPs were dispersed in 150 ml of deionised water using an ultrasonic finger (Hielscher GmbH, UP200S) with an amplitude of 75% and a cycle of 0.75 for 2 minutes. The pre-dispersed ONP solution was then added to the vessel containing the water and metal powder, and the entire mixture was manually remixed to ensure uniform ONP distribution. This final mixture was subsequently transferred to a rotary evaporator, where it was dried at 80°C under a 320-mbar atmosphere for approximately 6 hours, with the rotation speed adjusted between 80 and 20 rpm depending on the drying progress.

The reference metal powder and additivated powders were processed using PBF-LB/M (Aconity Mini, Aconity GmbH, Herzogenrath, Germany). The different additivation methods and powder properties can cause potential variations in process behaviour. For this reason, a wide range of process parameters was selected to compensate for these variations. This approach ensures that each material, despite its unique characteristics, can be processed under conditions most likely to produce dense samples. Nine cubes ($10 \times 10 \times 10$ mm^3) were built using identical parameter sets in one built job for each powder material with laser powers (Ytterbium laser, $\lambda = 1070$ nm) between 175 and 220 W, scan speeds between 700 and 915 mm/s, and hatch distances varied between 70, 80 and 90 µm. The laser spot diameter was 50 µm, and the nominal powder layer thickness was 30 µm.

Analytical methods. The Y_2O_3 nanoparticles were investigated with transmission electron microscopy (TEM) using a JEOL, JEM-2200FS machine. PSD of the ODS and reference powder were determined using dynamic image analysis. Scanning electron microscopy (SEM; Apreo S LoVac, Thermo Fisher Scientific) provided insights into powder morphology, while energy dispersive spectroscopy (EDS) allowed quantitative comparison of nanoparticle distribution in the ODS powder. The flow rate and apparent density of the metal and additivated powders were determined using a Hall flowmeter, following the procedures outlined in ASTM B213 and ASTM B212. Flow rate (F_{RH}) was reported in (g/s), and apparent density (AD) in (g/cm^3). The percent packing density (PD) was calculated using the theoretical density of Fe20Cr (ρFe20Cr = 7.724 g/cm^3). Flowability was also analysed using a rotating drum test. The relative humidity was measured with a DBS moisture analyser (Kern & Sohn GmbH). Approximately 10 g of powder was rapidly heated to 150°C for 10 minutes, and the mass loss was expressed as a percentage. The Fe20Cr base, ODS powder and bulk samples were subjected to XRF analysis using a Bruker S8 Tiger instrument equipped with a rhodium X-ray tube and a beryllium window that operates at a power of 4 kW. For powder measurement, 5 g of the virgin and additivated powders were analysed under a helium atmosphere. The printed samples were halved, and the cross-sections representing scanning direction were prepared by grinding with 180-grit paper to obtain a flat surface before surface analysis. The bulk samples were measured under vacuum with an region of interest (ROI) of 8 mm in diameter. The Quant-Express quantitative method, designed for the Bruker system, determined each element's weight percentage (wt.%) through the corresponding Kα lines.

Microstructural analysis was conducted using light optical microscopy (LOM) on metallographically prepared cross-sections, employing a Leica DM-2700 microscope. Density measurements were performed on each sample using five LOM images taken at a magnification of 50x, with images distributed across the entire build height and width of the cross-sections to ensure comprehensive coverage. The densities of the samples were measured using ImageJ software (Version 1.54j). For SEM analysis, images of the PBF-LB/M reference and ODS samples were captured at various magnifications. The interparticle distance was calculated from 4 to 8 images taken at 5kx magnification, while particle size was measured at higher magnifications of 80kx and 120kx to enhance accuracy. Pairwise Euclidean distances between particles were computed using the numpy linear algebra norm function (np.linalg.norm). The minimum distances were averaged to obtain the mean minimum distance, indicating particle clustering. Analysis was conducted using Python with the Pandas, Numpy and Matplotlib libraries.

Results and discussion

ONP characteristics. TEM analysis was performed on the Y_2O_3 ONP to assess their morphology and elemental composition. Figure 1 presents TEM images of the ONP in as-received condition and a line scan of one representative Y_2O_3 particle.

The TEM images (Figure 1(a) and (b)) reveal that the Y_2O_3 nanoparticles (NPs) exhibit a variety of morphologies, including spherical (Figure 1(a)), plate-like (Figure 1(b)), and irregular geometries that are plate-like but not symmetrical. The majority of the particles are angular and plate-like. Additionally, the images indicate a narrow size distribution among the nanoparticles. A spherical particle shape and uniform sizes are advantageous for consistent material properties in the final part. The line scan (Figure 1(c)) confirms a homogeneous distribution of yttrium (Y) and oxygen (O) throughout the nanoparticles, verifying their composition as Y_2O_3. Notably, no core-shell

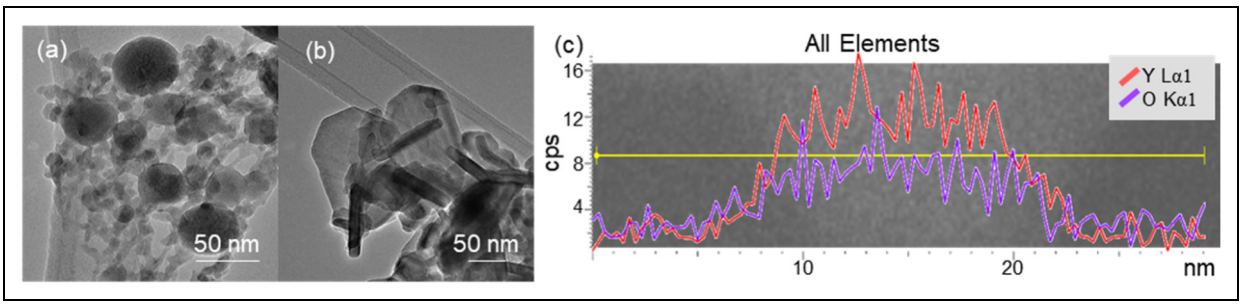

Figure 1. Transmission electron microscopy image showing (a) spherical Y_2O_3 nanoparticles and (b) plate-like Y_2O_3 nanoparticles. (c) Line scan of Y_2O_3 nanoparticle indicating the elemental distribution of yttrium (Y) and oxygen (O).

structures were detected. However, the observed plate-like morphology of some Y_2O_3 nanoparticles poses a potential concern. According to the theory of ODS materials,[28] a homogenous distribution and size of powder particles with a small interparticle distance,[29] either through high particle loading or smaller particles, support the strengthening effect more effectively in high-temperature environments.[30] Therefore, a spherical shape of the reinforced particles supports the homogenous interparticle distance and may positively affect the strengthening.[28,31] The plate-like shapes might lead to anisotropic mechanical properties and less effective pinning of dislocations, which could compromise the material's performance under thermal and mechanical stress. During the melting and solidification processes in laser-based AM processes, the strengthening effect can also be altered due to the distribution of ONP and microstructure characteristics like grain size.[6] With the varying process parameters, the size of the ONP can be changed.[32–34] Despite their high melting point of 2430 +/− 25°C,[35] the local energy densities of the laser radiation are high enough to exceed this temperature in the melt pool and cause partial melting,[34] resulting in rounding and even dissolving of the smallest ONP. Similar effects are observed, for example, in WC-containing coatings applied by laser cladding.[36,37]

Particle morphology and ONP distribution of ODS powders. Figure 2 presents the results of SEM and EDS analyses of powder particles, comparing the reference

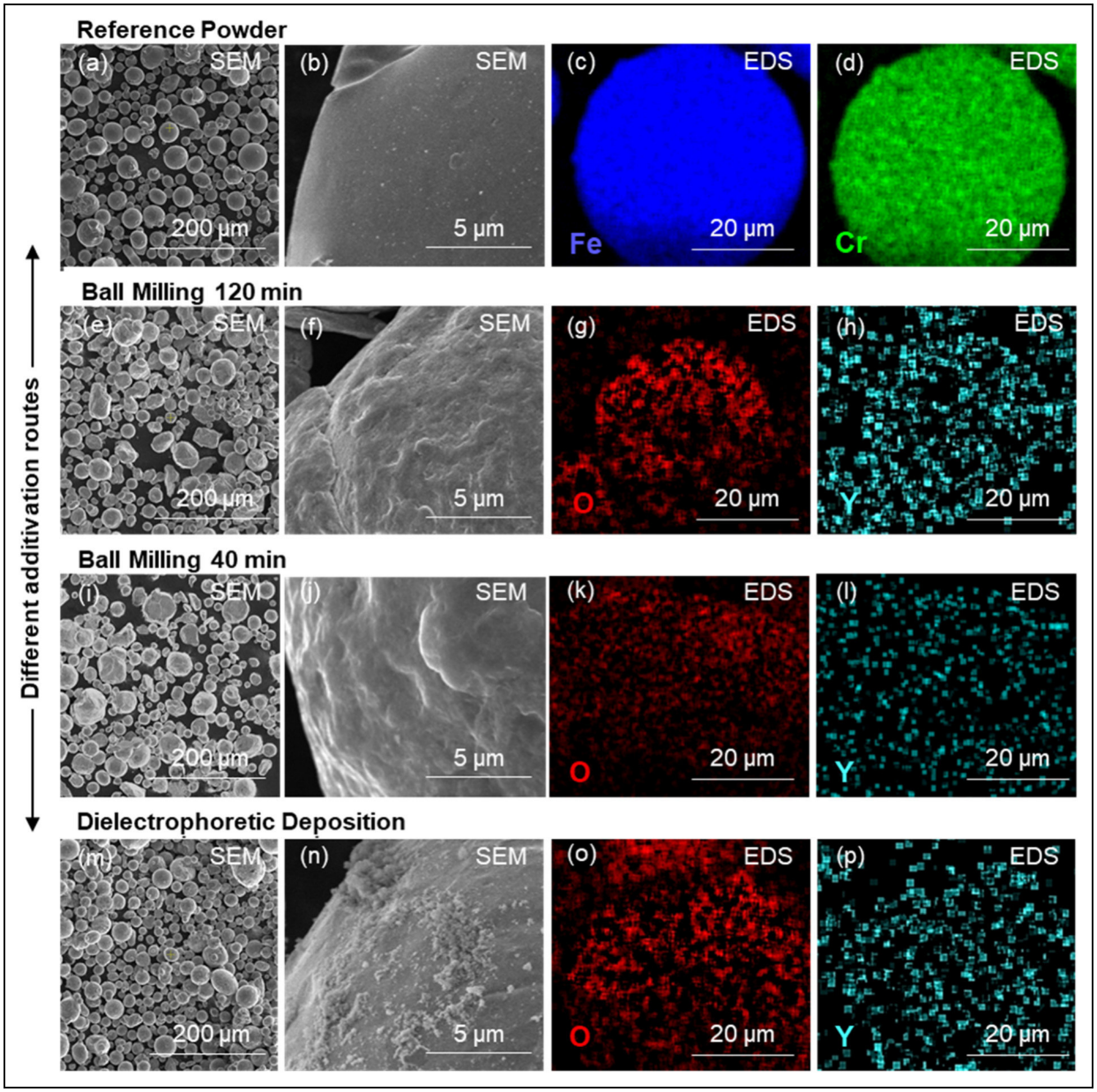

Figure 2. (a) and (b) SEM image of the reference powder. (c) and (d) EDS elemental maps of the reference powder showing Fe and Cr distribution. (e) and (f) SEM image of powder after BM/120 min. (g) and (h) EDS elemental maps of powder after BM/120 min showing O and Y distribution. (i) and (j) SEM image of powder after BM/40 min. (k) and (l) EDS elemental maps of powder after BM/40 min showing O and Y distribution. (m) and (n) SEM image of powder after DD. (o) and (p) EDS elemental maps of powder after DD showing O and Y distribution. BM: ball milling; DD: dielectrophoretic deposition; EDS: energy dispersive spectroscopy; SEM: scanning electron microscopy.

powder with powders additivated using the different routes of BM and DD.

The SEM images reveal distinct particle morphology and size distribution differences among the powders. The reference powder (Figure 2(a)) comprises well-rounded particles typical for gas atomisation. In contrast, the powders subjected to BM (Figure 2(e) and (i)) exhibit slightly altered shapes with increased surface roughness, indicating mechanical deformation during milling. The visual comparison between BM/120 min and BM/40 min does not reveal a noticeable difference in particle morphology, indicating that the milling duration (BM/120 min vs. BM/40 min) does not significantly affect this aspect. Notably, the DD additivated powder (Figure 2(m) and (n)) shows distinguishable nanoparticles on the surface, appearing as whitish dots or flakes. The appearance of whitish areas contrasts with the BM powders, whose nanoparticles are not discernible via SEM, likely due to their embedding within the roughened surfaces.

EDS elemental maps (Figure 2(b)–(d), (g), (h), (l), (l), (o) and (p)) provide insights into the elemental distribution of Fe, Cr, O and Y. Despite different additivation methods, no significant differences in Y distribution are observed among the powders. This could be attributed to the limited sensitivity of EDS in detecting the low Y content (1 vol.-%) and the small particle size of the Y_2O_3. The detection limitations of EDS at low Y concentrations prevent definitive conclusions regarding the uniformity and aggregation behaviour of the nanoparticles across the different additivation routes. Further, more sensitive techniques might be required to assess the nanoparticle distribution accurately. As far as the observations show, the distribution of the Y is predominantly uniform, regardless of the additivation method.

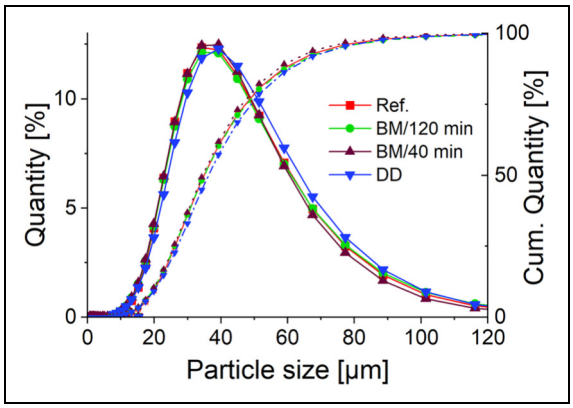

Figure 3. Percentual and cumulated particle size distribution of powder additivated with different routes.

Physical properties of ODS powders. Dynamic image analysis was utilised to quantify powders' PSD processed with the different additivation routes. The results are presented in Figure 3.

The PSD analysis indicates no significant difference between the reference powder and the powders processed through BM (BM/120 min and BM/40 min) and DD. All samples exhibit a similar distribution, with D_{10}, D_{50} and D_{90} values closely aligned across the different methods. This suggests that the additivation processes do not markedly alter the overall PSD of the Fe20Cr powder, even though the DD curve tends to shift to larger sizes compared to the reference and BM powders. Table 1 summarises PSD values of the powders and the related physical properties determined in this study.

The PSD also shows slightly larger average particle sizes, so it is assumed that ONP agglomerates could have occasionally led to the binding of the Fe20Cr particles. The standard deviation of the size values is within a maximum of 2%, with the D90 value for the DD sample showing a deviation of only 0.72 µm. Therefore, even within these minor deviations, the particle size remains slightly increased, supporting the observation that ONP agglomerates may have contributed to the binding of the Fe20Cr particles. However, there is no indication of such phenomena from SEM analysis of the ODS powders. Unlike the BM powder, where the nanoparticles are more uniformly integrated into the matrix, the DD powder shows nanoparticles prominently on the surface (Figure 2(n)). Considering the relatively high loading of 1 vol% for ODS steels in AM, the surface coverage by the nanoparticles is very dense. In the SEM images, several areas where ONP agglomerations up to 1.5 µm in height are visible can be identified. When converted to diameter, these accumulations can increase the detection of small particles < 10 µm in the PSD. The relative humidity of the powders remains low, around 0.09–0.11%, indicating minimal moisture content not affected by additivation routes. This shows that a liquid phase in the DD does

Table 1. PSD (D_{10}, D_{50}, D_{90}), relative humidity, flow rate (FR_H), AD, TD, Hausner Ratio and PD of reference powder Fe20Cr and additivated Fe20Cr + 1 vol.% Y_2O_3 powder.

Additivation route	PSD			Rel. humidity	Flow rate	Apparent density	Tap density	Hausner ratio	Packing density
Parameter	D_{10}	D_{50}	D_{90}	rel. H	FR_H	AD	TD	HR	PD
Unit	[µm]	[µm]	[µm]	[%]	[g/s]	[g/cm³]	[g/cm³]	[-]	[vol.-%]
Reference	20.16	34.92	62.50	0.11	2.46	3.70	4.76	1.29	48.00
BM/120 min	19.84	34.96	63.46	0.09	2.46	3.85	4.69	1.22	48.86
BM/40 min	19.69	34.51	60.34	0.09	2.46	3.97	4.69	1.18	50.40
DD	20.30	36.22	64.37	0.09	2.27	3.98	4.35	1.09	50.52

AD: apparent density; BM: ball milling; DD: dielectrophoretic deposition; PD: packing density; PSD: particle size distribution; TD: tap density.

not directly influence the residual moisture after the corresponding drying step. Flow rates are similar for all samples, with the reference and BM powders exhibiting a slightly higher flow rate than the DD powder. This difference can be partially attributed to interparticle friction effects, which influence flow characteristics alongside packing density and apparent density results. In the DD powder, the higher apparent and packing densities suggest a denser particle arrangement with potential interparticle friction reduction due to ONP surface distribution. The surface roughness of the DD powder and the agglomeration of ONP may lead to slightly increased interparticle friction, resulting in a lower flow rate compared to BM powders. Apparent density and tap density values show some variation, with the DD method resulting in the highest apparent density (3.98 g/cm^3) and the lowest Hausner ratio (1.09), suggesting better packing efficiency and flowability. The packing density follows a similar trend, with the DD method achieving the highest value (50.52 vol.-%). The unprocessed, gas-atomized reference powder is expected to have the lowest packing density due to its unchanged sphericity. The potentially reduced sphericity in the BM/120 min and specifically in the BM/40min powder could lead to increased particle interlocking. This interlocking can result in higher packing densities. This could also occur for the DD powder due to the rougher surface and agglomeration of the NP. The morphology of mechanically alloyed powders may be influenced more strongly by the ball-to-powder ratio than by the milling time.[14] Since the BPR remained constant between BM/120 min and BM/40 min, significant packing density differences between these powders are not expected. While the DD technique showed promising results in terms of particle distribution, density and flowability, it is important to consider the reproducibility of this method. In this study, each experimental result is based on a single batch, which limits our ability to fully evaluate consistency across multiple production runs. Several factors could influence reproducibility in DD, including environmental variables like ambient humidity and room temperature, as well as fluctuations in water temperature during the dispersion process or PSD of metal and nanopowders. Small variations in these conditions could impact the behaviour of the nanoparticles in solution, their distribution on the metal particles, and the drying dynamics within the rotary evaporator.

Processability of ODS powders. Table 2 shows the process parameters and resulting densities of samples produced from the reference powder and additivated powders via BM (BM/120 min and BM/40 min) and DD. Identical parameter sets were tested within each respective build job to evaluate the influence of the different ODS powders on the production of high-density samples by PBF-LB/M.

The results show high densities with values consistently above 99.8% could be reached within the analyzed process window for studied powders. The lowest porosities for samples built from reference powder, BM/40 min and DD were achieved with 220 W, 915 mm/s and a 70 µm hatch distance, resulting in 99.98%, 99.94% and 99.92% relative density, respectively. For BM/120 min, the highest density of 99.94% was measured using 210 W, 840 mm/s and 80 µm hatch distance. However, all samples produced from ODS powders exhibit a lower density than the reference Fe20Cr samples. Figure 4 shows a cross-section of the samples with the highest densities of the reference and NP-loaded powder with different additivation routes BM/120 min, BM/40 min and DD. In samples with added ONPs, the number and size of micropores is slightly increased. The reasons for this have not yet been conclusively investigated, and considerations include melt pool

Table 2. Varied PBF-LB/M process parameters laser power (P_L), scan velocity (v_s) and hatch distance (Δy_s) with fixed layer height (D_s=30 µm) used in this study with respective resulting relative sample densities.

Process parameters with layer height D_s=30 µm				Powder material			
P_L	v_s	Δy_s	E_v	Reference	BM/ 120 min	BM/ 40 min	DD
[W]	[mm/s]	[µm]	[J/mm³]	Relative density [%]			
175	700	80	104.167	99.94	99.90	99.89	99.87
200	800	70	119.048	99.96	99.83	99.85	99.91
200	800	80	104.167	99.96	99.83	99.88	99.85
200	800	90	92.593	99.94	99.89	99.89	99.88
210	735	80	119.048	99.96	99.90	99.91	99.88
210	840	80	104.167	99.94	**99.93**	99.92	99.92
220	800	80	114.583	99.97	99.88	99.87	99.90
220	915	70	114.494	**99.98**	99.88	**99.94**	**99.92**
220	710	90	114.763	99.96	99.88	99.92	99.87

E_v represents the volumetric energy density $Ev = P_L/(\Delta y_s D_s v_s)$ [38] to ease comparison with related studies. Density values below 99.90% are marked in orange, while a green background marks the highest density values for each material. Bold font indicates the selected samples for subsequent analysis.
BM: ball milling; DD: dielectrophoretic deposition; PBF-LB: laser powder bed fusion.

dynamics, heat conductivity, absorption and evaporation being influenced by the ONPs.[39–41]

Moreover, the wettability of the ONPs in steel matrix is low, which may lead to related effects.[42] According to Table 1, moisture introduced by ONPs can be ruled out as the cause of increased pore formation. Notably, the pores for the ODS samples have an irregular shape, whereas the reference sample shows round pores, presumably due to gas inclusions. The irregular shape of the pores in the ODS samples might also indicate a lack of fusion during the PBF-LB/M process or be due to the poor wettability of the nanoparticles within the metal matrix. When the ONPs are not adequately wet with the surrounding molten metal during the PBF-LB/M process, it can lead to incomplete integration of the particles into the matrix. This inadequate bonding can create voids around the nanoparticles, forming irregularly shaped pores in the final sample.

The results indicate that all ODS powders demonstrate suitable processability with high-density outputs regardless of the additivation route. The variation in density is minimal among the different additivation methods, suggesting that the process window for achieving optimal density is not significantly affected. This implies that the powders' inherent properties, such as PSD and flowability, are sufficiently maintained across different additivation processes and do not alter the process dynamics to a critical degree. It is noticeable that the parameters to achieve high-density samples with BM/120 min powder differ from those needed for the other powders, and the overall densities are lower when using BM/120 min powder. The processing of BM/120 min under ambient air could significantly impact its processability, as the increased O content in the powder may lead to a higher incidence of defects.[43,44] In correlation with the higher determined Hausner ratio, it is assumed that the homogeneity of the whole powder is probably low after the long milling process. This means that analytical methods that involve only small quantities of powder may need to be evaluated more cautiously. An overall lower homogeneity might also explain variances during the PBF-LB/M process, especially regarding the powder spread and, thus, resulting densities.

Correlation between ODS powder and part composition. The chemical composition of the powders and the processed PBF-LB/M samples was analysed using XRF. The results are summarised in Table 3. According to the added 1 vol.-% Y_2O_3, the nominal expected Y_2O_3 content would be 0.6 wt.-%, and therefore, the Y content would be 0.47 wt.%.

The reference powder shows no detectable Y, as expected. Both BM variants (BM/120 min and BM/40 min) yield similar Y content in the ODS powders, approximately 0.6 wt.%, indicating that the BM process effectively combines Y_2O_3 nanoparticles with the Fe20Cr matrix powder. In contrast, the DD route shows a slightly lower Y content of 0.467 wt.%, suggesting that the supporting efficiency of this method should be further optimised in producing ODS powder despite the initial addition of the same amount of nanoparticles for additivation as in the other methods. The Y content tends to decrease by approximately 65% (BM/40 min) to 70% (DD) during PBF-LB/M processing. This reduction could be due to the loss of ONP during the process, possibly from evaporation or the removal of particles from the process zone by the shielding gas flow. This reduction may also involve re-precipitation

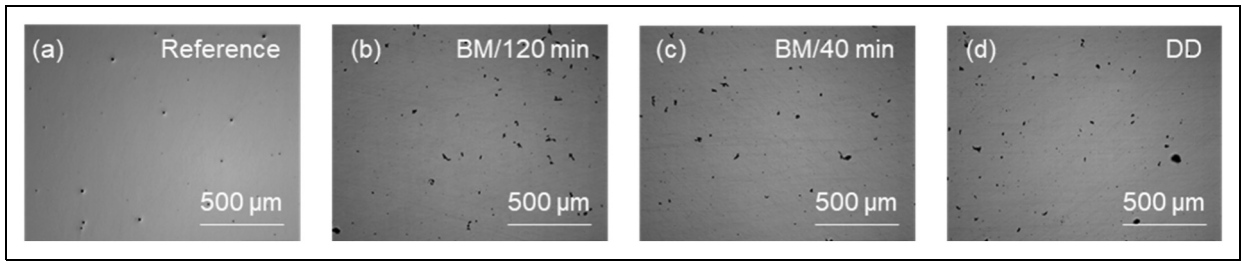

Figure 4. LM images of cross-sections of a reference (a), BM/120 min (b), BM/40 min (c) and DD (d) sample at 50× magnification. BM: ball milling; DD: dielectrophoretic deposition.

Table 3. Elemental composition of powders and PBF-LB/M produced samples analysed by XRF, values in wt.-%.

Condition	Additivation route	Fe	+/−	Cr	+/−	Y	+/−
	Unit	[wt.%]	[wt.%]	[wt.%]	[wt.%]	[wt.%]	[wt.%]
Powder	Reference	79.630	0.040	20.370	0.016	-	-
	BM/120 min	78.940	0.039	20.460	0.016	0.602	0.002
	BM/40 min	79.000	0.040	20.400	0.016	0.594	0.002
	DD	79.070	0.040	20.470	0.016	0.467	0.002
PBF-LB/M Samples	Reference	80.240	0.136	19.760	0.055	-	-
	BM/120 min	80.250	0.144	19.430	0.060	0.265	0.005
	BM/40 min	80.270	0.136	19.500	0.057	0.217	0.004
	DD	80.060	0.136	19.790	0.057	0.151	0.004

BM: ball milling; DD: dielectrophoretic deposition; PBF-LB: laser powder bed fusion; XRF: X-ray fluorescence.

of oxides under processing conditions, which could influence the observed oxide particle size and distribution in the solidified matrix. Although SEM was used to analyse these characteristics, it may not accurately reflect the true nano-oxide size due to agglomeration and surface effects. For a more precise determination, especially considering results from other studies on ODS steels where typical oxide sizes are closer to 10 nm,[34,45] techniques such as TEM could be employed in future works. The significant decrease in Y content from DD powder to the PBF-LB/M sample suggests that Y_2O_3 nanoparticles may interact with the melt differently during the PBF-LB/M process than BM. SEM analysis reveals that the ONPs in the DD powder are more concentrated on the surface. This positioning leads to greater exposure to laser radiation during processing. As a result, the nanoparticles may absorb more energy, increasing the likelihood of evaporation. However, this effect can only occur at the starting points of the scan vectors as the laser radiation is then absorbed by melt. It should, therefore, not be significant concerning the total volume of the samples. Additionally, there is a potential for NP ejection from the particle surface after interacting with the laser radiation. [46] Furthermore, the Cr content shows a slight reduction from approximately 20.5% in the powder to 19.5% in the final part, suggesting a possible loss of Cr during laser processing, likely due to the evaporation of Cr_2O_3 or elemental Cr. [47,48]

The discrepancy in Y content detection between powders and samples might be attributed to the XRF technique. The penetration depth of X-rays in XRF might affect the measurements. The analysed layer in powder measurements, which is the thickness of the sample that absorbs 90% of the intensity of the XRF line of interest, were around 100, 150 and 300 µm for Al, Cr and Y, respectively. However, the analysed layers in printed parts were 14, 20 and 39 µm. Here, sample surface preparation is crucial for detecting trace elements in a matrix. And 180 grit paper results in a surface roughness of around 25 µm and might result in lower Y amounts detected in parts. However, the grinding step might pull agglomerated Y_2O_3 particles from the Fe20Cr matrix due to low wettability between the two phases. Furthermore, an alternative XRF preparation methodology, such as oxidising powders with a glass forming matrix to form a glass bead where all elements are homogeneously distributed, might be recommended to understand the differences in Y contents in powder and part. This difference in nanoparticle positioning can lead to variations in the measured Y content, highlighting the need for complementary analytical techniques to obtain a higher accuracy in the assessment.

ONP size and distribution in PBF-LB/M parts. The theory of ODS highlights the importance of interparticle distance (IPD), particle size, and particle appearance in strengthening effects at high temperatures, making it crucial to examine these factors to optimise ODS material performance. Figure 5 shows SEM images of PBF-LB/M samples at various magnifications, illustrating the nanoparticle distribution and morphology in samples from BM/120min,

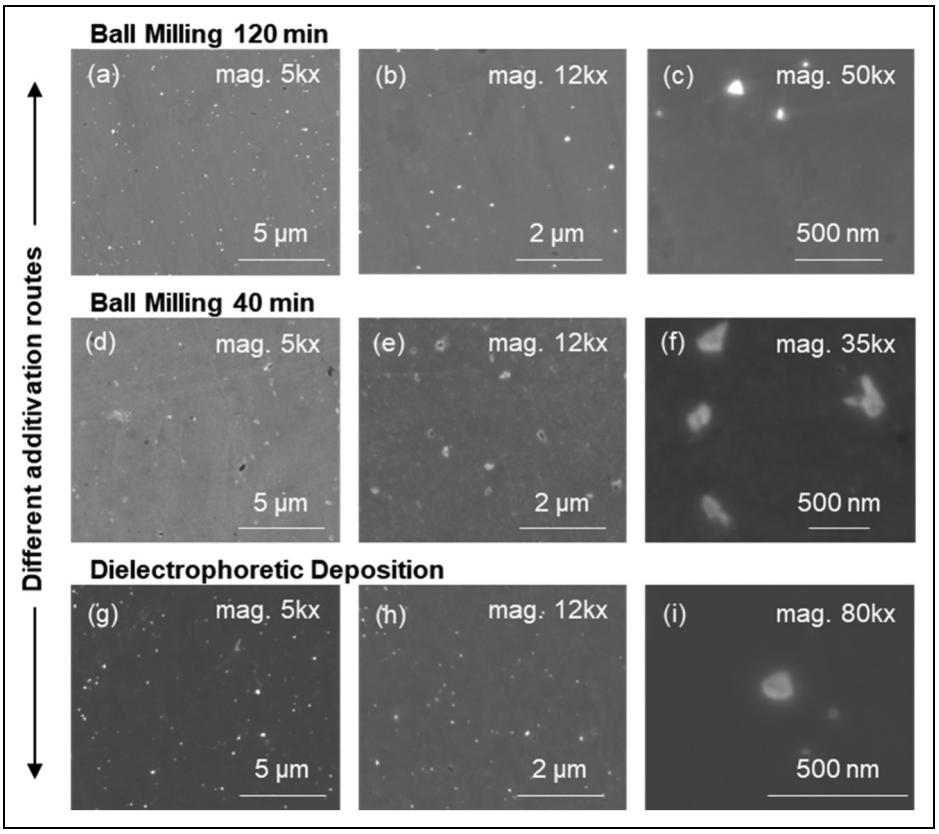

Figure 5. SEM images of PBF-LB/M samples in different magnification and additivation routes: (a)–(c) BM/120 min; (d)–(f) BM/40 min and (g)–(i) DD. BM: ball milling; DD: dielectrophoretic deposition; PBF-LB: laser powder bed fusion.

Table 4. Particle size and interparticle distance including SD.

Additivation route	Particle count	Average particle size	SD Particle size	Average IPD	SD IPD
Unit	[-]	[nm]	[nm]	[nm]	[nm]
BM/120 min	1298	77	29	790	79
BM/40 min	680	108	59	1114	363
DD	1194	74	23	826	103

BM: ball milling; DD: dielectrophoretic deposition; IPD: interparticle distance; SD: standard deviation.

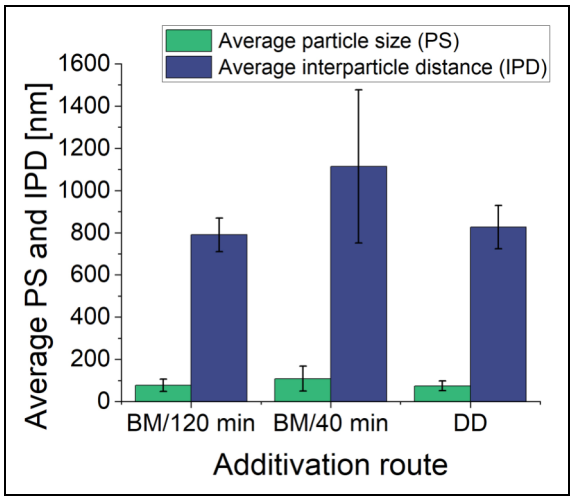

Figure 6. Average particle size and IPD of NP inclusions of the bulk samples additivated with different routes BM/120 min, BM/40 min and DD based on table 4. BM: ball milling; DD: dielectrophoretic deposition; IPD: interparticle distance.

BM/40min and DD powders. The measurements in Table 4, determined from SEM images at 5kx magnification, must be interpreted cautiously due to resolution limitations that could affect the accuracy of particle size and IPD values. However, the comparative analysis remains valid, as all measurements were consistently obtained under the same conditions. In addition to the numerical results from Table 4, the results are also visualised in Figure 6 for better comparison.

As observed in the SEM images, all samples contain visible ONP regions of various sizes, with larger areas likely being agglomerates (Figure 5(c), (f) and (i)). The lower detection limit for the ONP size is approximately 2 to 5 nm. Notably, the BM/40 min sample shows larger ONPs than the manufacturer's specifications and the other samples, indicating significant agglomeration during the shorter milling process and subsequent PBF-LB/M processing. The shorter milling time likely leads to agglomeration, which can also be observed with a gentler mixing process, such as tumbling. The ONPs tend to cluster during the initial milling stages, compounded by the van der Waals forces and density differences between the ONPs and metal powder. This results in a less uniform distribution of ONPs in the printed part, with an average particle size of 108 nm and a significantly larger IPD of 1114 nm, as detailed in Table 4. The elongated ONPs in this sample further suggest that the milling duration was insufficient to break down these agglomerates, leading to a less controlled distribution.

In contrast, the BM/120 min sample exhibits a finer and more uniform distribution of ONPs, with an average size of 77 nm and an IPD of 790 nm. The longer milling time facilitates the embedding of ONPs into the metal powder, causing the agglomerates to break down and resulting in smaller, more spherical particles, according to the literature.[25] This improved distribution is comparable to DD, where the ONPs are slightly smaller, averaging 74 nm, and better distributed, as indicated by a narrower size distribution and smaller error margin in Table 4 and Figure 6. Compared to the embedded ONP on the powder particles of the BM parts, the ONPs are additivated on the surface of the metal particle. The position of ONPs on the surface of the DD powder likely allows these nanoparticles to immediately interact with the surrounding melt pool during the PBF-LB/M process, resulting in greater oxide particle retention and distribution in the subsequently solidified microstructure.

In contrast, in the BM samples, where the ONPs are embedded within the metal matrix, the nanoparticles only interact with the melt pool once the powder particles have melted. This delayed interaction could contribute to the observed differences in particle size and distribution, as the ONPs in the BM samples might have less time to disperse evenly within the melt pool. Ultimately, while the analysis does not provide conclusive insights into the differences in nanoparticle size between the BM powder samples before processing, it is evident that the BM/120 min and DD methods produce a more favourable nanoparticle distribution for dispersion strengthening than the BM/40 min sample. The smaller nanoparticles and shorter interparticle distances observed in the DD sample are particularly beneficial for enhanced dispersion strengthening, as supported by previous studies.[28,29] Although the differences in size and distribution of BM/120min and DD are minimal, they may be more related to the initial size of the nanoparticles in the powder before processing rather than their position within the powder particles.

Conclusions

This study comprehensively investigated the impact of different additivation processes on the properties and processability of ODS powders tailored for the AM process of PBF-LB/M, addressing the growing demand for high-performance materials in complex shapes. An amount of 1 vol.-% Y_2O_3 NP was successfully additivated onto Fe20Cr powders using BM (ball milling) and DD (dielectrophoretic deposition) and subsequently processed into dense samples.

It was found that DD maintains the initial powder shape and surface, while oxide nanoparticles (ONPs) are homogeneously distributed on the Fe20Cr powder surface. BM powders show slight deformation and surface roughening, while ONPs are embedded into the Fe20Cr particles. In the SEM images, ONPs are not visible on the surface of the BM powders. In contrast, ONPs on the DD powder are uniformly distributed on the surface, forming some agglomerations. The exact distribution of the nanoparticles could not be further detailed using Y detection with EDS. ODS powder property analyses indicate that while the additivation routes do not significantly alter the PSD ($D_{50} \sim 35$ µm), the DD method may offer slight advantages in maintaining powder morphology and potentially in improving flow properties compared to BM. However, the observed differences show no apparent impact on the AM process. Compared to Fe20Cr reference material, ONP additivation does not significantly impact the maximum achievable density of the final parts. The processing window is reduced regardless of the selected additivation method, which indicates lower process stability. Deformed particles, partly visible in the BM samples, can lead to uneven powder deposition and defects in the printed parts. All additivation routes effectively introduced Y_2O_3 nanoparticles into the Fe20Cr matrix of PBF-LB/M parts. The BM/40min samples show larger ONPs and agglomerates (average size: 108 nm) and greater interparticle distances (1114 nm) than the BM/120min sample (77 and 790 nm) and DD sample (74 and 826 nm, respectively).

Although the DD method does not achieve a substantial difference in particle size or interparticle distance compared to the optimised BM/120 min process, it may be advantageous in applications requiring reduced deformation of particles and enhanced flowability due to its preservation of powder morphology. However, an adapted BM process could yield similar results by optimising milling parameters to achieve a finer and more uniform distribution of ONPs, as shown in the BM/120 min samples. Initially, plate-shaped ONPs could not be observed in the final samples, probably because they had either been dissolved or were below the SEM detection limit. The chemical analysis by XRF showed that both BM variants (BM/120 min and BM/40 min) had similar Y contents in the ODS powders (~0.6 wt.%), while the DD method resulted in a slightly lower Y content (0.467 wt.%). During PBF-LB/M processing, Y content decreased significantly, by approximately 65% (BM/40 min) to 70% (DD), likely due to evaporation or removal of nanoparticles from the process area, such as by the shielding gas flow.

While this study focuses primarily on the powder characterisation and oxide distribution in powders produced by ball milling and DD, it is acknowledged that mechanical properties are critical for assessing the overall performance of AM parts. The uniform dispersion of oxides within the powder is expected to influence the mechanical behaviour of the printed bulk material; however, this effect was not evaluated in the present study. The findings presented here lay the groundwork for future studies investigating the relationship between oxide distribution and the mechanical properties of AM parts. These future studies will enable a more comprehensive understanding of how powder characteristics affect the final material performance. Additionally, the nanoparticle distribution was primarily evaluated using SEM and EDS, which, due to resolution limits, may not fully capture the true size and dispersion of nanoparticles, particularly for oxides below 10 nm. Future studies should incorporate higher-resolution techniques such as TEM to provide a more accurate analysis of nanoparticle size and distribution, along with comprehensive mechanical testing, to more robustly establish the impact of nanoparticle dispersion methods on bulk material performance.

Acknowledgements

We want to thank Daniel Borchert, Leon Dippel and Nils Wiethoff for their support during the experiments and metallographic analysis. Additionally, we extend our gratitude to Ivan Zhirnov for his assistance in analysing the SEM images with ImageJ, Tobias Bochmann for his contributions to SEM and EDS imaging of the powder particles and Jurij Jakobi for his help with the XRF measurements. This manuscript was prepared with the aid of ChatGPT to refine sections of the text.

Author contributions

MG and FR were involved in conceptualisation, writing – original draft and investigation; S-KR in conceptualisation, writing – original draft; AE in investigation; IMK in investigation and writing – review & editing; AH and UK in writing – review & editing and BG in conceptualisation, funding acquisition and writing – review & editing.

Declaration of conflicting interests

The authors declared no potential conflicts of interest with respect to the research, authorship, and/or publication of this article.

Funding

The authors disclosed receipt of the following financial support for the research, authorship, and/or publication of this article: This research was conducted as part of the German Research Foundation (DFG) Priority Program 2122, "Materials for Additive Manufacturing" (SPP 2122, project number 493889809, GO 2566/13-1, and XU 121/20-1 and SPP2122 coordination project numbered 359962234). Additionally, B. Gökce acknowledges support from the DFG Heisenberg Program, project GO 2566/10-1 (445127149).

ORCID iD

Bilal Gökce https://orcid.org/0000-0001-6368-9659
Ihsan Murat Kuşoğlu https://orcid.org/0000-0002-1983-8343

References

1. Hoelzer DT (Advanced Materials and Manufacturing, 2018) *History and Outlook of ODS/NFA Ferritic Alloys for Nuclear Applications.* Philadelphia, Pennsylvania, USA.

2. Susila P, Sturm D, Heilmaier M, et al. Effect of yttria particle size on the microstructure and compression creep properties of nanostructured oxide dispersion strengthened ferritic (Fe–12Cr–2W–0.5Y2O3) alloy. *Mater Sci Eng: A* 2011; 528: 4579–4584.
3. Singh R, Prakash U, Kumar D, et al. Development of creep resistant high yttria 18Cr ferritic ODS steel through hot powder forging route. *J Nuclear Mater* 2023; 584: 154566.
4. Husák R, Hadraba H, Chlup Z, et al. ODS EUROFER steel strengthened by Y-(Ce, Hf, La, Sc, and Zr) Complex oxides. *Metals* 2019; 9: 1148.
5. Poudel B, Nguyen HX, Kwon P, et al. Selective laser melting of oxide dispersion strengthened MA956 alloy and its surface finishing by magnetic field assisted finishing. *J Manuf Process* 2023; 97: 220–234.
6. Doñate-Buendia C, Kürnsteiner P, Stern F, et al. Microstructure formation and mechanical properties of ODS steels built by laser additive manufacturing of nanoparticle coated iron-chromium powders. *Acta Materialia* 2021; 206: 116566.
7. Wang J, Liu S, Xu B, et al. Research progress on preparation technology of oxide dispersion strengthened steel for nuclear energy. *Int J Extrem Manuf* 2021; 3: 32001.
8. Wilms MB, Rittinghaus S-K, Goßling M, et al. Additive manufacturing of oxide-dispersion strengthened alloys: materials, synthesis and manufacturing. *Prog Mater Sci* 2023; 133: 101049.
9. Ghayoor M, Lee K, He Y, et al. Selective laser melting of austenitic oxide dispersion strengthened steel: processing, microstructural evolution and strengthening mechanisms. *Mater Sci Eng: A* 2020; 788: 139532.
10. Saptarshi S, deJong M, Rock C, et al. Laser powder bed fusion of ODS 14YWT from gas atomization reaction synthesis precursor powders. *JOM* 2022; 74: 3303–3315.
11. Stubbs T, Hou R, Leonard DN, et al. Dispersoid coarsening and slag formation during melt-based additive manufacturing of MA754. *Addit Manuf Lett* 2024; 9: 100195.
12. Nassar AR, Gundermann MA, Reutzel EW, et al. Formation processes for large ejecta and interactions with melt pool formation in powder bed fusion additive manufacturing. *Scientific Rep* 2019; 9: 5038.
13. de Luca A, Kenel C, Dunand DC, et al. Effect of HfO2 dispersoids on the microstructure of a Ni-Cr-Al-Ti superalloy processed by laser-based powder-bed fusion. *Addit Manuf Lett* 2023; 6: 100139.
14. Ansell TY, Hanneman T, Gonzalez-Perez A, et al. Effect of high energy ball milling on spherical metallic powder particulates for additive manufacturing. *Part Sci Technol* 2021; 39: 981–989.
15. Zhai W, Zhou W, Nai SML, et al. Characterization of nanoparticle mixed 316 L powder for additive manufacturing. *J Mater Sci Technol* 2020; 47: 162–168.
16. Vasquez E, Giroux P-F, Lomello F, et al. Effect of powder characteristics on production of oxide dispersion strengthened Fe 14Cr steel by laser powder bed fusion. *Powder Technol* 2020; 360: 998–1005.
17. Sehrt JT, Kleszczynski S and Notthoff C. Nanoparticle improved metal materials for additive manufacturing. *Prog Addit Manuf* 2017; 2: 179–191.
18. Goßling M, Rittinghaus S-K, Bharech S, et al. Towards enhancing ODS composites in laser powder bed fusion: investigating the incorporation of laser-generated zirconia nanoparticles in a model iron–chromium alloy. *J Mater Res* 2024; 39: 774–788.
19. Riabov D, Rashidi M, Hryha E, et al. Effect of the powder feedstock on the oxide dispersion strengthening of 316L stainless steel produced by laser powder bed fusion. *Mater Charact* 2020; 169: 110582.
20. Parsons EM and Shaik SZ. Additive manufacturing of aluminum metal matrix composites: mechanical alloying of composite powders and single track consolidation with laser powder bed fusion. *Addit Manuf* 2022; 50: 102450.
21. Wang Y, Wang B, Luo L, et al. Laser-based powder bed fusion of pre-alloyed oxide dispersion strengthened steel containing yttrium. *Addit Manuf* 2022; 58: 103018.
22. Walker JC, Berggreen KM, Jones AR, et al. Fabrication of Fe–Cr–Al oxide dispersion strengthened PM2000 alloy using selective laser melting. *Adv Eng Mater* 2009; 11: 541–546.
23. Minasyan T and Hussainova I. Laser powder-bed fusion of ceramic particulate reinforced aluminum alloys: a review. *Materials* 2022; 15: 1–38.
24. Chen Y, Ren Y, Li K, et al. Laser powder bed fusion of oxidized microscale SiC-particle-reinforced AlSi10Mg matrix composites: microstructure, porosity, and mechanical properties. *Mater Sci Eng: A* 2023; 870: 144860.
25. SALUR E. Structural evolution of mechanically alloyed ODS steel powders during ball milling and subsequent annealing treatment. *Int Adv Res Eng J* 2022; 6: 80–89.
26. Ogbonna OS, Akinlabi SA, Madushele N, et al. Effect of milling time on the morphological evolution of titanium alloy powder. *J Phys: Conf Ser* 2019; 1378: 42066.
27. Streubel R, Wilms MB, Doñate-Buendía C, et al. Depositing laser-generated nanoparticles on powders for additive manufacturing of oxide dispersed strengthened alloy parts via laser metal deposition. *Jpn J Appl Phys* 2018; 57: 040310.
28. Rösler J and Arzt E. A new model-based creep equation for dispersion strengthened materials. *Acta Metall Mater* 1990; 38: 671–683.
29. Zhao K, Duan Z, Liu J, et al. Strengthening mechanisms of 15 vol.% Al2O3 nanoparticles reinforced aluminum matrix nanocomposite fabricated by high energy ball milling and vacuum hot pressing. *Acta Metall Sin* 2022; 35: 915–921.
30. Ferguson JB, Lopez H, Kongshaug D, et al. Revised Orowan strengthening: effective interparticle spacing and strain field considerations. *Metall Mater Trans A* 2012; 43: 2110–2115.
31. Arzt E and Göhring E. Effects of order on dispersion strengthening at high temperatures: a first model. *Scripta Metall Mater* 1993; 28: 843–848.
32. AlMangour B, Grzesiak D, Cheng J, et al. Thermal behavior of the molten pool, microstructural evolution, and tribological performance during selective laser melting of TiC/316L stainless steel nanocomposites: experimental and simulation methods. *J Mater Process Technol* 2018; 257: 288–301.
33. Zhou X, An Z, Shen Z, et al. Particles control in selective laser melting in-situ oxide dispersion strengthened method. *IOP Conf Ser: Mater Sci Eng* 2017; 167: 012048.
34. Autones L, Aubry P, Ribis J, et al. Assessment of ferritic ODS steels obtained by laser additive manufacturing. *Materials* 2023; 16: 9–12.
35. Swamy V, Dubrovinskaya NA and Dubrovinsky LS. High-temperature powder x-ray diffraction of yttria to melting point. *J Mater Res* 1999; 14: 456–459.
36. Lee W-J, Kim E-A, Woo Y-J, et al. Effect of different WC particle shapes on laser-exposed microstructures during the directed energy deposition. *Powder Metall* 2022; 65: 22–30.
37. Zhang P, Pang Y and Yu M. Effects of WC particle types on the microstructures and properties of WC-reinforced Ni60 composite coatings produced by laser cladding. *Metals* 2019; 9: 583.
38. Smith C, Hommer G., Keeler M., etal. Assessing Volumetric Energy Density as a Predictor of Defects in Laser Powder Bed Fusion 316L Stainless Steel. *JOM* 2024.
39. Chia HY, Wang L and Yan W. Influence of oxygen content on melt pool dynamics in metal additive manufacturing: high-

fidelity modeling with experimental validation. *Acta Materialia* 2023; 249: 118824.
40. Horn T, Rock C, Kaoumi D, et al. Laser powder bed fusion additive manufacturing of oxide dispersion strengthened steel using gas atomized reaction synthesis powder. *SSRN J* 2022; 216: 3303–3315.
41. Jia H, Zhou Z and Li S. A new strategy for additive manufacturing ODS steel using Y-containing gas atomized powder. *Mater Charact* 2022; 187: 111876.
42. Zhai W, Zhou W and Nai SML. Effect of interface wettability on additively manufactured metal matrix composites: a case study of 316L-Y2O3 oxide dispersion-strengthened steel. *Metals* 2024; 14: 170.
43. Tan C, Shi Q, Li K, et al. Effect of oxygen content of tantalum powders on the characteristics of parts processed by laser powder bed fusion. *Int J Refract Metals Hard Mater* 2023; 110: 106008.
44. Bauer D, Dietrich K, Walter M, et al. Effect of process gas and powder quality on aluminum alloys processed by laser based powder bed melting process. 2016.
45. Meza A, Macía E, García-Junceda A, et al. Development of new 14 Cr ODS steels by using new oxides formers and B as an inhibitor of the grain growth. *Metals* 2020; 10: 1344.
46. Bidare P, Bitharas I, Ward RM, et al. Fluid and particle dynamics in laser powder bed fusion. *Acta Materialia* 2018; 142: 107–120.
47. Shoji Aota L, Bajaj P, Zschommler Sandim HR, et al. Laser powder-bed fusion as an alloy development tool: parameter selection for in-situ alloying using elemental powders. *Materials* 2020; 13: 10–12.
48. Falk-Windisch H, Svensson JE and Froitzheim J. The effect of temperature on chromium vaporization and oxide scale growth on interconnect steels for solid oxide fuel cells. *J Power Sources* 2015; 287: 25–35.

Appendix C: Study III

Goßling, M., Rittinghaus, S.-K., Radtke, F., Elsayed, A., Barrientos, M. M., Ziesing, U., Becker, L., Kuşoğlu, I.M., Broeckmann, C., Krupp, U., Hariharan, A., Weber, S., Gökce, B. (2025)

Mechanical and Microstructural Effects of ZrO_2 Nanoparticles in Fe20Cr Oxide Dispersion-Strengthened Alloys Processed by Laser Powder Bed Fusion

Advanced Engineering Materials, 2500317

DOI: 10.1002/adem.202500317

ADVANCED ENGINEERING MATERIALS
www.aem-journal.com

Mechanical and Microstructural Effects of ZrO_2 Nanoparticles in Fe20Cr Oxide Dispersion-Strengthened Alloys Processed by Laser Powder Bed Fusion

*Mareen Goßling, Silja-Katharina Rittinghaus, Felix Radtke, Abdelrahman Elsayed, Marina Macias Barrientos, Ulf Ziesing, Louis Becker, Ihsan Murat Kuşoğlu, Christoph Broeckmann, Ulrich Krupp, Avinash Hariharan, Sebastian Weber, and Bilal Gökce**

Integrating oxide nanoparticles (ONPs) into additively manufactured oxide dispersion-strengthened (ODS) steels is challenging due to their tendency for agglomeration and particle loss during processing. This study compares chemically synthesized and laser-generated ZrO_2 ONPs in Fe20Cr alloys produced by laser-based powder bed fusion (PBF-LB/M) using two concentrations (0.1 and 1.0 vol%) under comparable conditions. Oxide nanoparticle (ONP) properties, dispersion, and their impact on microstructure were analyzed via scanning electron microscopy, transmission electron microscopy, electron channeling contrast imaging, and X-ray fluorescence. Mechanical properties are evaluated through hardness, compression, and creep testing at 600 °C. Laser-generated ONPs exhibited narrower size distributions ($D_{90} = 10$ nm) and finer initial dispersion, enabling grain refinement and increased flow stress at 1.0 vol%, increased agglomeration lowered ONP dispersion and increased interparticle distance. Chemically synthesized ONPs show broader distributions and less uniform dispersion, but result in finer grains after heat treatment. Despite coarser grains, the sample with 1.0 vol% laser-generated ONPs shows the lowest creep rate, indicating that a sufficient ONP concentration with limited agglomeration is more critical for creep resistance than grain refinement alone. The results demonstrate that the ONP synthesis route and loading influence the microstructure and ONPs amount-specific strengthening, guiding the design of ODS steels for additive manufacturing.

1. Introduction

Oxide dispersion-strengthened (ODS) steels are known for their exceptional high-temperature strength and creep resistance, making them suitable for use in turbines, boilers, and fusion reactors under extreme thermal and mechanical loads.[1–3] Their performance results primarily from a uniform distribution of nanoscale oxide particles that impede dislocation motion via Orowan looping and grain boundary pinning.[4]

Conventional ODS production methods, such as mechanical alloying and hot isostatic pressing (HIP), are effective but energy-intensive, costly, and challenging to scale.[5–8] Additive manufacturing (AM), particularly laser-based powder bed fusion (PBF-LB/M), offers a promising alternative due to its geometric flexibility and processing efficiency.[9,10] However, integrating oxide nanoparticles (ONPs) into metallic matrices during AM remains challenging. Issues such as agglomeration,

M. Goßling, S.-K. Rittinghaus, B. Gökce
Chair of Materials Science and Additive Manufacturing
University of Wuppertal
42119 Wuppertal, Germany
E-mail: goekce@uni-wuppertal.de

F. Radtke, C. Broeckmann
Chair and Institute for Materials Applications in Mechanical Engineering
RWTH Aachen University
52062 Aachen, Germany

The ORCID identification number(s) for the author(s) of this article can be found under https://doi.org/10.1002/adem.202500317.

DOI: 10.1002/adem.202500317

A. Elsayed, U. Krupp, A. Hariharan
Chair of Materials Engineering of Metals at IEHK Steel Institute
RWTH Aachen University
52072 Aachen, Germany

M. M. Barrientos
Chair of Materials Test Engineering (WPT)
TU Dortmund University
44227 Dortmund, Germany

U. Ziesing, L. Becker, S. Weber
Chair of Materials Technology
Institute for Materials
Ruhr-Universität Bochum
44801 Bochum, Germany

I. M. Kuşoğlu
Technical Chemistry I
Center for Nanointegration Duisburg-Essen (CENIDE)
University of Duisburg
45141 Essen, Germany

inhomogeneous dispersion, and particle loss during melting can impair mechanical performance.[11–15]

Laser-based nanoparticle synthesis offers precise control over particle characteristics. Techniques like laser ablation in liquids (LALs) enable the production of high-purity nanoparticles with narrow size distributions and well-defined morphologies.[16–18] In the context of ODS steels, laser-synthesized ZrO_2 nanoparticles have shown particular promise.[19] Depending on process parameters, monoclinic, tetragonal, or cubic ZrO_2 phases can form, exhibiting different internal stress profiles and transformation behavior.[20,21] For example, tetragonal particles may exhibit residual stresses up to 6 GPa and undergo stress-induced transformations.[20] While production rates and productivity-related energy efficiencies vary, ranging from 0.3 to 25 $g\,h^{-1}$ and 8–83 $Wh\,h\,g^{-1}$, laser-based techniques offer a unique capability to tailor nanoparticle features like size and shape directly during synthesis.[22,23]

ZrO_2 is well-established for dispersoids in ODS steels, valued for its thermal stability and contribution to creep resistance.[24–28] Although chemically synthesized ZrO_2 has been widely used, the potential of laser-generated variants remains underexplored, particularly in alloys processed by AM. Smaller ONPs ($\leq$10 nm) have demonstrated strong strengthening effects,[29] yet their retention during AM is limited by their high reactivity.[30–32] Compared to more common dispersoids like Y_2O_3,[33–36] ZrO_2 also offers advantages in oxidation resistance and phase stability. However, the influence of the synthesis route on their behavior in AM remains insufficiently understood.

Benchmark values for ODS steels vary depending on the alloy composition and processing method. Conventionally processed 14Cr and 18Cr alloys can reach flow stresses of 300–460 MPa at elevated temperatures.[37–39] Widely used examples include PM2000 (Fe-20Cr-5Al), MA956, and 14YWT. However, these systems combine multiple strengthening effects. To isolate the role of the oxide, this study uses a binary Fe20Cr alloy, omitting elements such as Al or Ti, which typically contribute to complex secondary phase formation.[40–42]

Despite broad interest in ZrO_2 as a dispersoid, no quantitative study has yet compared the mechanical performance of AM-processed ODS steels as a function of ZrO_2 synthesis route. Additionally, the effect of nanoparticle concentration remained unclear: While some studies show improvements of mechanical properties at 0.1 vol%,[43] others observe property degradation above 1.0 vol%[44] due to agglomeration or processing defects.

This study tests the hypothesis that laser-generated ZrO_2 nanoparticles, characterized by their narrow size distribution and high phase uniformity, offer more homogeneous dispersion and mechanical performance than chemically synthesized counterparts. To verify this, a controlled comparison is conducted using Fe20Cr samples additivated with each 0.1 or 1.0 vol% of the respective nanoparticle type (**Figure 1**). All samples are produced via PBF-LB/M under comparable processing conditions.

Before processing, ONPs are characterized by scanning electron microscopy (SEM), transmission electron microscopy (TEM), and TEM energy-dispersive X-ray spectroscopy (EDS). Their surface distribution on the powder is analyzed by SEM and SEM-EDS. After PBF-LB/M processing, SEM, SEM electron backscatter diffraction (EBSD), and electron channeling contrast imaging (ECCI) are used to assess microstructure and ONP retention. Mechanical performance is evaluated via hot-hardness, compression, and preliminary creep tests at 600 °C. This temperature corresponds to 0.49 Tm for Fe20Cr (Tm = 1515 °C) and is relevant within the industrial secondary creep regime.[45] This approach allows for a direct, quantifiable comparison of key material properties, considering both the nanoparticle synthesis method and dispersion, while offering insights into the associated strengthening mechanisms.

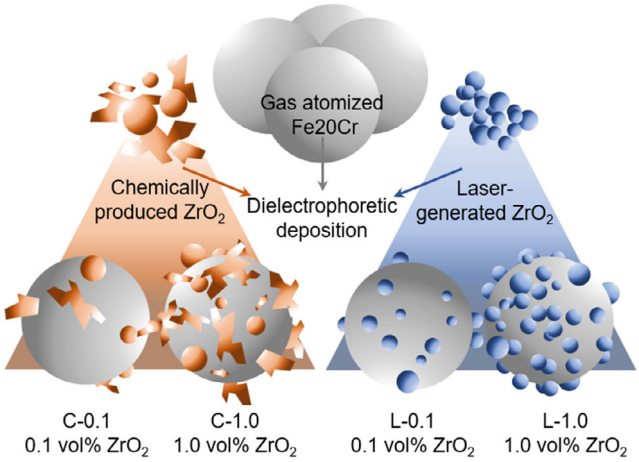

Figure 1. Visualization of ODS powder production routes and produced variants applied in this study.

2. Experimental Section

2.1. Materials

Laser-generated zirconia ONPs were synthesized from Zr700 material (VDM Metals, Altona, Germany) using LAL in deionized (DI) water (Figure 1). The composition of the target material, as characterized by X-ray fluorescence (XRF), revealed a composition of 98.70 wt% Zirconium (Zr), 1.23 wt% Hf, and a residual 0.07 wt% of trace elements. The conventional ONPs were produced using a chemical synthesis process, with a nominal average particle size provided by the supplier (abcr GmbH, Karlsruhe, Germany) of 20 nm and a composition of 99.9 wt% ZrO_2. The following size distribution information was determined: $D_{90} = 1257$ nm, $D_{50} = 26$ nm, and $D_{10} = 11$ nm. The metal base powder had a nominal composition of Fe20Cr (wt%). The initial particle size distribution provided by the manufacturer (Rosswag GmbH, Pfinztal, Germany) ranged from 15 to 45 µm ($D_{10} = 19$ µm, $D_{50} = 29$ µm, and $D_{90} = 43$ µm). XRF analysis confirmed the chemical composition of the Fe20Cr powder as 78.7Fe-21.2Cr (wt%).

2.2. Processing

2.2.1. Nanoparticle Synthesis by LAL

Laser-generated ONPs (L-ONPs) were produced by LAL to ensure precise control over ONP size and distribution.[16,46]

A focused laser beam targets the Zr700 material submerged in DI water, as described in a previous study.[19] For this study, a YLPN-0.5–1 × 5–80 ytterbium pulsed fiber laser (IPG Laser GmbH & Co. KG, Burbach, Germany) operates at 61 W, with a repetition rate of 3 MHz, a wavelength of 1064 nm, and a pulse duration of 1 ns. The laser beam was focused using an f/θ lens with a focal distance of 167 mm, resulting in a laser spot diameter of 40 µm. A spiral scanning pattern facilitated ablation, controlled by a MINISCAN III-14 galvanometric scanning unit (Raylase GmbH, Weßling, Germany). A peristaltic pump (LabV3, Baoding Shenchen Precision Pump Co., Ltd., Baoding, China) ensured a constant flow of DI water at 150 mL min^{-1} during the ablation procedure.

2.2.2. Dielectrophoretic Deposition of Nanoparticle-Additivated Metallic Powders

The dielectrophoretic deposition (DD) process[47,48] was used to produce ZrO_2-additivated Fe20Cr metallic powder by combining either chemically produced (C) or laser-generated ZrO_2 (L) ONPs with Fe20Cr powder. For each powder batch produced via DD, 496 g of Fe20Cr metal powder and 4 g of ZrO_2 ONPs (1.0 vol%; 0.8 wt% ZrO_2) or 499.6 and 0.4 g ZrO_2 ONPs (0.1 vol%; 0.08 wt% ZrO_2) were mixed with 300 mL DI water in a 2000 mL flask (Heidolph Scientific Products GmbH, Schwabach, Germany) as described in ref. [49].

2.2.3. AM by PBF-LB/M

The base and ONP-additivated Fe20Cr powders (Figure 1) were processed using a laboratory-scale PBF-LB/M system (Aconity MINI, Aconity3D GmbH, Germany). A Ytterbium fiber laser ($\lambda = 1064$ nm, spot diameter = 48 µm) was applied under an inert argon atmosphere (Ar 4.6, 1050 mbar), and the samples were produced on a 1.4404 (AISI 316 L) substrate. Processing parameters were optimized in preliminary trials to achieve maximum densification across all powder types. A constant hatch distance of 80 µm, a layer height of 30 µm, and a coater speed of 150 mm s^{-1} were used. Scan strategies included full-area exposure and interlayer rotation of 17°. Laser power (175–220 W) and scan speed (700–800 mm s^{-1}) were adjusted depending on the powder's optical absorption, which is influenced by nanoparticle type and concentration. The selected parameters are detailed in Table S1, Supporting Information. To ensure comparability, all samples were processed under parameter sets, resulting in a relative density of at least 99%, thereby minimizing processing-related variability.

2.2.4. Heat Treatment

After the PBF-LB/M process, selected as-built (AB) samples underwent heat treatment (HT). Solution annealing at 1100 °C for 1 h in an argon atmosphere, followed by air cooling, was chosen to mitigate the effects of rapid solidification and cooling inherent to the PBF-LB/M process.[50,51]

2.3. Analytical Methods

2.3.1. Nanoparticle Size and Chemical Composition Investigated by TEM and SEM

The ONPs were analyzed using TEM and SEM. TEM analysis was performed with a JEM-2200FS (JEOL GmbH, Freising, Germany) and SEM with Apreo S LoVac (Thermo Fisher Scientific GmbH, Schwerte, Germany). The size distribution of the ONPs was determined through image analysis of bright-field TEM and SEM images using ImageJ (Version 1.53 t). Smaller particles (<50 nm) were analyzed using TEM, capturing 594 particles for the L-ONPs. Contrary to the manufacturer's specified size range of ≈20 nm, a significant portion of the chemically produced ONPs (C-ONPs) was found to be in the micrometer range. Due to their unexpectedly large size, 110 particles were additionally characterized by SEM. In contrast, the L-ONPs were analyzed only using TEM images. TEM-EDS line scans were conducted to determine the chemical composition of ONPs. The acceleration voltages used for TEM images in this study were 200 and 5 kV for SEM.

2.3.2. Nanoparticle Crystal Structure Investigated by XRD

X-ray diffraction (XRD) was used to characterize the phase composition of the dry ONPs. This analysis utilized a D8 Advanced system (Bruker Corporation, Billerica, USA), operating in a Bragg–Brentano setup and emitting Cu Kα radiation (wavelength: 1.5406 Å). The XRD pattern was recorded in the 20°–70° 2θ range with a step size of 0.01° and an acquisition time of 5 s per step. The resulting diffractogram was analyzed using the DIFFRAC.EVA software (version 3.0).

2.3.3. Chemical Composition Analysis of Powder and Bulk Samples

The base and ZrO_2 ONP-additivated Fe20Cr powders and PBF-LB/M AB samples were analyzed for elemental composition using X-Ray Flourescence (XRF) with an S8 Tiger instrument (Bruker Corporation, Billerica, USA). The detection depths of ≈350 µm for powders and 45 µm for bulk samples confirm the reliability of XRF measurements for both material states. This instrument, equipped with a rhodium X-ray tube and a beryllium window, was operated at 4 kW. Powder samples (3 g) and cross-sections of AB cubic samples (region of interest (ROI): 8 mm diameter) were measured using the Quant-Express method to determine elemental weight percentages (wt%).

2.3.4. Microstructural Analysis of as- built Samples

Cross sections of AB base and ONP-additivated Fe20Cr samples were prepared metallographically for microstructural characterization. Densities were determined using optical microscopy (LOM, Leica DM-2700) and analyzed with ImageJ (version 1.53t) based on binarized porosity. For EBSD, samples were polished to a 1 µm finish, followed by OPS polishing and ultrasonic cleaning in ethanol for 10 min. EBSD data, collected using a Zeiss Sigma SEM (Carl Zeiss Microscopy GmbH, Jena,

Germany) and a Nordlys Nano detector (Oxford Instruments Co., Ltd., Oxford, UK), were processed with the AZtecCrystal software to generate inverse pole figure maps.

To preserve ONP morphology and evaluate particle retention, high-resolution SEM (Helios G5) imaging was conducted on OPS-polished surfaces. ImageJ (v1.54j) and Python libraries (Pandas, Numpy, Matplotlib) were used to determine ONP size, count, and interparticle distance (IPD); the analysis script is available in the Supplementary Information (Methods S1, Supporting Information). Further characterization was performed using FIB-SEM (Zeiss XB 550 L, Carl Zeiss Microscopy Deutschland GmbH, Oberkochen, Germany) and ECCI at 20 kV and a working distance of 6–7 mm to detect ONPs, including subsurface features. Atomic force microscopy (AFM) (LiteScope, Nenovision, Brno, Czech Republic) was used to validate the ECCI findings and distinguish ONPs from pores or preparation artifacts.

2.4. Mechanical Testing

2.4.1. Hot-Hardness Measurements of Bulk Samples

AB and HT specimens were prepared for hardness testing through standard metallographic grinding and polishing to a 1 µm finish. Vickers hardness was measured using an SRV 4 (Optimol Instruments Prüftechnik GmbH, Munich, Germany) tribometer equipped with a high-temperature heating module. Tests were conducted at room temperature (RT) of 25, 400, and 600 °C under a 9.81 N load (HV1) in an argon atmosphere to prevent oxidation. A heating rate of $10\,K\,s^{-1}$ and a dwell time of 15 min ensured thermal consistency while minimizing microstructural changes. Fifteen indentations were performed at each temperature, and the results were averaged. Indentations were analyzed at room temperature (RT) using optical microscopy.

2.4.2. High-Temperature Compression Testing of PBF-LB/M Samples

Cylindrical samples (5 mm diameter, 14 mm height) were produced via PBF-LB/M using the parameters in Table S1, Supporting Information, and cut from the substrate plate. HT samples were machined to a diameter of 4 mm and a length of 6 mm. Compression tests were performed in a DIL805 dilatometer (TA Instruments, New Castle, USA) under vacuum, with induction heating raising the temperature to 600 °C within 2 min. Samples were compressed at a strain rate of $0.0017\,s^{-1}$ to 25% deformation, followed by 3 min cooling. Actual stress (σ_{true}) and true strain (ε_{true}) were derived from load-displacement data, and the 0.2%-offset method was used to determine the flow stress (σ_f), indicating the onset of plastic deformation.

2.4.3. High-Temperature Creep Testing of PBF-LB/M Samples

To evaluate the long-term mechanical stability of the PBF-LB/M samples, preliminary uniaxial compression creep tests were conducted on selected HT samples. Cylindrical specimens (4 mm diameter, 6 mm height) were machined in the same way as for compression testing. Tests were performed at 600 °C under 50 MPa using a 12 kN creep frame with a three-zone furnace. Temperature was controlled via a thermocouple near the sample center, and axial strain was continuously recorded with an inductive sensor (DK25NLR5, WayCon, Brühl, Germany). Each test ran for 2 weeks.

3. Results and Discussion

3.1. Comparison of NP Chemistry and Morphology

In **Figure 2**, C- and L-ONPs are compared in terms of morphology, shape, and crystal structure and analyzed using SEM (Figure 2a), TEM (Figure 2d), TEM-EDS (Figure 2b,e), and XRD (Figure 2c,f). Quantitative particle size data derived from these methods are summarized in Table S2, Supporting Information.

The C-ONPs (Figure 2a) show a broad size distribution ranging from nanometers to micrometer-sized dendritic structures ($D_{90} = 1257$ nm and $D_{10} = 11$ nm). This inhomogeneity is attributed to uncontrolled nucleation and growth during synthesis, likely influenced by oversaturation and growth-directing anions such as chlorides or hydroxides.[52–54] Although uniform synthesis of particles smaller than 30 nm is reported,[55,56] such consistency was not achieved under the present synthesis route.

In contrast, L-ONPs (Figure 2d) exhibit a narrow size distribution ($D_{90} = 10$ nm and $D_{10} = 3$ nm) and predominantly spherical morphology. The observed uniformity is a direct consequence of the rapid cooling and surface tension effects inherent to LAL.[57–59] No agglomerates or oversized particles were observed in SEM or TEM imaging. For size analysis, more than 500 individual particles were evaluated using high-resolution TEM at varying magnifications. Figure 2d provides an overview and includes representative particle clusters; quantitative measurements were based on isolated ONPs.

Elemental compositions determined by TEM-EDS (Figure 2b,e) confirm Zr and O as primary constituents in both ONP types. L-ONPs (72 at% O, 28 at% Zr; 31 wt% O, and 69 wt% Zr) showed atomic ratios closer to stoichiometric ZrO_2 (67 at% O, 33 at% Zr; 26 wt% O, and 74 wt% Zr), while the C-ONPs (36 at% O, 37 at% Zr; 23 wt% O, and 77 wt% Zr) deviated slightly, possibly due to precursor residues or surface adsorbates.

XRD analysis (Figure 2c,f) revealed phase differences between both nanoparticle types. C-ONPs crystallized in the monoclinic ZrO_2 structure, whereas L-ONPs predominantly exhibited a tetragonal phase, with minor HfO_2 traces originating from the ablation target.

These results highlight substantial differences in particle size, morphology, and phase composition. While more than 500 L-ONPs were statistically analyzed, the irregular shape and clustering of C-ONPs limited the dataset to 30 well-resolved particles, as observed in SEM, supplemented by TEM data for broader representation. Despite this, the data provide a robust basis for evaluating the influence of ONP characteristics on microstructure and mechanical performance, which is explored in the following sections.

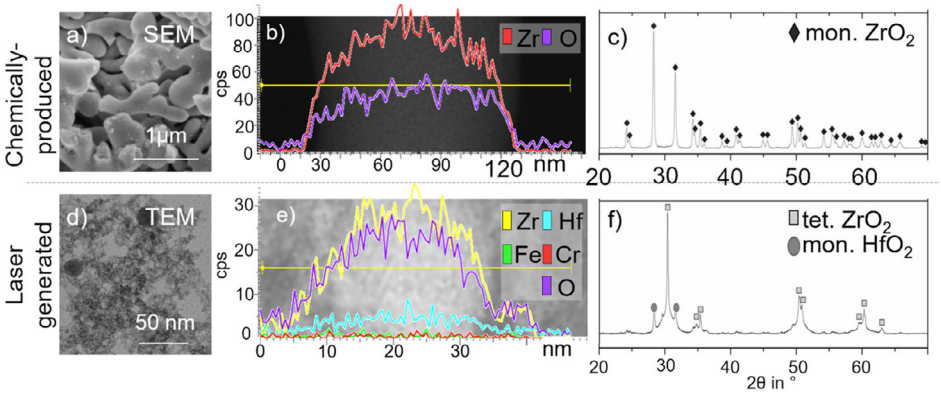

Figure 2. a) SEM, d) TEM, b,e) TEM-EDS line scans, and c,f) XRD of a–c) C-ONPs and d–f) L-ONPs.

3.2. Influence of NP Loading and Type on the NP Distribution on ODS Powders

In **Figure 3**, a SEM and SEM-EDS comparison of the spatial distribution of C-and L-ZrO_2 ONPs on Fe20Cr microparticles is shown. Quantitative elemental data are provided in Table S3, Supporting Information.

C-ONPs (Figure 3j,h) tend to form large agglomerates (≥500 nm), reflecting their irregular, dendritic morphology. In contrast, L-ONPs (Figure 3n,r,t) form smaller, more uniform clusters (<100 nm) with more homogeneous surface coverage. This is attributed to their narrower size distribution and spherical shape. Despite their nanoscale uniformity, even L-ONPs exhibit some agglomeration due to van der Waals forces and surface energy effects.[60] Higher ONP loading increases the frequency and size of agglomerates in both systems. However, at 1.0 vol% addition, L-ONPs create a more continuous and homogeneous coating layer (Figure 3r), while C-ONPs leave visibly uncovered regions at 0.1 vol% (Figure 3j).

While this trend is consistent across the series, the number of visually distinguishable ONPs may appear lower in some laser-modified samples (e.g., Figure 3s,r) compared to chemically modified ones (e.g., Figure 3k,j), despite the higher loading. This is attributed to the small size and dense surface coverage of L-ONPs, which, at sufficient concentration, form a near-continuous nanolayer that appears uniform in SEM imaging. Additionally, these particles' low electrical conductivity and minimal volume reduce contrast in electron imaging, making them less distinguishable than the larger, topographically protruding C-ONPs. We have clarified this optical effect in the manuscript to avoid potential misinterpretation of the particle distribution behavior.

XRF analysis (**Figure 4**) complements SEM-EDS by providing bulk quantification of Zr. EDS, with its shallow penetration depth, is particularly sensitive to compositional variations at the particle surface, where clustered ONPs were visually observed in SEM images (see Figure 3j). Therefore, higher Zr readings in chemically modified powders may partly reflect the presence of loosely adhered ONP clusters on the powder surface. Conversely, L-ONPs yield lower but more uniform Zr signals in both EDS and XRF, supporting the visual impression of even distribution. It is worth noting that EDS measurements on powder surfaces are influenced by surface roughness, particle curvature, and potential charging effects, which can contribute to signal variability and quantification uncertainty.[61]

Theoretical Zr contents for 0.1 and 1.0 vol% additions are ≈0.06 and 0.6 wt%, respectively. However, both EDS and XRF measurements show sublinear increases with higher ONP loading. This deviation indicates a saturation limit for ONP adherence to the powder surface, with excess particles likely detaching during mixing or handling. These findings highlight the more homogeneous distribution characteristics of L-ONPs and establish a compositional basis for evaluating their retention and mechanical impact, which will be discussed in the following sections.

3.3. Influence of ODS Powders on the Microstructure of PBF-LB/M Processed Parts

In the cross-sectional images (**Figure 5**), it can be seen that the addition of ONPs alters both porosity and pore morphology in Fe20Cr samples. The non-additivated reference (Figure 5a) exhibits the highest density (99.98%) with isolated spherical pores, typically associated with gas entrapment. In contrast, samples with 1.0 vol% ONPs exhibit a density reduction down to 99.04% and irregular dark features. Although similar features have been described as slag inclusions in Al-containing steels,[40–42] no reactive alloying elements or internal structures were detected here. Thus, these defects are attributed to incomplete ONP incorporation and were included in the densification analysis as pore-like features.

While the absolute change in density is small (e.g., 99.98–99.04%), such differences may significantly impact creep performance. Previous studies on AM 316 L have shown that even a porosity of ≈0.1% can reduce creep life due to cavity nucleation at defects.[62]

HT at 1100 °C for 1 h did not change porosity but significantly affected the microstructure. The EBSD images (**Figure 6**) illustrate the grain structures of the studied samples. The reference material (Figure 6i,j) exhibits the expected ferritic grain structure typical of additively manufactured steels, with grain sizes (GSs) of no clear preferred direction and a size of 17 µm in the AB and 10 µm in the HT condition.

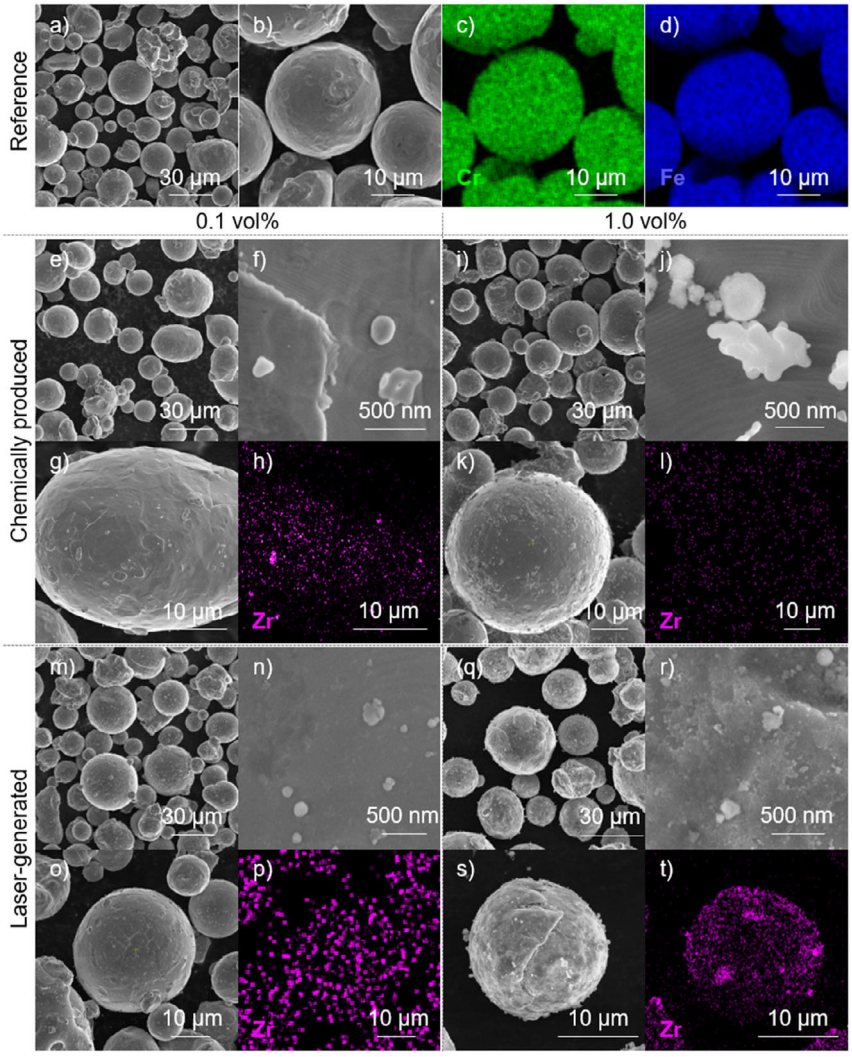

Figure 3. a,b,e–g,i–k,m–o,q–s) SEM imaging and c,d,h,l,p,t) SEM-EDS analysis of non-additivated Fe20Cr powder (upper section), chemically produced (middle section), and laser-generated (lower section) ZrO_2 NP distribution on Fe20Cr microparticles with 0.1 vol% (left) and 1.0 vol% (right) after feedstock additivation.

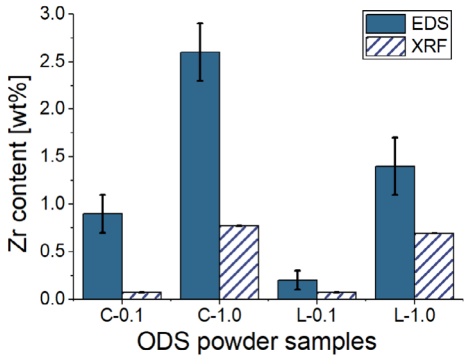

Figure 4. Zr content in the ODS powder as determined by EDS and XRF.

The rapid temperature fluctuations in the PBF process may lead to interrupted recrystallization, promoting a finer grain structure rather than grain coarsening. The nanoparticles act as grain growth barriers (Zener pinning), stabilizing this microstructure and favoring grain refinement. The recrystallization process during HT is initiated by heating the ferrite to a specific temperature range (<700–1300 °C[63–65]), where the thermal energy provided allows grains to overcome nanoparticle pinning. At higher temperatures, grains gain sufficient energy to coarsen by bypassing the particles, leading to grain growth and forming a new, more homogeneous grain structure.[66]

Samples with L-ONPs (Figure 6c,d) initially (AB) exhibit a visibly higher number of very fine grains than those with C-ONPs, yet no measurable anisotropy is observed. In contrast, the heat-treated L-0.1/1.0 (Figure 6g,h) samples are the only ones to show distinct anisotropy, with grains aligned along the build direction (BD) and aspect ratios (vertical mean linear intercept (MLI)/horizontal MLI) of 2.03 ± 1.46 (L-0.1) and 2.80 ± 2.25 (L-1.0), respectively. In contrast, samples with C-ONPs show no preferred grain elongation, neither in AB (Figure 6a,b) nor in HT (Figure 6e,f) condition, with aspect ratios close to 1.0.

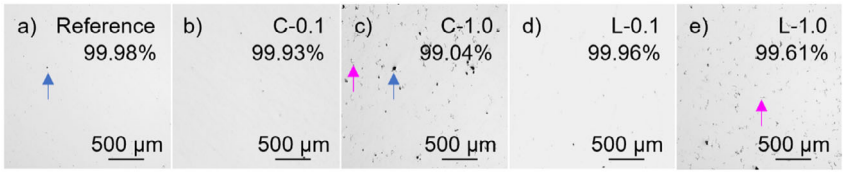

Figure 5. LOM images and part densities of PBF-LB/M samples in AB condition. Cross-sections show samples processed with a) no ONPs (reference), chemically synthesized ONPs at b) 0.1 vol% and c) 1.0 vol%, as well as d) laser-generated ONPs at 0.1 vol%, and e) 1.0 vol% loading.

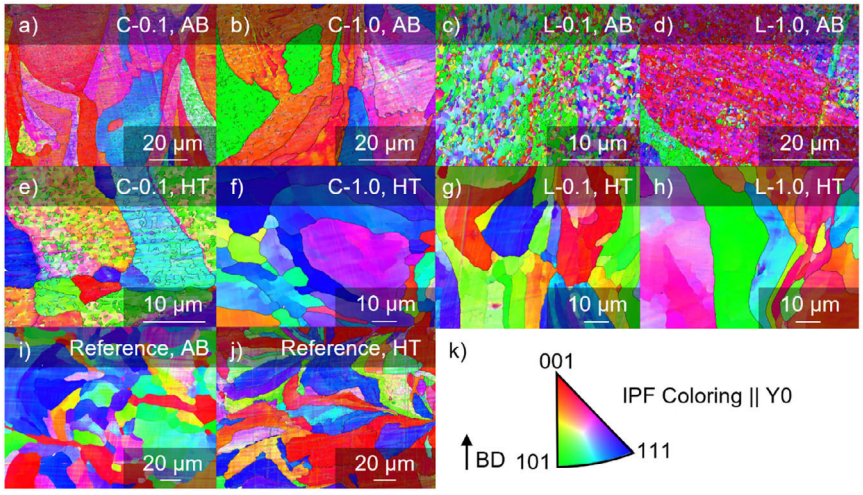

Figure 6. EBSD results of AB and HT ODS steel samples with a–j) representing IPF color maps according to the key depicted and BD in (k). C and L indicate samples with chemically (C) and laser-generated (L) ONP, respectively, while 0.1 and 1.0 represent the ONP volume fractions. The reference samples ((i) and (j)) highlight grain structures without ONPs in the AB and HT conditions.

The diagram in **Figure 7** quantifies these trends and confirms that ONP type and distribution influence GS evolution. The pronounced grain refinement observed in the AB condition for L-ONPs (GS ≈1 µm) is attributed to their small size and uniform dispersion, which enables effective grain boundary pinning during the cyclic thermal exposure of the PBF process. In contrast, the GS of C-0.1 decreases from 5 µm (AB) to 1 µm after HT, representing a 72% reduction. This may result from particle-stimulated nucleation at larger ONPs, due to their higher lattice mismatch and stronger interface energy. However, whether true nucleation or incomplete recrystallization, the underlying mechanism is not conclusively identified and may depend strongly on local processing and HT conditions. Both systems exhibit reduced refinement effects at higher ONP loadings (1.0 vol%), with GSs increasing to 16 µm for L-0.1 and 25 µm for L-1.0 after HT, likely due to particle agglomeration and coarsening.

While the EBSD data confirm general trends, the limited scan area may not capture all microstructural variability, particularly after HT. Additionally, exploring a broader temperature and duration range for HT would be valuable for optimizing and better understanding temperature-dependent changes in microstructural and mechanical alloy properties.

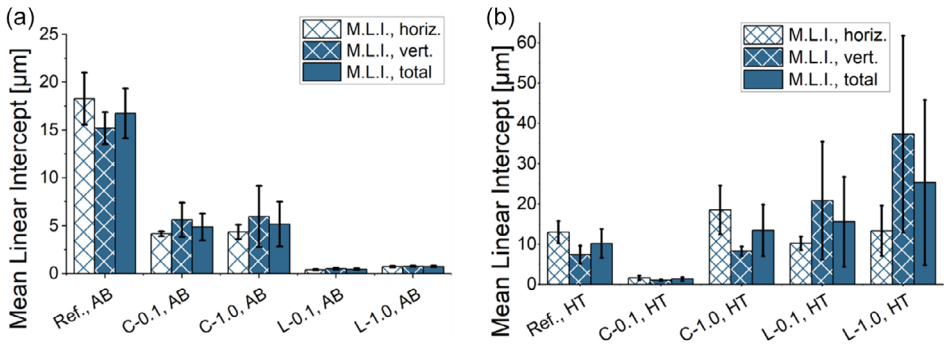

Figure 7. GSs determined by line intersection on the EBSD images in horizontal, vertical alignment to the build direction resulting in mean GS (total) calculated via MLI of the PBF-LB/M samples in a) AB and b) HT conditions.

3.4. Evaluation of NP Size and Distribution in PBF-LB/M Processed Parts

In XRF measurements (**Figure 8**), a marked reduction in Zr content is observed in as-built parts compared to the powder feedstocks, indicating nanoparticle loss during PBF-LB/M. The complete dataset is available in Table S4, Supporting Information. This loss, attributed to evaporation or spatter-induced ejection under high-temperature laser exposure, is more pronounced at higher ONP loadings. Quantitatively, C-ONPs exhibit 30% loss at 0.1 vol% and 25% at 1.0 vol%, whereas L-ONPs show 20% loss at 0.1 vol% and 30% at 1.0 vol%.

This loss can be attributed to particle evaporation or ejection during laser exposure. The elevated thermal input and interaction with process gas flows promote spatter and vaporization, especially for particles loosely bound at the surface. L-ONPs, although initially more homogenous dispersed, and smaller in size, become increasingly prone to loss at higher ONP loadings. This is explained by their tendency to coalesce during heating, which reduces surface area and weakens van der Waals interactions with the surrounding matrix. As a result, adhesion is reduced, and particles are more readily displaced or vaporized during melting.

At lower loadings, L-ONPs benefit from their high surface-to-volume ratio and stronger van der Waals forces, which promote higher adherence to the melt pool and result in lower loss rates compared to the bigger chemically synthesized counterparts. However, at higher ONP loadings, this advantage is negated by increased coalescence and a higher statistical probability of surface exposure to the laser, both of which amplify the risk of ejection or vaporization.

In contrast, C-ONPs—despite their larger size and less uniform distribution—are less prone to thermal coalescence, which may partially explain their more consistent retention behavior across different ONP loadings.

It should be noted that while matrix elements such as chromium are also subject to partial evaporation under PBF-LB/M conditions, they remain primarily embedded within the melt pool and benefit from rapid re-solidification. ONPs, particularly those at or near the surface or loosely present within the powder bed, experience weaker thermal coupling and are more vulnerable to localized overheating, recoil pressure, and gas flow-induced displacement. This makes their retention behavior fundamentally different and more prone to loss, despite the high thermal stability of ZrO_2 itself.

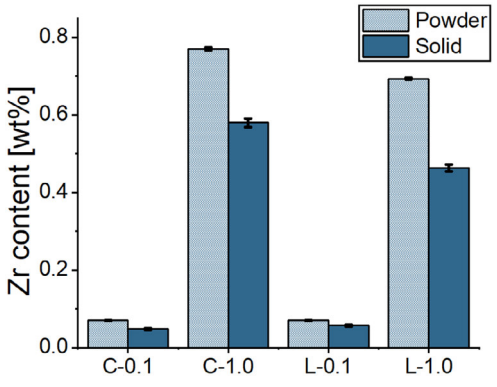

Figure 8. Measured Zr amounts (wt.-%) in the ODS powder feedstocks and AB PBF-LB/M ODS parts via XRF technique.

While XRF provides bulk data, its limited spatial resolution necessitates the use of complementary nanoscale techniques. ECCI imaging (**Figure 9**) reveals ONPs as nanoscale black dots (exemplary dashed with white circles), which AFM confirms as topographical protrusions with a height of ≈0.5–1 nm and a lateral size of 20–40 nm (Figure 9f–i), consistent with the expected ONP dimensions (**Figure 10**).

The yellow arrows indicate ONPs aligned along small-angle grain boundaries, supporting their role as pinning agents stabilizing the microstructure. Magenta arrows mark blurred ONPs beneath the surface, indicating sub-surface disruptions. Red arrows in Figure 9d and the zoomed view in Figure 9e highlight line-like features observed in the L-1.0 sample. Based on their morphology and location, they are interpreted as dislocation lines, in line with previous observations in similar ODS steels.[67–69] Their proximity to ONPs suggests a possible interaction, such as dislocation pinning or stress-induced formation from sample preparation. One potential cause may be internal stresses associated with the tetragonal-to-monoclinic phase transformation of L-ONPs during cooling (970–750 °C).[70] Further high-resolution investigations, such as TEM or HR-EBSD, would be required to confirm the exact mechanism.

The total number of ONPs detectable via ECCI varies significantly: L-1.0 yielded only 107 particles due to either image resolution or agglomeration-induced detectability loss. Representative high-magnification ECCI images used for particle size analysis are provided in Figure S1, Supporting Information, to illustrate the resolution and measurement basis. The ONP size distribution in bulk samples (Figure 10) shows that L-1.0 contains the largest ONPs, indicating coalescence. In contrast, C-0.1 exhibits the most petite average ONP sizes and the most uniform distribution.

SEM imaging (**Figure 11**) complements ECCI by enabling broader field analysis. ONPs appear as bright dots; however, particle sizes are generally overestimated due to charging and potential artifacts from sample preparation. However, larger particle sizes observed in SEM may indicate agglomeration behavior. For example, in Figure 11d, a spherical L-ONP with an approximate size of 70 nm can be observed, suggesting that ONPs may have undergone partial melting during the PBF-LB/M process, resulting in larger spherical volumes upon solidification. Furthermore, agglomerated ONPs are frequently observed in high-loading samples, forming dendritic structures (Figure 11i,j). In C-ONPs, larger particles retain their shape. They are found at the edges of these structures (Figure 11i), whereas L-ONPs (Figure 11j) appear to have melted together, contributing to the dendritic formation.

The IPD analysis (Figure 11k, and Table S5, Supporting Information) further clarifies the dispersion behavior of ONPs in the PBF-LB/M samples. Notably, the L-1.0 sample—despite its high ONP loading—exhibits the largest average IPD (734 ± 475 nm). This contradicts the expected trend of decreasing IPD with increasing ONP concentration, suggesting a saturation threshold at which additional particles no longer improve dispersion but promote agglomeration and localized growth.

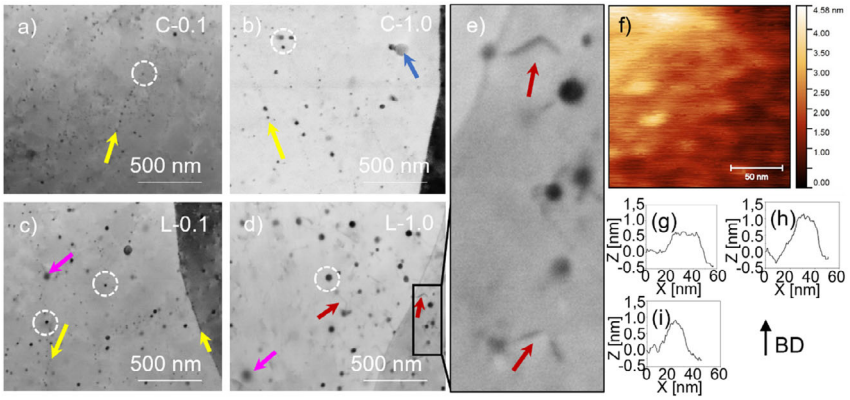

Figure 9. ECCI images of additivated solid samples with a,c) 0.1 vol% and b,d,e) 1.0 vol% a,b) C-ONPs and c–e) L-ONPs, exemplarily marked by the white dashed circles. Exemplary ONPs under the surface are shown with magenta arrows; dislocations are indicated with red arrows, and pores with blue arrows. f) AFM analyses with g–i) several measurements revealed elevations in the *Z*-direction.

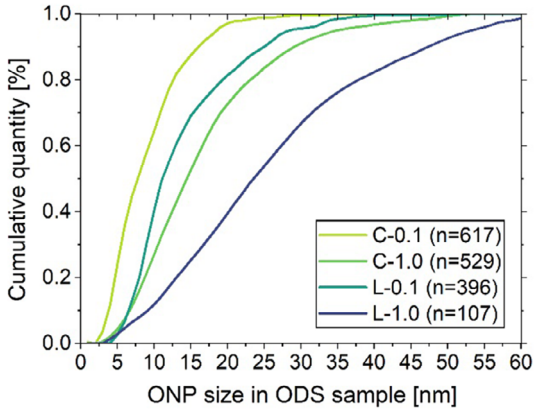

Figure 10. ONP size in PBF-LB/M processed samples in AB condition optically analyzed by ECCI images.

The reduced number of discrete particles in L-1.0 aligns with ECCI and SEM observations of particle clustering and coalescence.

In contrast, the low-loading L-sample (L-0.1) shows a lower average IPD, consistent with more effective dispersion and a higher number of individually detectable particles. For C-ONPs, the difference between C-0.1 (520 ± 348 nm) and C-1.0 (445 ± 309 nm) is less pronounced. Interestingly, C-1.0 exhibits a slightly smaller average IPD than C-0.1, despite its higher ONP loading. This is counterintuitive given that the C-0.1 sample contains the smallest ONPs (see Figure 10), which, under ideal dispersion, would be expected to produce the lowest IPD. One possible explanation lies in a less uniform particle distribution in C-0.1 or sampling limitations in the image-based evaluation. However, it may also reflect the lower tendency of C-ONPs to agglomerate under thermal exposure, as discussed in the XRF section. Unlike their laser-generated counterparts, the larger and structurally stable monoclinic ONPs exhibit reduced coalescence and stronger resistance to melt pool dynamics, potentially resulting in more consistent particle spacing even at higher loadings.

In summary, although L-ONPs exhibit a more homogenous initial dispersion and chemical purity, their tendency to agglomerate at higher ONP loadings reduces their effective particle number and dispersion quality postprocessing. This observation is crucial for evaluating the hypothesis that L-ONPs, if retained in a small, well-dispersed form, enhance strengthening efficiency through the Orowan mechanism.

3.5. Influence of NP Size and Distribution on Mechanical Properties of PBF-LB/M Processed Parts

The mechanical performance of PBF-LB/M-processed Fe20Cr samples was evaluated through hardness testing (RT, 400 °C, 600 °C) and compression tests at 600 °C, supported by creep experiments. The selected temperature of 600 °C corresponds to 0.49 Tm for Fe20Cr (Tm = 1515 °C) and lies within the secondary creep regime,[45] ensuring relevance for high-temperature applications.

In the AB condition (**Figure 12**a), the reference sample exhibited the highest hardness. All ONP-additivated samples showed slightly lower values, with L-1.0 (AB) marginally lower than the chemically modified variants. HT at 1100 °C for 1 h (Figure 12b) reduced the hardness across all samples due to recrystallization and grain growth (see Figure 6 and 7).

However, the extent of degradation varied depending on ONP type and loading. L-ONPs at 1.0 vol% (L-1.0, HT) achieved the highest hardness values (171 HV1 at RT and 168 HV1 at 400 °C), followed by C-1.0 (168 HV1 at RT and 156 HV1 at 400 °C), while 0.1 vol% ONP samples showed only minor improvements over the reference (150 HV1 at RT and 140 HV1 at 400 °C). The reduced variability observed in L-1.0 suggests a more homogeneous strengthening effect, consistent with homogeneous dispersion and finer ONP size. For comparison, in **Table 1**, the results of hardness measurements of HT samples at RT and 400 °C are shown.

Compression testing at 600 °C (Figure 12c) confirmed these trends and highlighted the influence of GS and IPD on the flow stress. C-0.1 exhibited the highest strength with an increase of 21% compared to the reference (252 ± 7 MPa), followed by

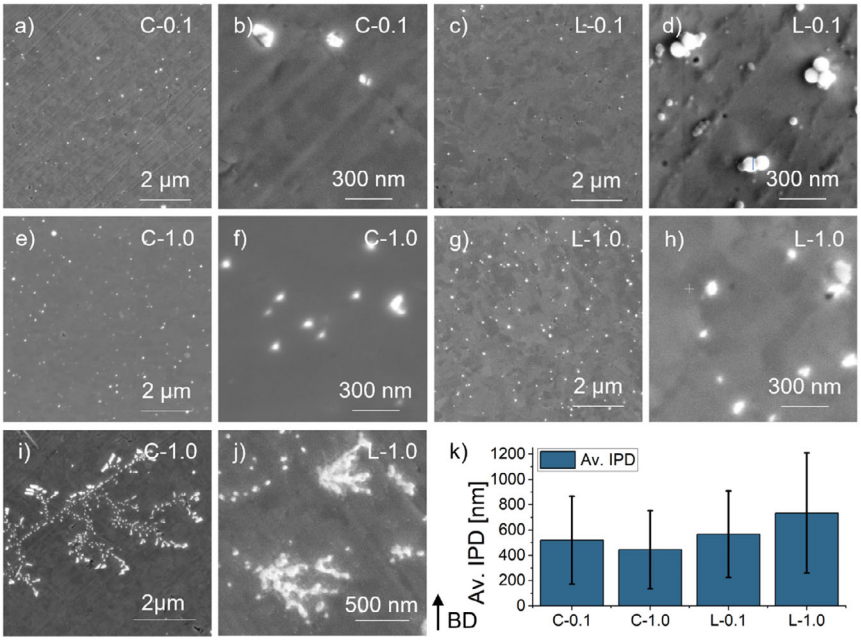

Figure 11. SEM images of additivated solid samples with a–d) 0.1 vol% and e–j) 1.0 vol% a,b,e,f,i) C-ONPs and c,d,g,h,j) L-ONPs in different magnifications. The optical analyzed IPD of the ODS samples is shown in diagram (k) with the values in Table S5, Supporting Information.

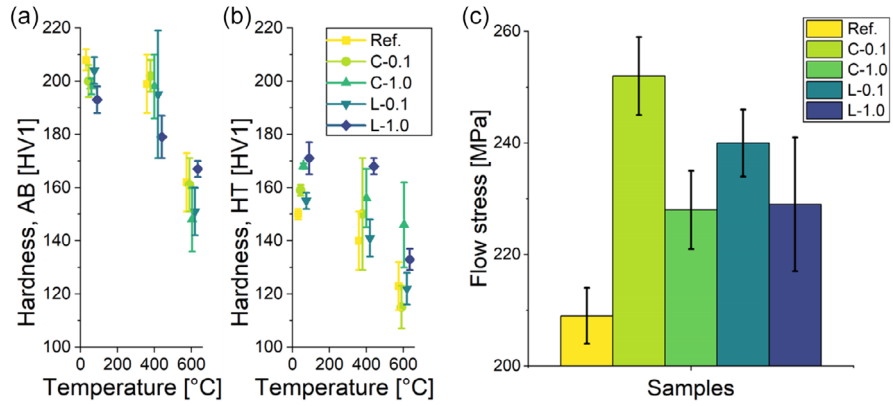

Figure 12. Hardness measured at room and elevated temperature on a) AB and b) HT parts, flow stress as a result of compression tests on c) HT parts at 600 °C.

Table 1. Vickers hardness of as-built parts at RT and 400 °C in HT condition.

	Vickers Hardness at RT	SD	Vickers Hardness at 400 °C	SD
	HV1	HV1	HV1	HV1
Ref, HT	150	2	140	11
L-0.1, HT	155	3	141	7
L-1.0, HT	171	6	168	3
C-0.1, HT	159	2	150	21
C-1.0, HT	168	1	156	11

15% for L-0.1 (240 ± 6 MPa), and ≈10% for C-1.0 (228 ± 7 MPa) and L-1.0 (229 ± 12 MPa). The high flow stress of C-0.1 correlates with its refined GS (1 ± 1 µm) and moderate IPD (520 ± 348 nm). In contrast, L-1.0, despite containing smaller ONPs, showed a lower flow stress due to a coarser GS (25 ± 21 µm) and the highest IPD (734 ± 475 nm). These findings indicate that GS primarily governs flow stress in short-term plastic deformation, while IPD plays a secondary role. ONP size alone is not decisive unless supported by practical grain refinement and dispersion.

In contrast, creep deformation at 600 °C and 50 MPa (**Figure 13**) was more strongly influenced by the ONP type

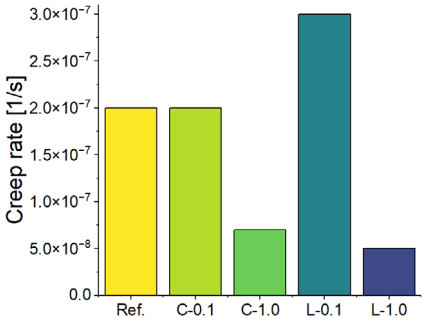

Figure 13. Results of creep tests performed at 600 °C under 50 MPa using a 12 kN creep frame (HT condition).

and ONP loading. The L-1.0 sample, characterized by the highest aspect ratio (2.80 ± 2.25), demonstrated the lowest steady-state creep rate ($5.0 \times 10^{-8}\,s^{-1}$), followed by C-1.0 ($7.0 \times 10^{-8}\,s^{-1}$), both significantly lower than the reference ($2.0 \times 10^{-7}\,s^{-1}$). The lowest result for L-1.0 in comparison to the other samples was confirmed by a repeat test, supporting the reliability of the observed lower creep rate. Although minor density variations might impact creep performance, as discussed earlier, such an effect was not prominently observed here.

C-0.1, despite achieving the highest flow stress, showed inferior creep resistance compared to higher ONP-loaded samples. This suggests the benefits of grain refinement diminish during prolonged thermal exposure. The notably poorer creep performance of L-0.1 ($3.0 \times 10^{-7}\,s^{-1}$) correlates with increased nanoparticle agglomeration, indicated by larger ONP sizes comparable to C-1.0 and a relatively high aspect ratio (2.03 ± 1.46). Such agglomerates likely reduce the efficiency of individual nanoparticles for Orowan-type dislocation pinning and introduce local structural imperfections, which may explain the observed differences.

To evaluate the potential influence of Zr content on the mechanical performance, the actual Zr concentrations in the printed parts were determined via XRF (Figure 8): L-0.1 = 0.057 wt%, C-0.1 = 0.048 wt%, L-1.0 = 0.463 wt%, and C-1.0 = 0.580 wt%. While C-1.0 exhibits the highest overall Zr content, the higher creep resistance and hot-hardness observed for L-1.0 suggest that total Zr content alone is not the dominant factor. Instead, particle size, dispersion quality (IPD), and microstructural stability play a more decisive role.

The mechanical response of the investigated ODS steels is thus governed by ONP load-specific mechanisms: GS and IPD dictate performance in short-term loading. At the same time, thermally stable dispersoids control long-term behavior. These findings confirm that L-ZrO_2 ONPs, when well-dispersed, are particularly effective in improving high-temperature creep resistance. However, their tendency to agglomerate at higher concentrations can lead to increased IPD and reduced strengthening efficiency.

It is important to note that the creep tests presented here were exploratory and based on single measurements per condition. While trends are observed, further replicates are needed to establish statistical robustness. Moreover, the selected creep temperature was chosen for consistency with compression testing and does not cover the full range of application-relevant conditions, which may involve higher temperatures and stresses.

Future studies should include post-mortem high-resolution analysis (e.g., TEM and HR-EBSD) to investigate dislocation–particle interactions and directly validate proposed mechanisms such as Orowan looping or particle pinning. Complementary chemical analysis may further elucidate the stability of ONP, potential interfacial reactions, and phase transformations under thermal exposure. These insights are crucial for optimizing ONP type, ONP loading, and processing parameters to achieve higher long-term performance in ODS steels.

4. Conclusions

This study demonstrates that the synthesis route and concentration of ZrO_2 nanoparticles significantly influence their distribution, microstructural integration, and strengthening mechanisms in PBF-LB/M-processed Fe20Cr ODS steels. L-ONPs, characterized by a narrow size distribution ($D_{90} = 10$ nm) and tetragonal phase composition, showed more homogeneous initial dispersion than chemically synthesized, polydisperse monoclinic ONPs ($D_{90} = 1257$ nm). However, at higher ONP loadings (1.0 vol%), L-ONPs exhibited coalescence and agglomeration, leading to an increased IPD (734 ± 475 nm) and reduced retention, as evidenced by XRF and ECCI.

The mechanical response depends on distinct microstructural factors. Compression strength at 600 °C correlated primarily with GS, with C-0.1 achieving the highest flow stress (252 ± 7 MPa) due to a refined GS (1 ± 1 µm) and moderate IPD (520 ± 348 nm). In contrast, creep resistance correlated more strongly with ONP loading, GS aspect ratio, and agglomeration tendencies rather than grain refinement alone. Specifically, the lowest creep rate ($5.0 \times 10^{-8}\,s^{-1}$ for L-1.0) corresponded to high ONP loading combined with elongated ONPs and minimal agglomeration, promoting effective Orowan pinning.

These results partially confirm the hypothesis that L-ONPs, characterized by narrow size distributions and high uniformity, can positively influence creep resistance. However, contrary to initial expectations, the advantage of L-ONPs is not consistent across all loadings. While L-1.0 exhibited superior creep performance, the unexpectedly poor creep resistance of L-0.1 indicates significant open questions regarding the impact of nanoparticle distribution and agglomeration. Such agglomeration appears to substantially reduce effective nanoparticle-based strengthening mechanisms, overshadowing potential advantages derived from their initial uniformity. In contrast, C-ONPs showed stable microstructural refinement and strengthening at lower concentrations.

Overall, the interplay between nanoparticle type, size, and dispersion determines the dominant strengthening mechanism. For short-term performance, grain refinement—achieved through small and well-distributed ONPs—is most effective. In contrast, long-term creep resistance correlates with a higher ONP loading and a homogeneous, finely dispersed distribution with minimal agglomeration. These insights provide a foundation for tailoring ONP synthesis and processing strategies to application-specific mechanical demands in ODS alloys.

Supporting Information

Supporting Information is available from the Wiley Online Library or from the author.

Acknowledgements

The authors thank Hamed Shokri and Michael Blüm for their preliminary work on the compression tests, as well as Jan Hendrik Vehrs for his contributions during his master's thesis. Thanks to Tobias Bochman and Matthias Epple for conducting the SEM/EDS (Faculty for Chemistry at University Duisburg Essen) analysis of the powder samples and Jonathan Edling's support in performing the hot-hardness measurements. Daniel Behrens is acknowledged for his support of the PBF-LB/M processing, and Johanna Dell'Anno is recognized for supporting the production of the laser-generated ONPs. The authors also thank Johannes Sailer for assisting with the evaluation of the compression tests. Salvatore Scrofani is credited for ECCI imaging, with additional contributions from Jan Goldberg and Kai Donnerbauer for in situ AFM. Parts of the text were linguistically refined with the assistance of OpenAI GPT-4. This research was conducted as part of the German Research Foundation (DFG) Priority Program 2122, "Materials for Additive Manufacturing" (SPP 2122, project number 493889809, GO 2566/13-1, and XU 121/20-1). Additionally, B. Gökce acknowledges support from the DFG Heisenberg Program, project GO 2566/10-1 (445127149). Marina Macias Barrientos thanks the DFG and the Ministerium für Kultur und Wissenschaft des Landes Nordrhein-Westfalen (MKW NRW, Ministry of Culture and Science of North Rhine-Westphalia) for their financial support within the Major Research Instrumentation Program (Focused Ion Beam Zeiss XB550 L (FIB-SEM, 386509496) and In-situ Atomic Force Microscope (445052562)).

Open Access funding enabled and organized by Projekt DEAL.

Conflict of Interest

The authors declare no conflict of interest.

Author Contributions

Mareen Goßling: conceptualization (equal); investigation (lead); validation (lead); visualization (lead); and writing—original draft (lead). **Silja-Katharina Rittinghaus**: conceptualization (equal); writing—original draft (supporting). **Felix Radtke**: investigation (supporting) and writing—original draft (supporting). **Abdelrahman Elsayed**: investigation: (supporting) and writing—original draft: (supporting). **Marina Macias Barrientos**: investigation (supporting) and writing—original draft (supporting). **Ulf Ziesing**: investigation (supporting) and writing—original draft (supporting). **Louis Becker**: investigation (supporting); validation (supporting); and writing—review and editing (supporting). **Ihsan Murat Kuşoğlu**: investigation (supporting) and writing—original draft (supporting). **Christoph Broeckmann**: funding acquisition (supporting) and supervision (supporting). **Ulrich Krupp**: funding acquisition (supporting) and supervision (supporting). **Avinash Hariharan**: writing—review and editing (supporting). **Sebastian Weber**: funding acquisition (supporting); validation (supporting); and writing—review and editing (supporting). **Bilal Gökce**: conceptualization (equal); funding acquisition (lead); and writing—review and editing (supporting).

Data Availability Statement

The data that support the findings of this study are available from the corresponding author upon reasonable request.

Keywords

high temperature, heat treatment strength, laser ablation in liquids, laser powder bed fusion, nanoparticles

Received: January 31, 2025
Revised: April 10, 2025
Published online:

[1] S. Eswarappa Prameela, T. M. Pollock, D. Raabe, M. A. Meyers, A. Aitkaliyeva, K.-L. Chintersingh, Z. C. Cordero, L. Graham-Brady, *Nat. Rev. Mater.* **2023**, *8*, 81.
[2] Q. Li, C. M. Parish, K. A. Powers, M. K. Miller, *J. Nucl. Mater.* **2014**, *445*, 165.
[3] A. Wasilkowska, M. Bartsch, U. Messerschmidt, R. Herzog, A. Czyrska-Filemonowicz, *J. Mater. Process. Technol.* **2003**, *133*, 218.
[4] G. Gottstein, *Materialwissenschaft und Werkstofftechnik: Physikalische Grundlagen*, 4th ed., Springer Berlin Heidelberg, Berlin, Heidelberg **2014**, pp. 219–319.
[5] S. K. Karak, T. Chudoba, Z. Witczak, W. Lojkowski, I. Manna, *Mater. Sci. Eng. A* **2011**, *528*, 7475.
[6] C. Capdevila, M. K. Miller, K. F. Russell, J. Chao, J. L. González-Carrasco, *Mater. Sci. Eng. A* **2008**, *490*, 277.
[7] I. Hilger, X. Boulnat, J. Hoffmann, C. Testani, F. Bergner, Y. Carlan, F. de Ferraro, A. Ulbricht, *J. Nucl. Mater.* **2016**, *472*, 206.
[8] S. Chung, B. Lee, S. Y. Lee, C. Do, H. J. Ryu, *J. Mater. Sci. Technol.* **2021**, *85*, 62.
[9] Y. Tang, S. Yang, Y. F. Zhao, in *Handbook of Sustainability in Additive Manufacturing* (Eds: S. S. Muthu, M. M. Savalani), Springer Singapore, Singapore **2016**, pp. 101–144.
[10] W. Liu, X. Liu, Y. Liu, J. Wang, S. Evans, M. Yang, *Sustainability* **2023**, *15*, 3827.
[11] D. Gu, X. Shi, R. Poprawe, D. L. Bourell, R. Setchi, J. Zhu, *Science* **2021**, *372*, eabg1487.
[12] M. A. Meyers, K. K. Chawla, in *Mechanical Behavior of Materials*, Cambridge University Press, Cambridge **2012**.
[13] D. Pilone, G. Pulci, L. Paglia, A. Mondal, F. Marra, F. Felli, A. Brotzu, *Metals* **2020**, *10*, 1457.
[14] H. Tang, X. Chen, M. Chen, L. Zuo, B. Hou, Z. Wang, *Mater. Sci. Eng. A* **2014**, *609*, 293.
[15] J. H. Schneibel, M. Heilmaier, W. Blum, G. Hasemann, T. Shanmugasundaram, *Acta Mater.* **2011**, *59*, 1300.
[16] D. Zhang, B. Gökce, S. Barcikowski, *Chem. Rev.* **2017**, *117*, 3990.
[17] A. Subhan, A.-H. I. Mourad, Y. Al-Douri, *Nanomaterials* **2022**, *12*, 8.
[18] S. Z. Mat Isa, R. Zainon, M. Tamal, *Materials* **2022**, *15*, 3.
[19] M. Goßling, S.-K. Rittinghaus, S. Bharech, Y. Yang, M. B. Wilms, L. Becker, S. Weber, B.-X. Xu, B. Gökce, *J. Mater. Res.* **2024**, *39*, 774.
[20] M.-H. Tsai, S.-Y. Chen, P. Shen, *J. Chem. Phys.* **2005**, *122*, 204708.
[21] D. Tan, Y. Teng, Y. Liu, Y. Zhuang, J. Qiu, *Chem. Lett.* **2009**, *38*, 1102.
[22] N. Bärsch, J. Jakobi, S. Weiler, S. Barcikowski, *Nanotechnology* **2009**, *20*, 445603.
[23] A. I. Kostyukov, A. A. Nashivochnikov, V. Snytnikov, M. I. Rakhmanova, V. N. Snytnikov, *Quantum Electron.* **2022**, *52*, 149.
[24] A. Adamski, P. Jakubus, Z. Sojka, *Nukleonika* **2006**, *51*, S27.
[25] C. Wang, *Ph.D. Thesis*, University of Stuttgart, Max Planck Institute for Metals Research, Stuttgart, Germany **2006**, pp. 5–6.
[26] Y. Kawasaki, Y. Ikeda, T. Kobayashi, H. Sumiyoshi, *ISIJ Int.* **1996**, *36*, 1208.
[27] N. Sekido, A. Hoshino, M. Fukuzaki, Y. Yamabe-Mitarai, T. Maruko, *Mater. Sci. Eng. A* **2011**, *528*, 8451.
[28] M. Silalahi, B. Bandriyana, S. Ahda, B. Sugeng, A. Dimyati, *J. Phys.: Conf. Ser.* **2020**, *1436*, 12055.

[29] L. L. Hsiung, HRTEM Study of Oxide Nanoparticles in Fe-16Cr ODS Ferritic Steel Developed for Fusion Energy, Lawrence Livermore National Laboratory, LLNL-BOOK-438635, June 25, **2010**.
[30] T. A. H. Nguyen, A. V. Nguyen, *Langmuir* **2012**, *28*, 16725.
[31] E. Homede, O. Manor, *J. Colloid Interface Sci.* **2020**, *562*, 102.
[32] T. Boegelein, E. Louvis, K. Dawson, G. J. Tatlock, A. R. Jones, *Mater. Charact.* **2016**, *112*, 30.
[33] L. L. Hsiung, M. J. Fluss, A. Kimura, *Mater. Lett.* **2010**, *64*, 1782.
[34] M. B. Wilms, S.-K. Rittinghaus, M. Goßling, B. Gökce, *Prog. Mater. Sci.* **2023**, *133*, 101049.
[35] Z. Li, Z. Lu, R. Xie, C. Lu, Y. Shi, C. Liu, *Fusion Eng. Des.* **2017**, *121*, 159.
[36] Q. Tang, T. Hoshino, S. Ukai, B. Leng, S. Hayashi, Y. Wang, *Alloys. Mater. Trans.* **2010**, *51*, 2019.
[37] G. Zhang, Z. Zhou, H. Sun, L. Zou, M. Wang, S. Li, *J. Nucl. Mater.* **2014**, *455*, 139.
[38] A. Karch, D. Sornin, F. Barcelo, S. Bosonnet, Y. Carlan, R. de, Logé, *J. Nucl. Mater.* **2015**, *459*, 53.
[39] R. Jarugula, S. Koppoju, R. Jeyaraam, S. Ganesh Sundara Raman, G. Sundararajan, *Mater. Sci. Eng. A* **2021**, *800*, 140343.
[40] W. Hou, T. Stubbs, L. DeBeer-Schmitt, Y.-T. Chang, M.-A. Charpagne, T. M. Smith, A. Huang, Z. C. Cordero, *Addit. Manuf.* **2024**, *96*, 104554.
[41] T. Stubbs, R. Hou, D. N. Leonard, L. DeBeer-Schmitt, Y. Zhu, Z. C. Cordero, A. Huang, *Addit. Manuf. Lett.* **2024**, *9*, 100195.
[42] C. Kenel, A. Luca, S. S. de, Joglekar, C. Leinenbach, D. C. Dunand, *Addit. Manuf.* **2021**, *47*, 102224.
[43] K. A. Unocic, B. A. Pint, D. T. Hoelzer, *J. Mater. Sci.* **2016**, *51*, 9190.
[44] A. Afandi, R. Nisa, K. A. Z. Thosin, *J. Phys.: Conf. Ser.* **2017**, *817*, 12028.
[45] A. P. Mouritz, in *Introduction to Aerospace Materials*, Elsevier, Amsterdam **2012**, pp. 521–533.
[46] I. Y. Khairani, G. Mínguez-Vega, C. Doñate-Buendía, B. Gökce, *Phys. Chem. Chem. Phys.* **2023**, *25*, 19380.
[47] R. Streubel, M. B. Wilms, C. Doñate-Buendía, A. Weisheit, S. Barcikowski, J. H. Schleifenbaum, B. Gökce, *Jpn. J. Appl. Phys.* **2018**, *57*, 40310.
[48] G. Marzun, C. Streich, S. Jendrzej, S. Barcikowski, P. Wagener, *Langmuir* **2014**, *30*, 11928.
[49] M. Goßling, S.-K. Rittinghaus, F. Radtke, A. Elsayed, I. M. Kusoglu, A. Hariharan, U. Krupp, B. Gökce, *Powder Metall.* **2024**, *30*.
[50] P. K. Parida, A. Dasgupta, S. K. Sinha, *J. Mater. Eng. Perform.* **2021**, *30*, 9227.
[51] H. Xu, Z. Lu, C. Jia, H. Gao, C. Liu, *High Temp. Mater. Processes* **2016**, *35*, 321.
[52] P. Stolzenburg, A. Freytag, N. C. Bigall, G. Garnweitner, *CrystEngComm* **2016**, *18*, 8396.
[53] F. Tana, A. Serafini, L. Lutterotti, A. Cigada, F. Variola, F. Bondioli, L. de Nardo, *CrystEngComm* **2018**, *20*, 879.
[54] W. Shao, G. Zangari, *J. Phys. Chem. C* **2009**, *113*, 10097.
[55] G. Shishodia, S. Gupta, N. Pahwa, P. K. Shishodia, *J. Electron. Mater.* **2024**, *53*, 5159.
[56] A. Behbahani, S. Rowshanzamir, A. Esmaeilifar, *Procedia Eng.* **2012**, *42*, 908.
[57] A. K. Mahmoud, Z. Fadhill, S. I. Al-nassar, F. I. Husein, E. Akman, A. Demir, *JMSE-B* **2013**, *3*.
[58] M. R. N. Soares, T. Holz, F. Oliveira, F. M. Costa, T. Monteiro, *RSC Adv.* **2015**, *5*, 20138.
[59] K. Choudhury, R. K. Singh, P. Kumar, M. Ranjan, A. Srivastava, A. Kumar, *Nano-Struct. Nano-Objects* **2019**, *17*, 129.
[60] N. M. Kovalchuk, D. Johnson, V. Sobolev, N. Hilal, V. Starov, *Adv. Colloid Interface Sci.* **2019**, *272*, 102020.
[61] M. Miler, B. Mirtič, *Geologija* **2013**, *56*, 5.
[62] M. Li, W.-Y. Chen, X. Zhang, F. Heidet, E. J. Listwan, D. L. Rink, J. T. Listwan, Location-Dependent Mechanical Property Evaluation on Additively Manufactured Materials, Argonne National Laboratory Report, ANL/NSE-21/47, August **2021**, pp. 15–19.
[63] Y. Ha, A. Kimura, *Crystals* **2019**, *9*, 145.
[64] B. Leng, S. Ukai, Y. Sugino, Q. Tang, T. Narita, S. Hayashi, F. Wan, S. Ohtsuka, T. Kaito, *ISIJ Int.* **2011**, *51*, 951.
[65] H. R. Z. Sandim, R. A. Renzetti, A. J. O. Zimmermann, A. F. de Padilha, A. Möslang, *MSF* **2012**, *715–716*, 629.
[66] J. Chen, X. Li, L. Kang, T. Wang, L. Yi, K. Sang, Y. Lu, *J. Mater. Res. Technol.* **2024**, *32*, 1845.
[67] Y. Ijiri, N. Oono, S. Ukai, S. Ohtsuka, T. Kaito, Y. Matsukawa, *Nucl. Mater. Energy* **2016**, *9*, 378.
[68] F. Li, L. Li, Q. Fang, J. Li, B. Liu, Y. Liu, *J. Mater. Sci.* **2020**, *55*, 13414.
[69] J. Ren, L. Yu, Y. Liu, C. Liu, H. Li, J. Wu, *Materials* **2018**, *11*, 3.
[70] W. L. Baun, *Science* **1963**, *140*, 1330.

Appendix D: Academic Curriculum Vitae

For data protection reasons, the CV is not included in the online version.

Der Lebenslauf ist in der Online-Version aus Gründen des Datenschutzes nicht enthalten.